

1 **Recent progress on nanostructured carbon-based counter/back electrodes**
2 **for high-performance dye-sensitized and perovskite solar cells**

3
4 M. Aftabuzzaman[†], Chunyuan Lu[†], and Hwan Kyu Kim^{*}

5
6 *Global GET-Future Lab & Department of Advanced Materials Chemistry, Korea University,*

7 *2511 Sejong-ro, Sejong 339–700, Korea, *E-mail: hkk777@korea.ac.kr*

8
9
10
11
12
13
14
15
16
17 [†]*These authors made an equal contribution.*

18 ^{*}*To whom correspondence should be addressed: Email: hkk777@korea.ac.kr*

19

20

21

22 **Abstract:** Dye-sensitized solar cells (DSSCs) and perovskite solar cells (PSCs) favor minimal
23 environmental impact and low processing costs, factors that have prompted intensive research
24 and development. In both cases, rare, expensive, and less stable metals (Pt and Au) are used as
25 counter/back electrodes; this design increases the overall fabrication cost of commercial DSSC
26 and PSC devices. Therefore, significant attempts have been made to identify possible
27 substitutes. Carbon-based materials seem to be a favorable candidate for DSSCs and PSCs due
28 to their excellent catalytic ability, easy scalability, low cost, and long-term stability. However,
29 different carbon materials, including carbon black, graphene, and carbon nanotubes, among
30 others, have distinct properties, which have a significant role in device efficiency. Herein, we
31 summarize the recent advancement of carbon-based materials and review their synthetic
32 approaches, structure-function relationship, surface modification, heteroatoms/metal/metal
33 oxide incorporation, fabrication approaches, and effects on photovoltaic efficiency, based on
34 previous studies. Finally, we highlight the advantages, disadvantages, and design criteria of
35 carbon materials and fabrication challenges that inspire researchers to find low cost, efficient
36 and stable counter/back electrodes for DSSCs and PSCs.

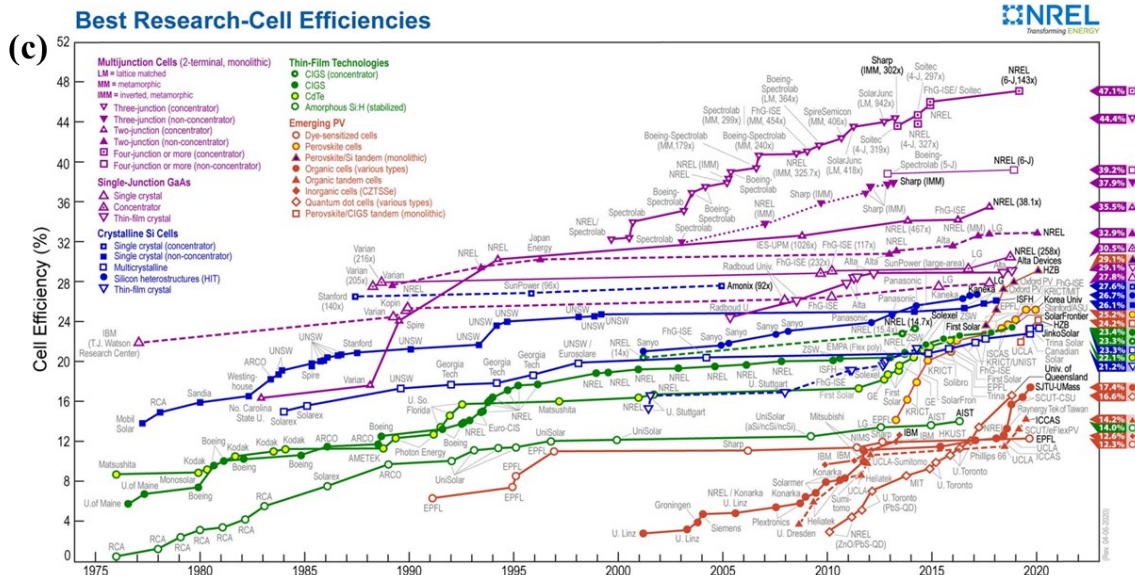
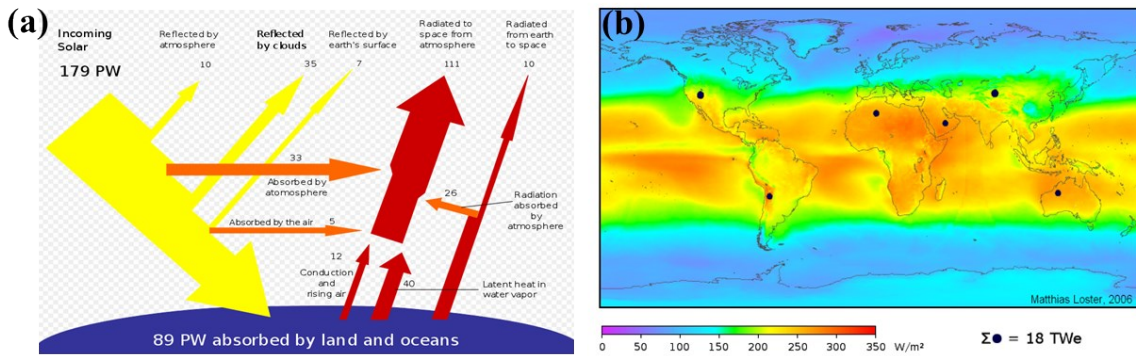
37

38 **1. Introduction**

39 Energy has become the key to achieving almost all sustainable development. Total energy
40 consumption in 2018 was 13864.9 mtoe (million tonnes oil equivalent, 1 mtoe = 4.1868×10^{16} J),
41 and by 2040, almost 815 quadrillion Btu (British thermal units, 1 Btu = 1055.06 J) energy will
42 be needed.^{1,2} To meet this ever-increasing demand for energy, fossil fuel depletion has
43 accelerated and, considering the greenhouse effect and climate change, exploration and
44 development of renewable energy resources have increased around the world. Among all of
45 the renewable energy sources, solar energy is the world's most rapidly developing system.

46 Indeed, total solar production has grown by an average of 8.3% per year and has the abundant
47 potential for power generation.^{1,3} The overall solar energy received by the Earth's crust is
48 roughly 3.8 million EJ per year, and the total global annual solar energy potential is 1,575
49 (minimum) to 49,837 EJ (maximum) per year (**Fig. 1a**).^{4,5} **Fig. 1b** shows the worldwide
50 distribution of solar radiation; the small black dots indicate a theoretical area large enough to supply
51 the entire world's energy demands (18 TW with solar power).

52 Third generation solar cells are often designated as evolving photovoltaic cells, including
53 dye-sensitized solar cells (DSSCs), quantum dot solar cells, organic/polymer solar cells,
54 perovskite solar cells (PSCs), etc. The majority of these designs are still in the research or
55 development stage. **Fig. 1c** displays the efficiency progress of the best researched cells since
56 1976. Notably, third generation solar cells favor minimal environmental impact and low
57 processing costs, factors that have prompted intensive research and development.⁶⁻¹² DSSC
58 energy conversion efficiency ($\eta \approx 14.0\%$) is far below that of silicon solar cells ($\eta \approx 26.1\%$).¹³⁻¹⁶
59 However, due to DSSCs' simple assembly technique, transparency, good plasticity, mechanical
60 robustness, environmental friendliness, and ability to work at wider angles, they are one of the
61 highly promising alternatives to silicon solar cells.^{17,18} Furthermore, their outstanding
62 performance¹⁹ ($\eta \approx 34\%$) in indoor-light conditions compared to other solar cells makes them a
63 possible candidate as a power source for indoor electronic devices and smart windows in building-
64 integrated photovoltaics (BIPVs).²⁰⁻²² On the other hand, PSCs, which originate from DSSCs, have
65 advanced from very low initial efficiency to show competitive efficiency with silicon solar cells in
66 only a decade. Hence, PSCs are the fastest-advancing solar technology. Furthermore, due to
67 low production cost, roll-to-roll processing ability, and flexibility, PSCs have become
68 commercially attractive for photovoltaic technology.



69

70 **Fig. 1** (a) Isolation of incoming solar radiation (photo credit: Frank van Mierlo).²³ (b) Worldwide
 71 distribution of solar radiation; small black dots indicate theoretical areas large enough to supply
 72 the entire world's energy demands (18 TW) with solar power²⁴ (photo credit: Matthias Loster). (c)
 73 Top solar cell efficiencies by National Renewable Energy Laboratory (NREL).²⁵ Images reprinted
 74 with permission (according to CC BY-SA 3.0).

75 Platinum (Pt) is a commonly used standard counter electrode (CE) in DSSCs due to its
 76 high catalytic activity for redox shuttles and high conductivity. However, Pt is a costly and rare
 77 noble metal, and thus it is not feasible for extensive use to industrialize DSSCs. Furthermore,
 78 Pt makes complexes with electrolyte and has insufficient long-term stability in DSSCs.
 79 Therefore, significant attempts have been made to find possible substitutes for an efficient, low
 80 cost, and stable CE. Similar to DSSCs, the back electrode (BE) used in PSCs (silver [Au] and

81 gold [Ag]) are expensive and less stable, factors that increase the overall device fabrication
82 cost and practical application of Au or Ag as the BE in commercial (or real) devices.

83 Carbon-based materials are favorable CE/BE candidates for DSSCs and PSCs due to their
84 excellent catalytic ability, easy scalability, low cost, and long-term stability.^{26–30} Furthermore,
85 the carbon work function (WF) (5.0) is close to Au (5.1) and Ag (4.7); this criterion is critical
86 for PSC BEs. Another advantage of carbon-based materials is its non-hydrophilic character: It
87 stops moisture penetration in the perovskite layer, even with no sealing process.³¹ In 1996, Kay
88 and Grätzel first employed a graphite–carbon black (CB) mixture as the CE in a DSSC.
89 Subsequently, many research attempts have explored different carbon materials, such as CB,
90 graphite, mesoporous carbon, carbon nanotubes (CNTs), graphene, and carbon nanofibers
91 (CNFs), all of which have been effectively utilized as CEs. However, the application of carbon-
92 based materials as the BE in PSCs has not grown at the same rate as DSSCs; it remains in an
93 emerging stage.

94 Some interesting reviews have discussed different CEs/BEs of DSSCs and PSCs.^{27–29,32,33}
95 However, in this review, we specially focus and discuss the different critical issues of carbon-
96 based CEs/BEs. We discuss the source, structure-function relationship, and synthesis methods
97 that greatly influence the performance of the materials. Finally, we highlight the advantages,
98 disadvantages, design criteria of carbon materials, and fabrication challenges of a CE/BE that
99 may lead researchers to identify low cost, efficient, and stable CEs/BEs for DSSCs and PSCs.

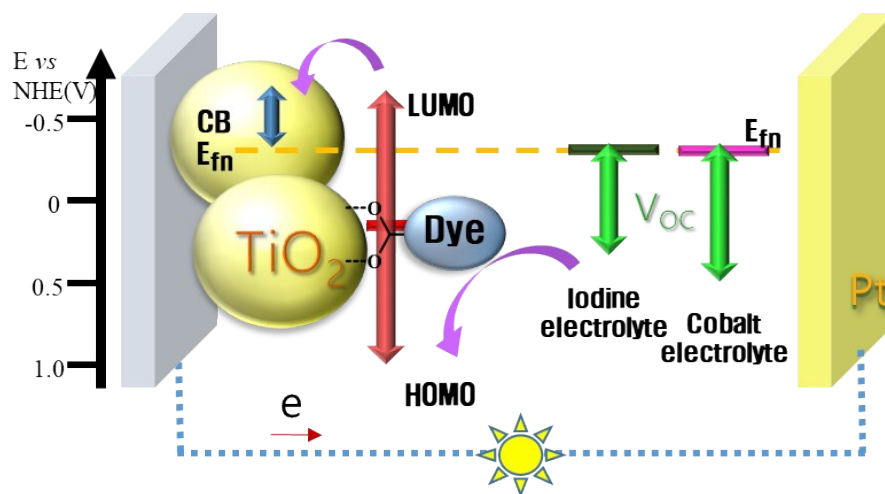
100 **2. Dye-sensitized Solar Cells**

101 **2.1. Working principle of DSSCs and the function of the CE**

102 In a conventional solar photovoltaic cell, when a sunlight photon hits the P-N junction, an
103 electron-hole pair is generated in the depletion region. Due to the built-in potential and electric
104 field in the depletion region, electrons move to the n-region and the holes move to the p-region.

105 When an external load is applied, electrons travel through the load and recombine with the
106 holes to complete the circuit.

107 The working principle of DSSCs is not similar to a conventional solar cell; rather, it is
108 similar to the natural photosynthesis process, where light absorption and charge carrier
109 transportation are mediated by different substances. The overall process in a DSSC can be
110 divided into four different fundamental steps: (i) photoexcitation of a sensitizer dye; (ii)
111 injection of the electron into the conduction band of a semiconductor metal oxide from the
112 excited dye and flow to the CE via an external circuit; (iii) reduction of an oxidized electrolyte
113 at the CE interface; and (iv) regeneration of the dye by accepting electrons from the redox
114 couple (**Fig. 2**). When a DSSC is exposed to light, the dye sensitizer is excited by absorbing a
115 photon and an electron from a HOMO jump to LUMO. The excited electron is injected into
116 the conduction band of the n-type semiconductor metal oxide film and diffuses to the anode.
117 For efficient electron transfer between the excited dye and semiconductor metal oxide, the
118 conduction band of the metal oxide should be lower than the LUMO level of the excited
119 dye.^{18,34} Typically, a layer of nanocrystalline titanium dioxide (TiO_2) is used as a
120 semiconductor electrode with a thickness ca. 10 μm , particle size 10–30 nm and porosity of 50–
121 60%.¹⁸



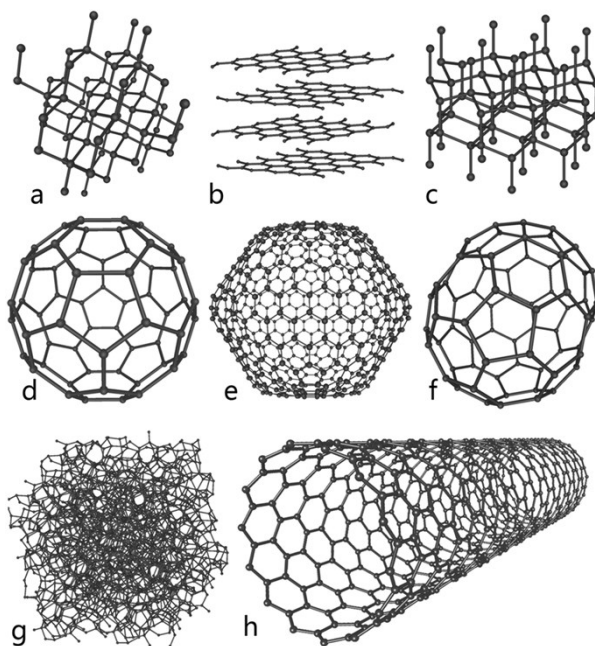
123 **Fig. 2** Schematic illustration of the working principle of dye-sensitized solar cells.

124 In DSSCs, the charge carriers face different types of resistance during the completion of
125 the circuit, including series resistance (R_s), the Warburg parameter (Z_W), and charge transfer
126 resistance (R_{ct}).^{35–37} Series resistance arises from the sheet resistance of transparent conductive
127 oxide (TCO) glass and the contact resistance of the cell. The Warburg parameter describes the
128 Nernst diffusion of the triiodide ion (I_3^-) in the electrolyte. Charge transfer resistance results
129 from the charge transfer at the photoanode/electrolyte and CE/electrolyte interface. In DSSCs,
130 the charge transfer resistance at the CE/electrolyte interface often dominates over other charge
131 transfer resistances, and thus R_{ct} often refers to charge transfer resistance at the CE/electrolyte
132 interface. The CE in a DSSC executes three fundamental functions^{38–42}: it collects electrons
133 from the external circuit, reduces the oxidized redox couple as a catalyst, and finally—as a
134 mirror—it reflects unabsorbed light from the cell back to the cell to enhance the utilization of
135 sunlight. The CE substantially contributes to the photovoltaic properties of DSSCs. The output
136 voltage of a DSSC after loading is lower than its theoretical maximum photovoltage or open-
137 circuit voltage. This voltage loss is due to the charge transfer or mass transfer over-potential as
138 well as the kinetic over-potential. The former originates from the electrocatalytic activity of
139 the CE toward the mediator, whereas the latter results from the ionic conductivity of
140 electrolytes and the transportation of mediator species from the CE to the photoanode.^{35,43}
141 Another important parameter, the fill factor (FF), depends on the aforementioned resistance
142 values. Decreasing the overvoltage for diffusion and electron transfer and reducing the charge
143 transfer resistance and series resistance will lead to a higher FF value, thus ensuring better
144 efficiency and allowing the output power of the solar cell to approach its theoretical maximum.

145

146 **2.2. Diverse carbon-based CEs for dye-sensitized solar cells**

147 Carbon is the 15th most abundant element on Earth. Carbon atoms can bond with each
148 other in diverse ways. There are eight carbon allotropes (**Fig. 3**): (i) diamond, (ii) graphite, (iii)
149 lonsdaleite, (iv) fullerenes, namely C₆₀ (buckminsterfullerene or buckyball), C₅₄₀, and C₇₀, (vii)
150 amorphous carbon, and (viii) CNTs (buckytube). Due to different intrinsic structures,
151 allotropes show distinct physical and electrochemical properties. Several carbon-based
152 materials, including CB, mesoporous carbon, graphite,^{79,45} graphene,^{46,47} CNTs, and CNFs,
153 have been successfully employed as CEs in DSSCs. To enhance the catalytic ability of carbon,
154 different heteroatoms (nitrogen [N], oxygen [O], sulfur [S], and phosphorus [P]) can be doped
155 in the carbon network. Due to their different electronegativity, the heteroatom redistributes the
156 spin and charge density of the carbon network and creates a highly efficient active site, where
157 reactant molecules interact more competently.^{48,49} Furthermore, different metals (Pt, iron [Fe],
158 cobalt [Co] and palladium [Pd]), metal oxides (RuO₂, Fe₂O₃, and NiO), alloy, and polymers
159 can be incorporated into the carbon matrix: The synergetic effect of the component materials
160 produces better catalytic performance.⁵⁰⁻⁵³ Different defect positions or heteroatoms in the
161 carbon substrate can be exploited as active sites for nucleation and growth of metal
162 nanoparticles (NPs). These features can help stabilize the deposited metal NPs with a small
163 size and narrow distribution.⁵⁴ Besides, the carbon substrate enhances the surface roughness
164 and oxygen vacancies of metal NPs and metal oxides, factors that also improve the catalytic
165 activity of carbon composites.



166

167 **Fig. 3.** Allotropes of carbon: (a) diamond, (b) graphite, (c) lonsdaleite, (d–f) fullerenes (C_{60} , C_{540} ,
 168 C_{70}), (g) amorphous carbon, and (h) carbon nanotube.⁵⁵ Copyright 2006, Wikipedia (reproduced
 169 by CC BY-SA 3.0).

170

171 2.2.1. Carbon black and dense carbons for dye-sensitized solar cells

172 **Carbon black (CB)** is an amorphous form of carbon with finely divided particles; it is
 173 generally obtained as soot from partial combustion of hydrocarbons. CB particles are spherical
 174 and their size varies widely depending on the process by which they are made. The particles
 175 are typically less regularly crystalline (paracrystalline). As a result of high surface-area-to-
 176 volume ratio, excellent conductivity, and electrocatalytic activity, CB is a good material for a
 177 CE.^{56,57}

178 The electrocatalytic activity and charge transfer resistance of CB depend on the particle
 179 size and its thickness on the fluorine-doped tin oxide (FTO) glass; these factors are crucial for
 180 the function and performance of DSSCs. As CB thickness increases, the charge transfer
 181 resistance of the CE drops. Above 14 μm , the enormous surface area of the CB leads to a low

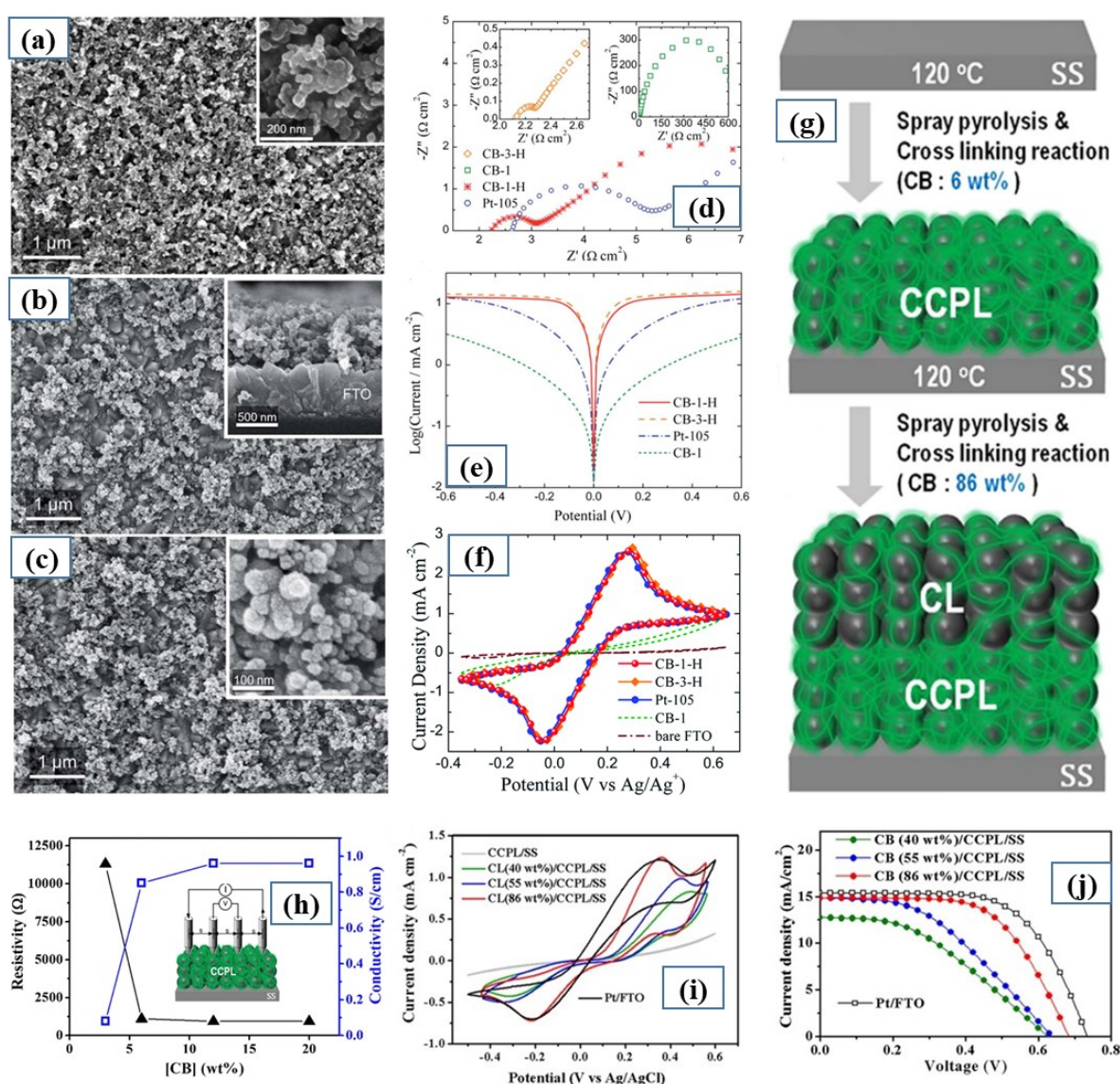
182 R_{ct} of approximately $2.96 \Omega \text{ cm}^2$ and enhances the DSSC's power conversion efficiency (PCE)
183 to 9.1%.⁵⁸ Kim *et al.* varied the particle size from 20 to 90 nm and controlled electrode
184 thickness from 1 to 9 μm by adjusting the spraying time. They increased the surface-to-volume
185 ratio by decreasing the CB particle size. These manipulations increase the electrocatalytic
186 activity and conductivity of the CB electrode. Charge transfer resistance decreases as the
187 electrolyte/electrode interface area increases.

188 The annealing temperature and composition of CB also play critical roles in the
189 photovoltaic performance, especially when a binder is used in CE fabrication.⁵⁹ At a low
190 temperature, excess binder materials leads to a high charge transfer resistance. The optimum
191 temperature is above 450°C , at which point the binder particles are entirely eliminated.
192 Consequently, the electrochemical properties of the resulting CB films become similar to those
193 of Pt film.

194 Recently, Liu *et al.* studied the electrocatalytic activity of CB material in Co-based DSSCs
195 (**Fig. 4a–f**).⁶⁰ They found that the amount of CB loading and the heat-treatment play equal key
196 roles in the electrochemical behavior of the resulting a thin CB film. Notably, one CB layer
197 without heat-treatment (denoted as CB-1) fully covers the FTO/glass substrate and is tightly
198 bound by ethyl cellulose molecules. By contrast, a heat-treated CB layer (i.e., CB-1-H) is partly
199 covered with aggregated CB clusters. The electrochemical studies revealed that heat-treated
200 CB shows very high catalytic activity and low charge transfer resistance. This CB particle
201 aggregation is evidently increased by augmenting the CB deposition layer (CB-3-H).
202 Furthermore, catalytic activity is increased with an increased CB deposition layer.

203 To augment the CE performance, CB composites have been made with different
204 materials, including polymer, graphene, and transition metals and their compounds.^{56,61–66}
205 Park's group developed a three-dimensional (3D) network epoxy polymer and CB composite,

206 acting as a catalytic layer and conductive corrosion protective layer (CCPL), by controlling the
 207 CB weight percentage alongside the polymer (**Fig. 4g-j**).⁶⁷ The authors fabricated the
 208 composite film by mixing cross-linkable epoxy monomers and polyamine hardener with CB;
 209 they applied it by the spray pyrolysis technique. They used an efficient charge collector
 210 stainless steel as the substrate. The CCPL (6 wt% of CB) is chemically stable in contact with
 211 electrolytes and can inhibit the diffusion of electrolytes. These data indicate it is a remarkable
 212 CCPL.



213

214 **Fig. 4.** Scanning electron microscopy (SEM) images of the (a) CB-1, (b) CB-1-H, and (c) CB-
 215 3-H films (top-view; the insets display magnified and cross-sectional images of the

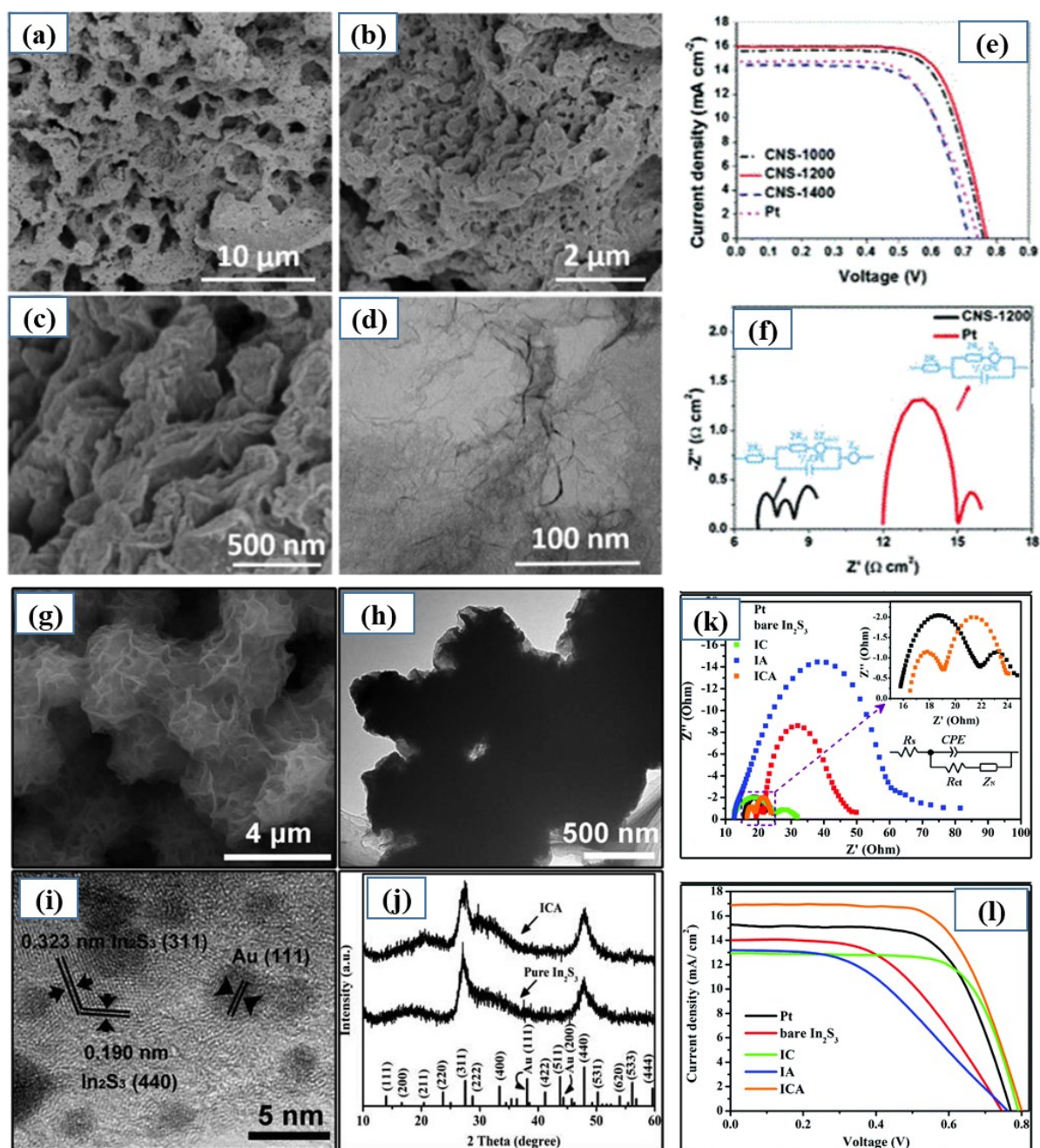
216 corresponding films, respectively). (d) Nyquist plots at 0 V, (e) Tafel polarization curves (10
217 mV s^{-1}) of the corresponding symmetrical dummy cells, and (f) CV of various thin-film
218 electrodes obtained at a scan rate of 100 mV s^{-1} in a three-electrode system. Copyright 2017,
219 The Royal Society of Chemistry; reprinted with permission.⁶⁰ (g) Fabrication procedures of a
220 SS counter electrode covering a composite of a three-dimensional (3D) network of polymers
221 and the carbon black (CB). (h) The conductivity and resistivity as a function of the wt% CB.
222 (i) CV curves using CL/CCPL/SS counter electrodes prepared with 40, 55, or 86% CB, and (j)
223 J-V curves of the corresponding dye-sensitized solar cells. Copyright 2016, Nature Publishing
224 Group; reprinted with permission.⁶⁷

225

226 Wu's group used the spin-coating method to fabricate cheap and efficient counter CEs for
227 DSSCs using Pt/CB composites.⁶⁸ To make the spin-coating procedure, they used ethyl
228 cellulose (EC) as a binder to control the viscosity of the Pt/CB composites. At the Pt-to-CB
229 ratio of approximately 1:3, the authors studied the influences of film composition (Pt/CB:EC
230 = 30:15 or 30:4) and the number of coating layers of the Pt/CB electrodes on the
231 electrochemical properties as well as the efficiency of the corresponding DSSCs. The analysis
232 showed that a Pt/CB CE with a lower fraction of EC (Pt/CB:EC = 30:4) exhibits a low charge
233 transfer resistance, high electrochemical activity, and good PCE (8.06%) comparable to that of
234 cells using Pt. The detailed information of CB CEs and their electrocatalytic and photovoltaic
235 properties in DSSCs are summarized in **Table 1**.

236 Different carbon-based materials with a low SSA also show very good catalytic activity
237 due to their high surface catalytic activity. Different polymers and biomass have been used
238 without any activating agent or template. Stucky *et al.* reported crystalline poly(triazine imide)-
239 based graphitic carbon nitride (g-CN) which they prepared via a reformed ionothermal process

240 by using a melamine-cyanuric acid (MCA) complex as precursor.⁶⁹ Li *et al.* reported an active
241 agent and template-free facile fabrication approach for the preparation of carbon nanosheets
242 (CNSs) (**Fig. 5a–f**).⁷⁰ To fabricate CNSs, the authors mixed sodium citrate and urea, ground
243 them, and annealed the mixture at various temperatures. At low-temperature solid-phase, cross-
244 linking occurs, while at high-temperatures, carbonization occurs. There were annealing
245 temperature–dependent electrochemical properties when applying CNSs as metal-free CEs for
246 DSSCs. Yuan *et al.* reported a unique In₂S₃-C-Au hybrid, fabricated simply by decorating
247 carbon-coated hierarchical In₂S₃ flower-like architectures with Au particles (**Fig. 5g–i**).⁷¹ The
248 authors synthesized the In₂S₃-C-Au (ICA) hybrid materials by two-step hydrothermal
249 treatment, using glucose and polyvinylpyrrolidone (PVP) as carbon sources. Electrochemical
250 performance showed that the hybrid material contains high catalytic activity and
251 electrochemical constancy for the interchange of the redox couple I₃⁻/I⁻. Moreover, the hybrid
252 material as a CE exhibits a better PCE (8.91%) compared to the commercial Pt counterpart
253 (7.67%).



254

255 **Fig. 5** (a–c) Field emission scanning electron microscopy (FE-SEM) images of the generated
 256 CNS-1200 at different magnifications. (d) A transmission electron microscopy (TEM) image
 257 of the generated CNS-1200. (e) J-V curves of the cells with carbon nanotube sheets (CNS) at
 258 different annealing temperatures compared to platinum (Pt). (f) Nyquist plots of the identical
 259 CNS-1200 and Pt counter electrodes (CEs) at 0.8 V (inset: equivalent circuit). Copyright 2018,
 260 The Royal Society of Chemistry; reprinted with permission.⁷⁰ (g) A SEM and (h and i)
 261 transmission electron microscopy (TEM) image of In₂S₃–carbon–Au (ICA) hybrid at different

262 magnifications. (j) X-ray diffraction (XRD) spectra of In_2S_3 (top) and In_2S_3 -carbon-Au with a
263 standard (bottom) of cubic In_2S_3 , JCPDS 32-0456. (k) Nyquist plots of electrochemical
264 impedance spectroscopy (EIS) spectra with an equivalent circuit (inset). (l) J-V curves of dye-
265 sensitized solar cells for different electrodes. Copyright 2017, The Royal Society of Chemistry;
266 reprinted with permission.⁷¹

267 Wang and Chen group's successfully planned and prepared a superlattice
268 polyoxometalate/ MoS_2 heterojunction coated on the activated carbon surface by a facile step-
269 by-step method. They used candle soot as carbon precursor.⁷² This nanomaterial contains the
270 synergetic benefits of the high conductivity of carbon NPs, admirable redox performance of
271 P_2Mo_{18} , and electrocatalytic activity of two-dimensional (2D) MoS_2 with the structural
272 advantages of a superlattice, heterojunction, high SSA, and hierarchical structure.
273 Electrochemical properties specify that the $\text{P}_2\text{Mo}_{18}/\text{MoS}_2@\text{C}$ nanomaterial has excellent
274 electric conductivity for fast charge transformation, as well as outstanding catalytic activities
275 for I_3^- reduction in DSSCs. Indeed, a DSSC that employs $\text{P}_2\text{Mo}_{18}/\text{MoS}_2@\text{C}$ as a CE shows a
276 PCE of 8.85%, which is higher than when using a Pt electrode. The details information of
277 dense-carbon counter electrodes and their electrocatalytic and photovoltaic properties in
278 DSSCs are summarized in **Table 2**.

279

280

281 **Table 1.** Carbon black (CB) counter electrodes and their electrocatalytic and photovoltaic properties in dye-sensitized solar cells.

CE Materials	Substrate/coating technology	Redox couple	Sensitizer	R_s/R_{ct} ($\Omega \text{ cm}^2$)	$J_{sc}/V_{oc}/FF$ ($\text{mA cm}^{-2}/\text{V}/\%$)	$\eta^{\text{CE}}/\eta^{\text{Pt}}$ (%)	Ref.	Year
CB	FTO-g/doctor blading	I_3^-/I^-	N719	-/0.66	15.00/0.78/71.3	8.35/8.29	59	2016
CB	FTO-g/spin coating	I_3^-/I^-	N719	-/-	14.70/0.75/67.0	7.28/7.13	73	2016
CB	FTO-g/spin coating	$\text{Co}^{3+}/\text{Co}^{2+}$	Y123	-/0.39	13.44/0.89/74.0	8.81/-	74	2017
CB	FTO-g/spin coating	$\text{Co}^{3+}/\text{Co}^{2+}$	Z907	-/0.39	11.74/0.85/72.0	7.21/7.10	74	2017
CB/CuO	FTO-g/doctor blading	I_3^-/I^-	N719	-/-	15.94/0.77/65.0	8.05/6.96	75	2015
CB/PT	Tinfoil/drop casting	I_3^-/I^-	N719	2.88/20.22	17.21/0.76/69.0	9.02/8.36	62	2016
CB- Fe_3O_4	ITO-g/drop casting	I_3^-/I^-	N719	1.86/0.47	14.40/0.66/51.0	6.1/4.1	61	2016
CB-g- C_3N_4	FTO-g/doctor blading	I_3^-/I^-	N3	-/2.4	13.21/0.69/56.0	5.09/5.45	76	2016
CB/Epoxy polymer	Stainless steel/spray coating	I_3^-/I^-	N719	-/20.0	17.7/0.70/59.4	7.3/7.1	67	2016
α - MnO_2 /CB	FTO-g/doctor blading	I_3^-/I^-	N719	-/-	11.41/0.66/57.0	4.29/4.24	64	2017
CB/Pt	FTO-g/spin coating	I_3^-/I^-	N719	-/1.44	14.76/0.77/70.3	7.99/8.17	63	2017
NiCo_2O_4 /CB	FTO-g/doctor blading	I_3^-/I^-	N3	-/-	16.08/0.65/65.0	6.27/7.38	77	2017
CB/PAniNT	FTO-g/doctor blading	I_3^-/I^-	N719	-/-	12.52/0.74/71.0	6.62/6.75	78	2018
CB/PAniNT	FTO-g/doctor blading	Polymer gel electrolyte	N719	-/-	9.11/0.74/71.0	4.82/6.75	78	2018
CB- Si_3N_4	FTO-g/screen-printed	I_3^-/I^-	N719	-/0.85	15.91/0.74/79.1	8.34/8.50	79	2018
N-CB@Pd	FTO-g/spin coating	I_3^-/I^-	N719	12.63/23.25*	15.34/0.74/70.0	7.95/7.85	80	2019

282 Abbreviations: FTO-g, fluorine-doped tin oxide glass; ITO-g, indium tin oxide glass; SSA, specific surface area. *Charge transfer unit is Ω

283

284

285

286

287 **Table 2.** Dense carbon counter electrodes (CEs) and their electrocatalytic and photovoltaic properties in dye-sensitized solar cells.

CE material(s)	Precursor/SSA (m ² g ⁻¹)	Substrate/coating technology	Redox couple	Sensitizer	R_s/R_{ct} (Ω cm ²)	$J_{sc}/V_{oc}/FF$ (mA cm ⁻² /V/%)	η^{CE}/η^{Pt} (%)	Ref.	Year
Carbon	poly(triazine imide)/58	FTO-g/drop casting	I ₃ ⁻ /I ⁻	N719	-/0.5	15.4/0.75/68.0	7.8/7.9	69	2015
Carbon	Urea, sodium citrate/-	FTO-g/doctor blading	I ₃ ⁻ /I ⁻	N719	3.48/0.35	15.94/0.77/71.03	8.71/7.24	70	2018
Carbon	Pomelo Peel/-	FTO-g/spray coating	I ₃ ⁻ /I ⁻	N719	27.14/3.16*	14.65/0.81/67.0	7.81/8.24	81	2019
Carbon	Coconut shell/-	FTO-g/pray coating	I ₃ ⁻ /I ⁻	N719		19.49/0.65/62.0	7.85/9.41	82	2019
Carbon/PANI	Citric acid/-	FTO-g/spin coating	I ₃ ⁻ /I ⁻	N719	13.2/1.93	13.8/0.77/70.0	7.45/7.37	83	2015
PEDOT:PSS/Carbon cloth	Commercial/-	Directly	I ₃ ⁻ /I ⁻	N719	-/1.52	14.95/0.70/72.0	7.60/7.08	84	2015
s-PT/Carbon cloth	Commercial/-	Directly	I ₃ ⁻ /I ⁻	N719	-/1.08	15.90/0.71/75.0	8.45/7.08	84	2015
CoSe ₂ /Carbon cloth	Commercial	FTO-g/-	I ₃ ⁻ /I ⁻	N719	2.66/0.26	18.03/0.73/67.0	8.92/8.25	85	2016
CoS ₂ /Carbon	MOF & PVP/-	FTO-g/spin coating	I ₃ ⁻ /I ⁻	N719	6.53/2.03*	16.9/0.73/66.0	8.20/7.88	86	2016
N-Carbon@FeCo	K ₄ Fe(CN) ₆ /3.84	FTO-g/spin coating	I ₃ ⁻ /I ⁻	N719	4.38/1.02	17.59/0.76/67.0	8.87/8.28	87	2016
N-Carbon@FeNi ₃	K ₄ Fe(CN) ₆ /9.52	FTO-g/spin coating	I ₃ ⁻ /I ⁻	N719	4.71/ 1.23	16.58/0.77/65.0	8.26/8.28	87	2016
Sb ₂ S ₃ @Carbon	Commercial/-	FTO-g/spin coating	I ₃ ⁻ /I ⁻	N719	6.7/10.3*	14.6/0.68/67.6	6.69/6.74	88	2016
Carbon/Pt	Bagasse/90.0	FTO-g/spin coating	I ₃ ⁻ /I ⁻	N719	5.30/1.60	15.3/0.73/62.0	6.98/6.08	89	2017
In ₂ S ₃ -carbon-Au	Glucose/-	FTO-g/doctor blading	I ₃ ⁻ /I ⁻	N719	5.51/-*	16.88/0.80/66.0	8.91/7.67	71	2017
Carbon/ Sn _{0.92} 5Ta _{0.075} O ₂	Glucose/119.7	Ti foil/dip coating	I ₃ ⁻ /I ⁻	N3	9.0/2.1	16.53/0.70/0.72	8.38/8.46	90	2017
CQDs-CoSe	Glucose/-	FTO-g/-	I₃⁻/I⁻	N719		17.64/0.733/0.70	9.08/-	91	2017
Carbon@Fe ₃ O ₄	Phenolic resin/93.8	Magnetic/spray coating	Co ³⁺ /C O ₂ ⁺	YD2-o-C8	6.32/4.60*	16.80/0.86/74.0	10.71/-	92	2018
Carbon-MoS ₂	Commercial/-	Graphite	I ₃ ⁻ /I ⁻	N719	1.54/0.28*	15.58/725/68.34	7.72/6.74	93	2018

paper/drop casting									
S-CQDs/CoSe	Maltitol/-	FTO-g/electrodeposition	I ₃ /I ⁻	N719	-/-	16.6/0.77/0.771	9.15/8.09	⁹⁴	2018
P ₂ Mo ₁₈ /MoS ₂ @Carbon	Candle soot/174.2	FTO-g/screen-printing	I ₃ /I ⁻	N719	5.78/1.44*	18.81/0.77/61.0	8.80/7.37	⁷²	2019
Carbon-Ni	Humic acid/-	FTO-g/doctor blading	I ₃ /I ⁻	N719	9.1/7.4	13.51/0.76/68.0	7.01/7.1	⁹⁵	2020

288 Abbreviations: FTO-g, fluorine-doped tin oxide glass; PANI, polyaniline; PEDOT:PSS, poly(3,4-ethylenedioxythiophene) polystyrene sulfonate; SSA, specific surface area.

289 *Charge transfer unit is Ω

290

291

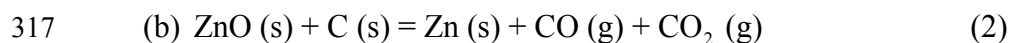
292

293 2.2.2. Porous carbons for dye-sensitized solar cells

294 Porous carbon materials have received significant attention as CEs for DSSCs owing to
295 their unique characteristics, including ultra-high surface areas, large pore volumes, and tunable
296 pore sizes and shapes. They also exhibit nanoscale effects in their pore channels and pore walls.
297 High surface areas provide a large number of reaction or interaction sites for surface or
298 interface-related processes, such as adsorption and catalysis. Moreover, mesoporous channels
299 facilitate the transport of atoms, ions, and large molecules through the bulk of the material and
300 assist to overcome charge transfer resistance.^{96–98} Different methods and precursors have been
301 used to synthesize mesoporous carbons; the efficiency of the mesoporous carbon electrodes
302 depend on synthetic methods and precursors.^{85–94}

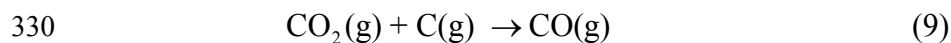
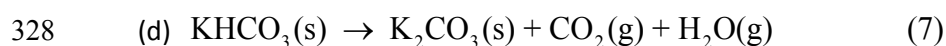
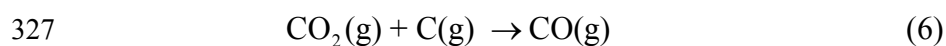
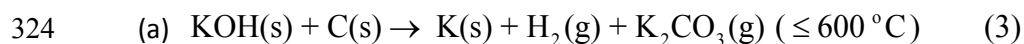
303 Activated carbons, due to their high surface area, pore structure (essentially microporous),
304 and high degree of surface reactivity, are widely used as catalysts. The primary raw material
305 used for activated carbon is any organic material with a high carbon content, such as coconut
306 shells, coal, peat wood, and polymers. Typically, physical (CO₂ or steam) or chemical (salts:
307 ZnCl₂, K₂CO₃, K₂SO₄,^{108,109} strong bases: KOH, NaOH,^{110,111} or acids: H₂SO₄, H₃PO₄)^{109,111}
308 activation methods are used to produce activated carbon. Transition metal chlorides, which
309 decompose at low temperatures (below the carbonization temperature), may act as crystalline
310 templates below the decomposition temperature, but at an elevated temperature, they act as
311 activating agents. For example, ZnCl₂ is generally considered to be a dehydrating agent that
312 eliminates water and induces aromatization and acts as a template below decomposition
313 temperature to create micropores. However, at an elevated temperature, zinc chloride hydrates,
314 which may form at low temperature, are converted to ZnO, which oxidizes carbon and creates
315 mesopores as well as micropores, according to Equations (1) and (2).^{109,112–114}





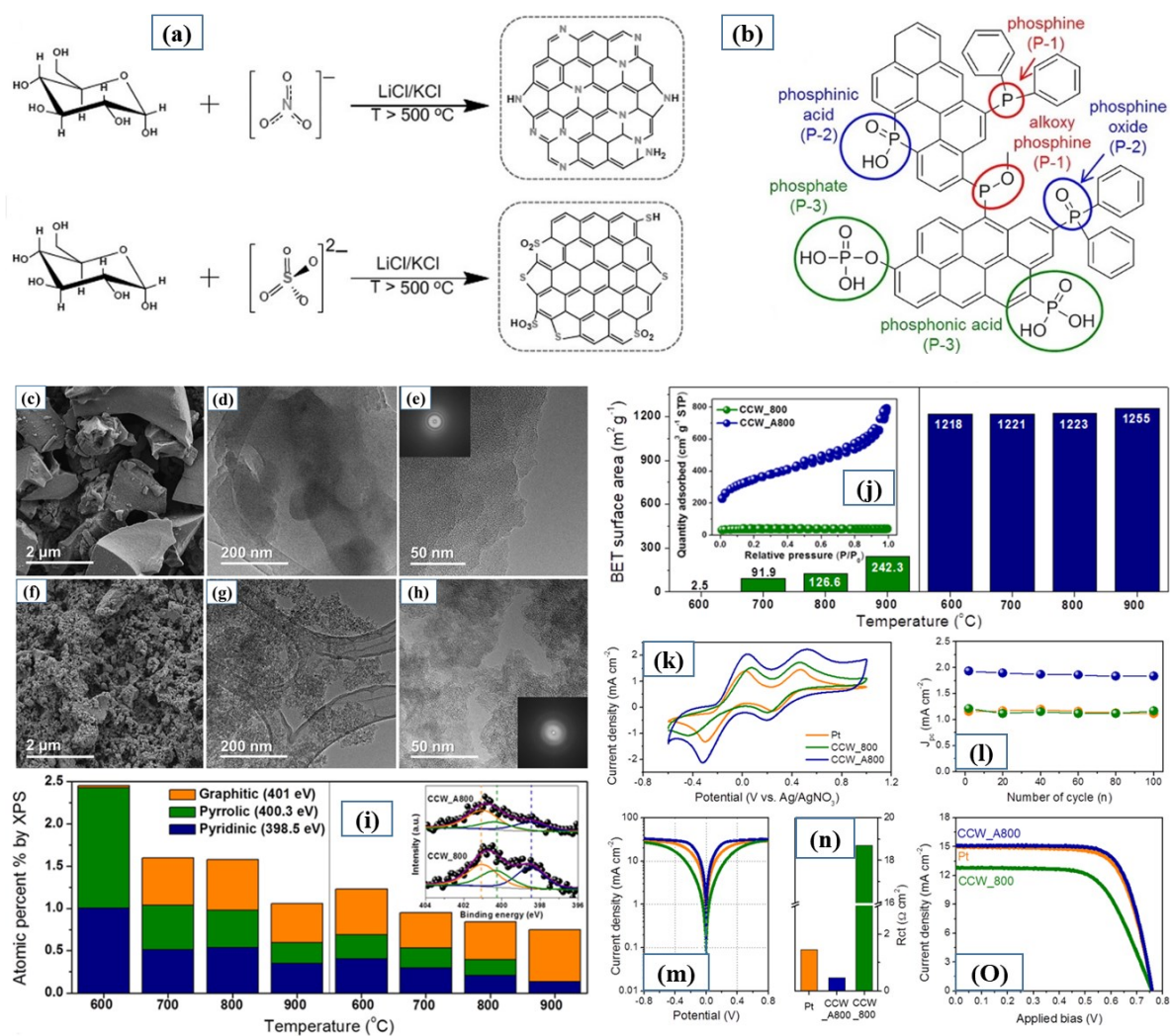
318

319 On the other hand, oxysalts, acids, and bases either oxidize lignocellulose or carbon itself
320 or decompose to form CO_2 , SO_4^{2-} , NO_3^- , or H_2O (steam), among other compounds, which
321 oxidize lignocellulose or carbon and create pores, according to Equations (3-9).^{115,116}
322 Furthermore, S-, N-, and P-containing activating agents may be incorporated heteroatoms in
323 the carbon network, as shown in **Fig. 6a**.^{112,117}



331 Activating agents and carbonization temperatures have significant effects on the
332 materials' surface morphology and performance. The carbonization temperature shows a
333 pyramidal effect on the efficiency of materials that contain heteroatoms. At low temperatures,
334 there is lower catalytic performance due to inferior graphitization, while at elevated
335 temperature, the fraction of heteroatoms decreases. Therefore, an optimized temperature is a
336 prerequisite. When researchers carbonized coffee waste (CW) carbonized with ZnCl_2 at
337 different temperatures, they found that the total surface area is higher for the prepared carbon
338 samples at a carbonization temperature 900°C , while the electrocatalytic performance is higher
339 for the carbon prepared at 800°C (**Fig. 6c-n**).¹¹⁸ This phenomenon occurs because of the
340 decreasing percentage of pyridinic and pyrrolic nitrogen. Our group activated anchovy-derived
341 carbons (AnCs) with KOH, a strong activating agent; there is a higher SSA ($2622 \text{ m}^2 \text{ g}^{-1}$) with

342 2.09 and 0.81 atom% N and S, respectively.¹¹⁹ AnCs as CEs in DSSCs show superior
 343 electrocatalytic activity compared to Pt CE with a $\text{Co}(\text{bpy})_3^{2+/3+}$ redox mediator. An AnC-based
 344 DSSC employing an SM-315 porphyrin sensitizer shows a PCE of 12.72%. To our knowledge,
 345 this is the highest reported value for DSSCs that utilize carbon nanomaterials as CEs.



346

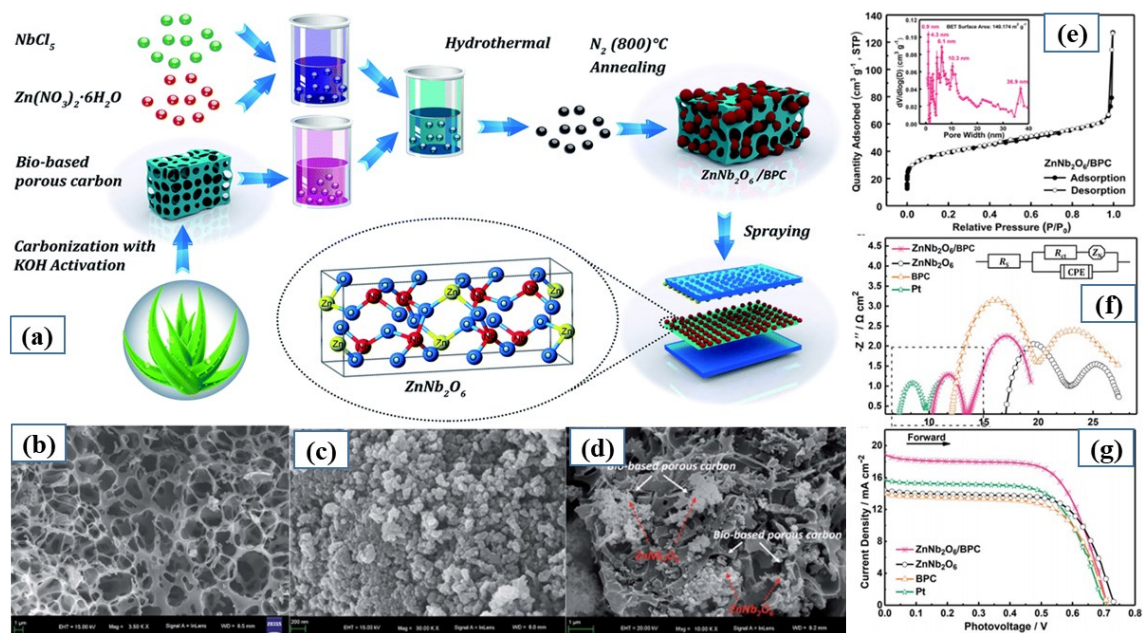
347

348 **Fig. 6.** (a) Development of N- and S-doped porous carbon sheets through the reaction of
 349 glucose and nitrate- (NO_3^-) or sulfate- (SO_4^{2-}) containing activating agents.¹¹⁷ (b) Types of P-
 350 containing functional groups in the carbon matrix activated with H_3PO_4 . Copyright 2013,
 351 WILEY-VCH; reprinted with permission.¹²⁰ (c) Scanning electron microscopy (SEM) and (d,
 352 e) transmission electron microscopy (TEM) images of CCW_800; (f) SEM and (g, h) TEM

353 images of CCW_A800 (insets of e and h correspond to fast Fourier transform (FFT) images).
354 (i) N 1s X-ray photoelectron spectroscopy (XPS) deconvoluted results of different CCW
355 samples (inset: N 1s XPS spectra of CCW_800 and CCW_A800). (j) Brunauer–Emmett–Teller
356 (BET) surface area of different CCW samples (inset: N₂ adsorption/desorption isotherms of
357 CCW_800 and CCW_A800). (k) CV spectra of CCW_800, CCW_A800, and Pt,
358 corresponding to the (l) cathodic peak current density as a function of the CV cycle number.
359 (m) Tafel polarization curves, (n) charge transfer resistance result based on electrochemical
360 impedance spectroscopy (EIS) fitting, and (o) J–V performance curve of a dye-sensitized solar
361 cells. Copyright 2017, The Royal Society of Chemistry; reprinted with permission.¹¹⁸

362

363 Wang *et al.* prepared activated N-doped porous carbons (a-NCs) by melamine-
364 formaldehyde (MF) resin incorporation in the graphene and subsequent alkali activation and
365 pyrolysis.¹²¹ The graphene integration, mesopore-rich porous texture, and moderate N doping
366 levels facilitate the applications of a-NCs as a CE in DSSCs. Wang *et al.* showed a simple and
367 general way to prepared bio-based porous carbon (BPC) supported by a ZnNb₂O₆ hybrid
368 containing a distinctive network structure that provides an efficient way to increase electron
369 transportation between the electrode/electrolyte interface, and higher PCE (**Fig. 7**).¹²² As the
370 raw materials, they used aloe peel waste, and by hydrothermal carbonization, KOH activation,
371 and pyrolysis carbonization, they prepared a network BPC structure. Subsequently, they
372 generated a dispersed solution of BPC in ethanol mixed with NbCl₅ and Zn(NO₃)₂·6H₂O salts
373 containing another ethanol solution. Next, they moved the mixed solution to a Teflon-coated
374 stainless-steel autoclave. Finally, they conducted hydrothermal treatment at 240°C for 12 h and
375 dried it under inert gas conditions. **Table 3** shows the details information of porous-carbon
376 counter electrodes and their electrocatalytic and photovoltaic properties in DSSCs.



377

378 **Fig. 7** (a) Schematic design of the preparation of the ZnNb₂O₆/BPC nanomaterial. Field
 379 emission scanning electron microscopy (FE-SEM) images of (b) BPC, (c) ZnNb₂O₆, and (d)
 380 ZnNb₂O₆/BPC. (e) The N₂ adsorption/desorption isotherms of ZnNb₂O₆/BPC. (f) Nyquist plots of
 381 the symmetrical cells, and (g) characteristic J-V curves of platinum (Pt), BPC, ZnNb₂O₆, and
 382 ZnNb₂O₆/BPC under one sun illumination. Copyright 2017, The Royal Society of Chemistry;
 383 reprinted with permission.¹²²

384

385 **Table 3.** Activated carbon counter electrodes (CEs) and their electrocatalytic and photovoltaic properties in dye-sensitized solar cells.

CE materials	Precursor/SSA (m ² g ⁻¹)	Substrate/coating technology	Redox couple	Sensitizer	R_s/R_{ct} (Ω cm ²)	$J_{sc}/V_{oc}/FF$ (mA cm ⁻² /V/%)	η^{CE}/η^{Pt} (%)	Ref.	Year
AC	Polypyrrole/707.98	FTO-g/drop casting	I ₃ ⁻ /I ⁻	N719	-/4.08	14.37/0.73/62.0	6.54/6.87	123	2016
AC	Pine cone flower/1589	FTO-g/brush painting	I ₃ ⁻ /I ⁻	N719	-/-	13.51/0.71/51.62	4.98/6.25	124	2017
AC	PANI/2580.5	FTO-g/spray coating	I ₃ ⁻ /I ⁻	N719	17.1/2.2	15.85/0.702/63.0	7.01/7.25	125	2017
AC	Anchovy/2622	FTO-g/spray coating	Co ³⁺ /Co ²⁺	SM-315	3.00/7.56	18.78/0.89/75.88	12.72/12.23	119	2017
AC	Coffee waste/1200	FTO-g/spray coating	I ₃ ⁻ /I ⁻	N719	6.05/0.46	15.09/0.76/72.6	8.32/8.07	118	2017
AC	Fish scales/2933	FTO-g/doctor blading	I ₃ ⁻ /I ⁻	N3	-/0.54	15.64/0.750/66.8	7.83/8.34	126	2018
AC	Quince leave/2196.6	FTO-g/brush painting	I ₃ ⁻ /I ⁻	N719	-/12.9*	14.99/0.70/52.59	5.52/6.56	127	2018
AC	Polypyrrole/636.27	FTO-g/drop casting	I ₃ ⁻ /I ⁻	N719	-/2.59	13.62/724/64.0	6.29/6.80	128	2019
AC	Pomelo peel /1283.77	FTO-g/spray coating	I ₃ ⁻ /I ⁻	N719	15.29/7.06	14.56/0.70/68.0	6.94/6.71	129	2019
AC	poly(para-phenylenediamine)/527	Carbon paper/brush painting	I ₃ ⁻ /I ⁻	N719	11.23/2.32	12.64/762/63.77	6.14/6.63	130	2020
AC	Polypyrrole/1744.98	FTO-g/spray coating	I ₃ ⁻ /I ⁻	N719	-/1.1	16.82/0.74/66.0	8.21/8.61	131	2018
AC/Graphene	Melamine resin/1302.4	FTO-g/doctor blading	I ₃ ⁻ /I ⁻	N719	15.65/3.75*	18.11/0.72 /53.0	6.91/7.10	132	2015
AC/MWCNT	Commercial/735.31	FTO-g/doctor blading	Quasi-solid gel electrolyte	N719	5.4/0.6	15.9/0.714/74.2	8.42/8.11	133	2017
AC/CNT	Commercial/735.32	Fabric/doctor blading	Gel electrolyte	N719	15/0.77*	12.4/0.72/70.19	6.26/7.26	134	2017
AC/NiWO ₄	Aloe peel/-	FTO-g/spray coating	I ₃ ⁻ /I ⁻	N719	5.65/1.08	14.70/0.70/69	7.08/6.46	135	2019
AC/CoWO ₄	Aloe peel/-	FTO-g/Spray coating	I ₃ ⁻ /I ⁻	N719	7.22/4.03	13.96/0.69/63.0	6.07/6.46	135	2019
AC/FeWO ₄	Aloe peel/-	FTO-g/spray coating	I ₃ ⁻ /I ⁻	N719	6.51/4.25	14.38/0.68/55.0	5.38/6.46	135	2019
V ₂ O ₃ @AC	Commercial/520.0	FTO-g/spray coating	I ₃ ⁻ /I ⁻	N719	-/1.32*	11.38/0.733/67.0	5.55/4.54	136	2019

AC/ZnNb ₂ O ₆	Aloe peel/140.17	FTO-g/spray coating	I ₃ ⁻ /I ⁻	N719	12.78/6.50	19.12/0.71/65.0	8.83/7.14	¹²²	2019
AC/FeTa ₂ O ₆	Aloe peel/-	FTO-g/spray coating	I ₃ ⁻ /I ⁻	N719	3.10/3.52	15.16/0.70/65.0	6.85/6.34	¹³⁷	2019

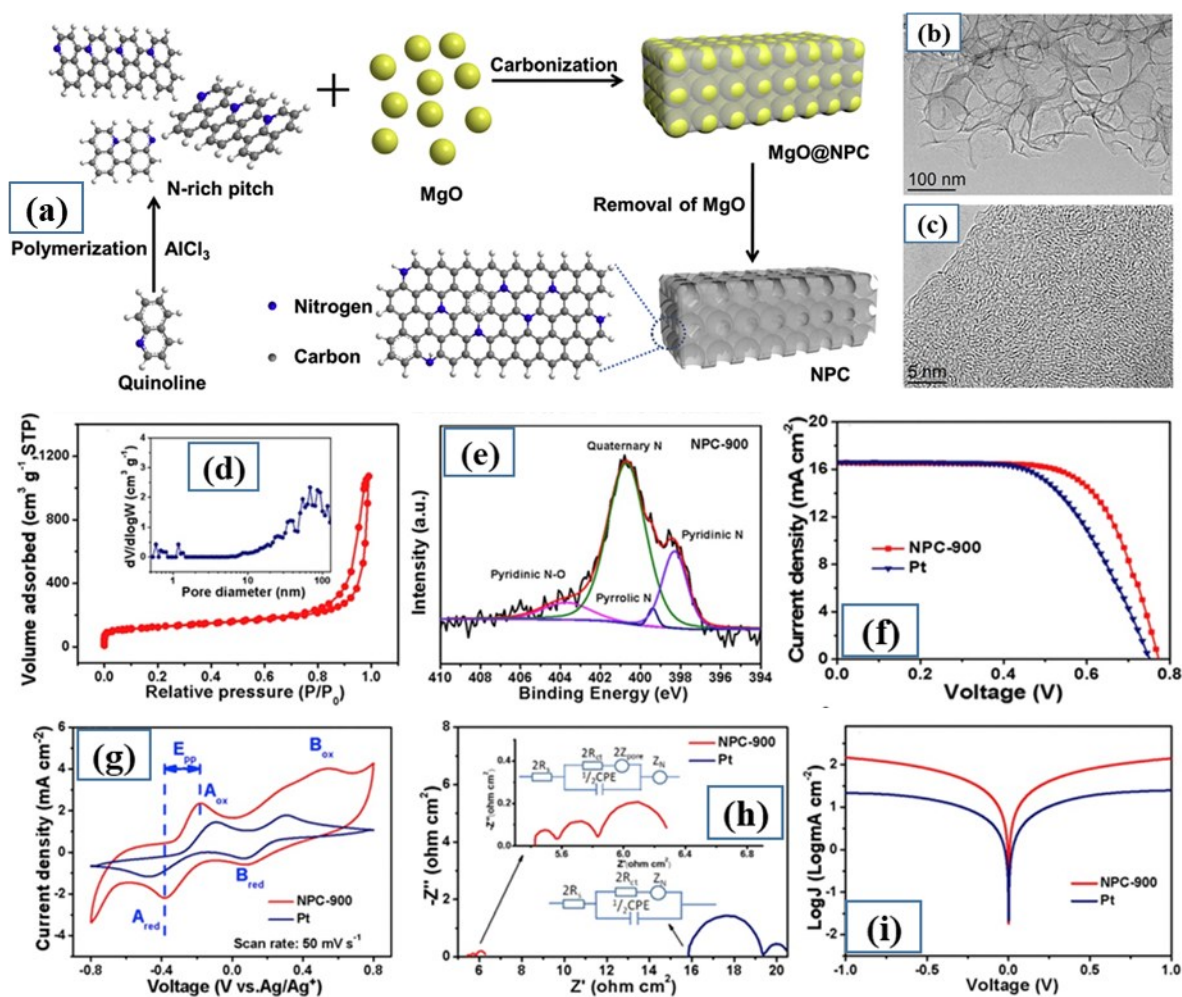
386 Abbreviations: AC, activated carbon; CNT, carbon nanotubule; FTO-g, fluorine-doped tin oxide glass; MWCNT, multi-walled carbon nanotubules; PANI, polyaniline; SSA,

387 specific surface area. *Charge transfer unit is Ω

388

389 Different template methods, including hard and soft templates, are generally used to
390 produce mesopores or macropores alongside micropores in many carbon materials. In the hard
391 template processes, carbon precursors are incorporated into the templates with well-defined
392 structures. Subsequently, templates are removed by high-temperature, dissolution, or chemical
393 etching, leaving behind the negative carbon replicas of the templates. Silica,^{138,139} inert alkali
394 metal chlorides (LiCl, NaCl, or KCl),^{112,140} alkali earth metal oxides (MgO or CaO)^{141–143},
395 sulfates (MgSO₄),¹⁴⁴ and carbonates (CaCO₃)^{145–147} are used as hard templates.

396 Xiao *et al.* used an MgO-based hard template method to synthesize N-doped porous
397 carbon (NPC) from the nitrogen-rich pitch (**Fig. 8a–i**).¹⁴⁸ The authors mechanically mixed N-
398 rich pitch and MgO with a 1:6 mass ratio, followed by carbonization at 900°C. The porous
399 carbon obtained at 900°C contains a high nitrogen content (7.11 wt.%) with high SSA and
400 displays high electrocatalytic activity in the iodine reduction reaction. The generated NPC
401 provides higher PCE (8.75%) compared to that of the commercial Pt CE (7.55%). Li *et al.* used
402 basic magnesium sulfate (BMS) whiskers to fabricate dual-doped meso/microporous carbon as
403 low-cost and efficient CEs for I₃⁻ reduction.¹⁴⁴ Melamine is used as N-containing carbon source,
404 while BMS whiskers are used as an S source and templates. This higher photovoltaic efficiency
405 is due to the merits of well-balanced and fast charge transportation relating to facile ion transfer
406 and fast electron conduction to the open framework structure and soft carbon nature of pitch-
407 derived porous carbon, respectively.



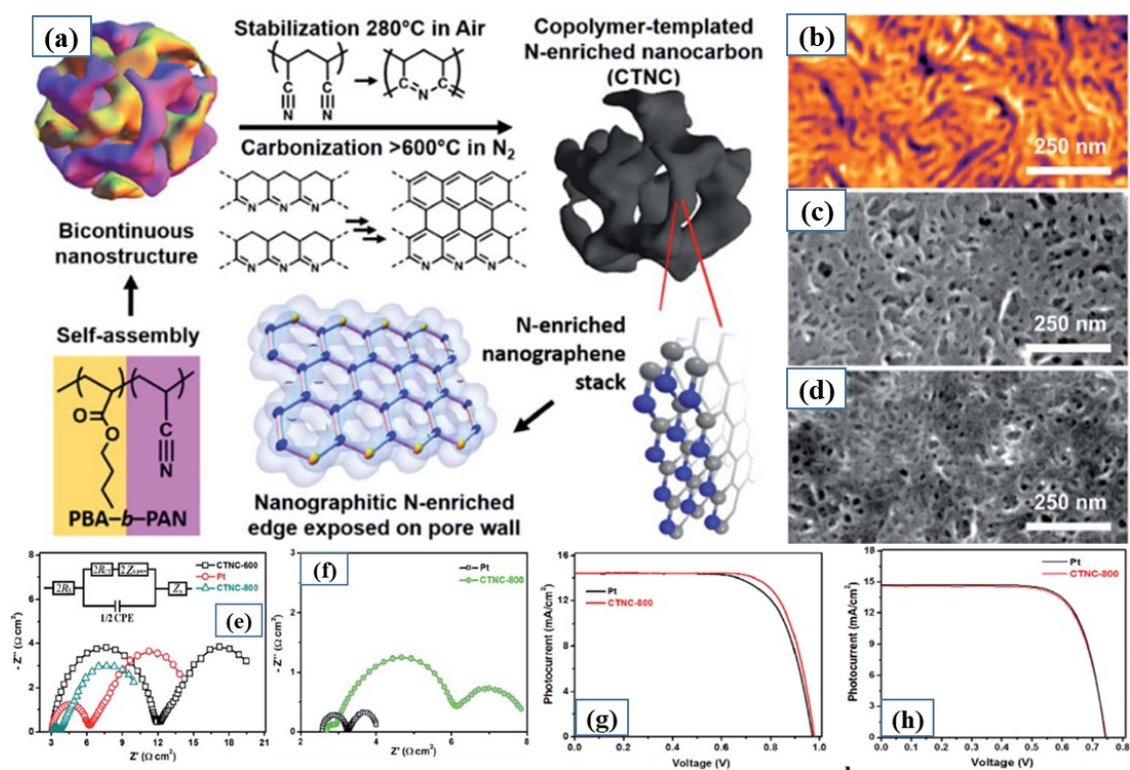
408

409 **Fig. 8.** (a) Schematic presentation of nitrogen-doped porous carbon (NPC) synthesis. (b, c)
 410 High-resolution transmission electron microscopy (HR-TEM) images of NPC-900. (d) N_2
 411 adsorption and desorption isotherm (inset: the pore size distribution) and (e) high-resolution
 412 $N1s$ X-ray photoelectron spectroscopy (XPS) spectrum of NPC-900. (f) J-V for dye-sensitized
 413 solar cells (DSSCs) based on a NPC-900 or platinum (Pt) counter electrode (CE). (g) CV
 414 curves, (h) Nyquist plots of the symmetrical dummy cells (inset: the magnified plots and
 415 equivalent circuits), and (i) Tafel polarization curves of NPC-900 and Pt. Copyright 2018,
 416 Elsevier; reprinted with permission.¹⁴⁸

417

418 Unlike the hard template, soft templates do not possess a concrete shape. Soft templates
419 are mainly block copolymers or organic molecules. In a liquid mixture, soft templates form
420 micelles via self-assembly and act as the structure-directing agent. The hydrophilic tails of
421 micelles then interact with the carbon precursor through covalent or hydrogen bonds. In this
422 process, micelles are enclosed inside the carbon precursor. The enclosed micelles are then
423 removed by heat treatment in an inert atmosphere above 400°C, creating hierarchically ordered
424 mesopores inside the carbon. The shape of the pores depends on the shape of the micelles.¹⁴⁹

425 Our group prepared copolymer-templated N-enriched nanocarbon (CTNC) and examined
426 the performance with I^-/I_3^- and $Co(bpy)_3^{2+/3+}$ redox mediators (**Fig. 9**).¹⁵⁰ This is also considered
427 as a self-template or template-free method. We used polyacrylonitrile-*b*-poly(butyl acrylate)
428 (PAN-*b*-PBA) block copolymer as a precursor, where the PAN fraction acts as a source of
429 graphene-like structure and the PBA fraction acts as sacrificial block to create pores. CTNC
430 shows greater catalytic activity towards the $Co(bpy)_3^{2+/3+}$ reduction reaction and higher
431 efficiency in comparison to the typical Pt CE. The experimental catalytic activity is due to the
432 synergetic effect of the large surface area of CTNCs provided by a 3D bi-continuous structure
433 and hierarchical pore connection. Furthermore, their distinctive electrical characteristics result
434 from the existence of N heteroatoms situated on the edges of nano graphitic domains.



435

436 **Fig. 9.** (a) Schematic presentation of copolymer-templated nitrogen-enriched nanocarbon
 437 (CTNC) preparation. (b) Atomic force microscopy (AFM) of PBA-*b*-PAN, displaying a bi-
 438 continuous morphology. (c and d) Scanning electron microscopy (SEM) images of the thin-
 439 film CTNC obtained at 400°C and 900°C, respectively. (e and f) Nyquist plots of symmetrical
 440 dummy cells consisting of CTNC and platinum (Pt) counter electrodes (CEs) for Co(bpy)₃^{2+/3+}
 441 and I⁻/I₃⁻ electrolytes, respectively (inset: the corresponding equivalent circuit). (g and h) J-V
 442 curves of JK-306-based dye-sensitized solar cells with CTNC-800 and Pt CEs under one sun
 443 illumination with Co(bpy)₃^{2+/3+} and I⁻/I₃⁻ based electrolytes. Copyright 2015, The Royal Society
 444 of Chemistry; reprinted with permission.¹⁵⁰

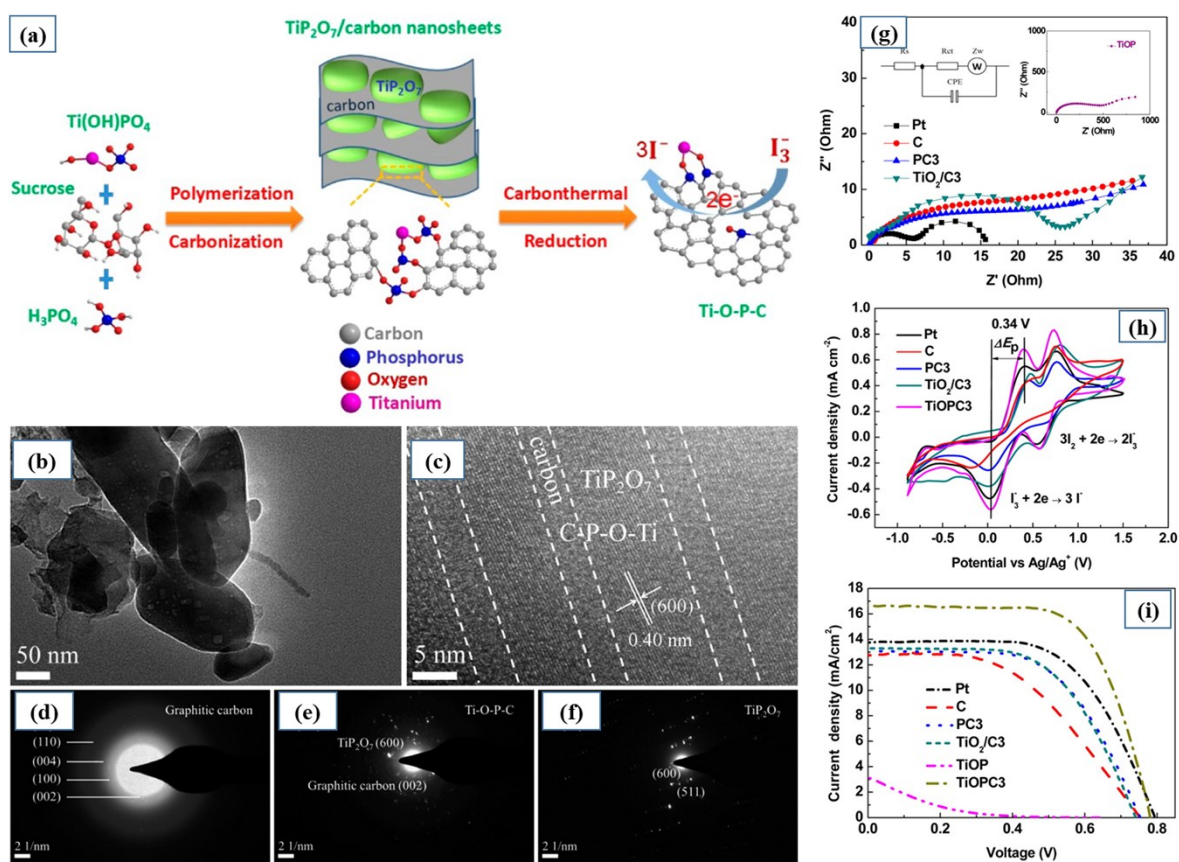
445

446 To enhance catalytic activity and stability, porous carbon with ordered graphitic layer
 447 has been mixed with a polymer, transition metal, metalloid, or other nanocarbon materials like
 448 graphene and CNTs to enhance the catalytic activity, wettability toward electrolytes, and long-
 449 term stability.^{149,151–154} Wang and Lin's group used a polystyrene sphere as a soft template to

450 prepare CoSe₂ NPs inserted into porous carbon shells (CoSe₂/CS) as highly competent catalysts
451 for the I₃⁻ reduction reaction.¹⁵⁵ They covered the polystyrene sphere with polydopamine-
452 containing Co precursor. After pyrolysis at 800°C, they removed the polystyrene sphere with
453 CoO_x/CS, which after calcination with Se powder at 450°C under an Ar atmosphere produces
454 CoSe₂/CS. The carbon nanoshells are highly graphitized with N doping, and CoSe₂ NPs are
455 well distributed within the nanoshells. Our group recently doped tellurium (Te) and ruthenium
456 (Ru) in the copolymer-templated N-enriched nanocarbon network via an *in situ*
457 approach.^{52,156,157} We found that after doping, the Te and Ru atom 3D carbon network retains
458 its hierarchical graphene-like structure, including numerous defect sites and high porosity.
459 Therefore, the generated Te- and Ru-doped CTNC shows better catalytic ability toward both
460 iodine and cobalt redox couples. We obtained the highest efficiencies of 11.64 and 9.67% under
461 one sun illumination for SGT-021/Co(bpy)₃^{2+/3+}- and N719/I⁻/I₃⁻-based DSSCs with Te-doped
462 CTNC CEs. These values are higher compared to using a Pt CE.

463 To enhance the synergetic effect of different elements, Chen *et al.* synthesized titanium,
464 oxygen, phosphorus, and carbon-containing compositional material (TiOPC) as a CE
465 competent in I₃⁻/I⁻ redox couples (**Fig. 10**).¹⁵⁸ In this study, they obtained TiOPC
466 nanocomposites from carbon thermal transformation of TiP₂O₇ at a high temperature in inert
467 conditions. Furthermore, they examined the catalytic performance of TiOPC by varying the
468 carbon composition in the nanocomposites. They found that TiOPC with approximately 24.6
469 wt% carbon enhances porosity and displays better electrocatalytic activity in the iodine
470 reduction reaction, offering a photovoltaic performance of 8.65%. The energy conversion
471 efficiency of TiOPC CE-based DSSCs is even greater than that of the typical Pt-based CE
472 (6.66%). The superior catalytic activity of TiOPC is due to the existence of a leading
473 Ti–O–P–C structure, besides the uninterrupted conductive carbon structure and higher

474 porosity. Detailed information about mesoporous carbon CEs and their electrocatalytic and
 475 photovoltaic properties in DSSCs are summarized in **Table 4**.



476

477 **Fig. 10.** (a) Schematic illustration of the synthesis of titanium, oxygen, phosphorus, and carbon
 478 (TiOPC_x) composites. (b, c) Transmission electron microscopy (TEM) images and (d–f)
 479 selected area electron diffraction (SAED) patterns of the TiOPC₃ nanocomposite. (g) Nyquist
 480 plots and (h) CV curves of different CEs. (i) J–V curves of dye-sensitized solar cells with
 481 different CEs. Copyright 2016, American Chemical Society; reprinted with permission.¹⁵⁸

482 **Table 4** Mesoporous carbon counter electrode (CE)s and their electrocatalytic and photovoltaic properties in dye-sensitized solar cells.

CE material(s)	Precursor/SSA (m ² g ⁻¹)	Substrate/coating technology	Redox couple	Sensitizer	R_s/R_{ct} (Ω cm ²)	$J_{sc}/V_{oc}/FF$ (mA cm ⁻² /V/%)	η^{CE}/η^{Pt} (%)	Ref.	Year
N-doped porous carbon	Resorcinol & cyanamide/728.0	FTO-g/doctor blading	I ₃ /I ⁻	N719	-/-	13.75/0.79/67.2	7.27/6.92	138	2015
S-doped porous carbon	Pitch/649.0	FTO-g/spray coating	I ₃ /I ⁻	N719	6.45/1.99*	14.98/0.70/67.0	6.97/7.28	159	2015
N-doped porous carbon	PBA- <i>b</i> -PAN/485.0	FTO-g/spray coating	Co ³⁺ /Co ²⁺	SM-315	1.55/0.31	14.57/0.97/73.5	10.32/9.80	160	2015
N-doped porous carbon	PBA- <i>b</i> -PAN/485.0	FTO-g/spray coating	I ₃ /I ⁻	N719	-/-	14.58/0.74/72.9	7.88/8.11	160	2015
Porous carbon	Eggshell membranes/401.0	FTO-g/doctor blading	I ₃ /I ⁻	N719	5.77/1.22	13.40/0.79/63.	6.71/6.63	161	2015
N-doped porous carbon	Resorcinol/246.3	FTO-g/doctor blading	I ₃ /I ⁻	N3	-/0.77	15.19/0.71/66.0	7.09/7.31	162	2015
Porous carbon	CMS/301.4	FTO-g/spray coating	Co ³⁺ /Co ²⁺	YD2-o-C8	11.96/2.44	15.24/0.84/68.0	8.73/ 9.41	163	2016
Porous carbon	MOF/813.9	-/-	I ₃ /I ⁻	N719	7.43/8.54*	13.56/0.77/68.0	7.32/7.53	164	2016
N/S-doped porous carbon	PVA & melamine/814	FTO-g/spray coating	I ₃ /I ⁻	N719	6.43/1.85	14.42/0.73/70.6	7.41/ 7.14	144	2016
Co@Porous carbon	MOF/231.0	FTO-g/spray coating	I ₃ /I ⁻	N719	-/-	13.29/0.80/ 74.0	7.92/ 8.18	165	2016
Porous carbon	Resorcinol/454.47	FTO-g/spray coating	I ₃ /I ⁻	N719	6.14/1.22	14.82/0.78/58.0	6.71/7.88	166	2016
Porous carbon	Polystyrene & resorcinol/-	FTO-g/spray coating	Co ³⁺ /Co ²⁺	YD2-o-C8	5.63/0.37	16.90/0.86/73.0	10.61/9.41	166	2016
Porous carbon	Tetraaminobenzene tetrahydrochloride & benzene tricarboxylic acid/406.0	FTO-g/spray coating	Co ³⁺ /Co ²⁺	SGT-129	1.33/ 0.51	16.30/0.84/71.9	9.82/9.28	167	2017
Porous carbon	Resorcinol/431.4	Ti-oil/spray coating	Co ³⁺ /Co ²⁺	YD2-o-C8	4.08/1.06	15.71/0.84/68.8	9.10/-	168	2017
N-doped porous carbon	Pitch/407.0	FTO-g/dip coating	I ₃ /I ⁻	N719	2.71/0.14	16.54/0.77/69.0	8.75/7.55	169	2018
Porous carbon	Pomelo peel/154.0	FTO-g/spray coating	I ₃ /I ⁻	N719	12.76/1.02*	16.24/0.79/65.0	8.29/8.24	170	2018

N-doped porous carbon	PpPD/657	FTO-g/doctor blading	I ₃ /I ⁻	N719	5.6/-	16.08/0.75/0.74	8.90/8.09	171	2018
Porous carbon	Resorcinol/724.0	FTO-g/doctor blading	I ₃ /I ⁻	N719	11.06/3.96	16.59/0.77/71.0	9.08/7.92	172	2019
Graphene/Porous carbon	Resorcinol/485.0	FTO-g/doctor blading	I ₃ /I ⁻	N719	15.58/8.47*	15.13/0.73/61.0	6.82/7.08	153	2015
TiOP/Porous carbon	Sucrose/227.0	FTO-g/doctor blading	I ₃ /I ⁻	N719	0.15/0.17	16.64/0.78/67.0	8.65/6.66	158	2016
W ₂ C/Porous carbon	Resorcinol/327.3	ITO-PEN/spray coating	I ₃ /I ⁻	N719	-/-	15.23/0.74/67.2	7.61/-	151	2016
VC/Porous carbon	Resorcinol/436.82	ITO-PEN/spray coating	Co ³⁺ /Co ²⁺	YD2-o-C8	15.5/0.48	15.86/0.84/73.2	9.75/8.18	173	2016
CoNi/Porous carbon	Starch & Gelatin/236.0	FTO-g/doctor blading	I ₃ /I ⁻	N719	18.3/3.2*	18.53/0.70/58.0	7.58/7.15	174	2017
Fe/N-doped porous carbon	Resorcinol/1041.73	FTO-g/spin coating	I ₃ /I ⁻	N719	-/-	12.53/0.74/74.9	6.94/6.69	175	2018
N-doped porous carbon	Resorcinol/690.0	-/-	I ₃ /I ⁻	-	-/-	15.3/0.74/69.21	7.89/7.48	176	2019
N, S-doped porous carbon	Resorcinol/388.0	-/-	I ₃ /I ⁻	-	-/-	19.6/0.67/60.76	8.03/7.52	177	2019
CoSe ₂ /Porous carbon	PVP & polystyrene/-	FTO-g/doctor blading	I ₃ /I ⁻	N719	0.22/-	15.88/0.69/69.0	7.56/7.40	155	2019
HCS/NiS/RGO	Polydopamine/366	FTO-g/doctor blading	I ₃ /I ⁻	N719	0.14/13.7	22.3/0.77/54.07	9.32/8.06	178	2019
Te-N-Porous carbon	PAN- <i>b</i> -PBA/540.69	FTO-g/spray coating	I ₃ /I ⁻	N719	2.45/0.24	17.06/0.73/77.3	9.67/9.62	52	2019
Te-N-Porous carbon	PAN- <i>b</i> -PBA/540.69	FTO-g/spray coating	Co ³⁺ /Co ²⁺	SGT-021	2.26/0.53	16.09/0.89/79.4	11.64/11.59	52	2019
CQD/CS	Resorcinol/1498	FTO-g/doctor blading	I ₃ /I ⁻	N719	0.1/4.0	16.87/0.72/69.7	8.48/7.35	179	2020
Ru-N-Porous carbon	PAN- <i>b</i> -PBA/464.8	FTO-g/spray coating	Co ³⁺ /Co ²⁺	SGT-021	0.034/1.18	18.20/0.83/76.1	11.42/11.16	156	2020

483 Abbreviations: FTO-g, fluorine doped tin oxide glass; PAN-*b*-PBA, polyacrylonitrile-*b*-poly(butyl acrylate); PVA, polyvinyl alcohol; PVP, polyvinylpyrrolidone; SSA, specific

484 surface area. *Charge transfer unit is Ω

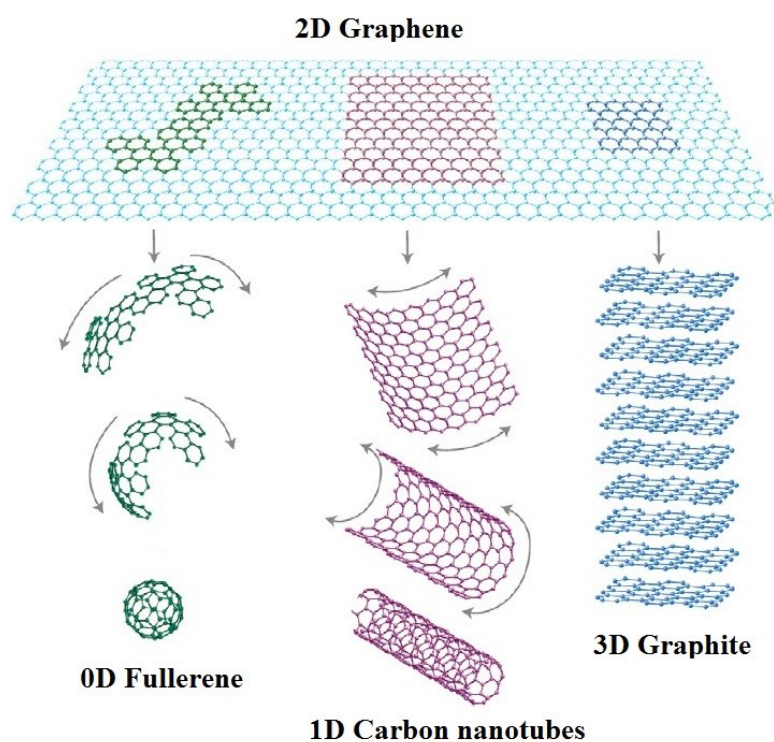
485

486

487

488 **2.2.3. Graphene for dye-sensitized solar cells**

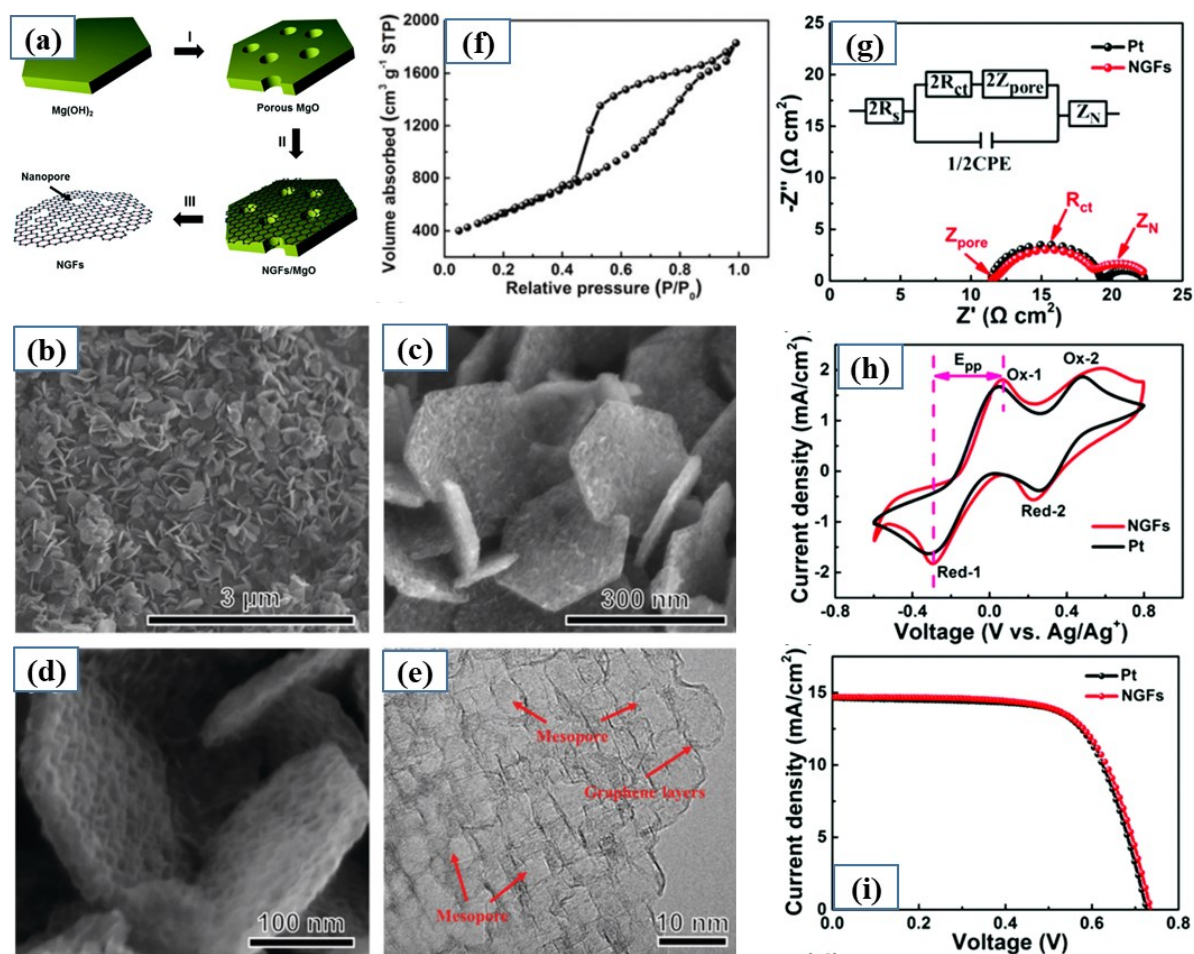
489 Graphene is a flat monolayer of sp^2 hybridized carbon atoms tightly packed into a 2D
490 honeycomb lattice. It is the basic building block of many other carbon allotropes, such as
491 graphite, charcoal, CNTs, and fullerenes (**Fig. 11**).^{102,103} Graphene possesses many exceptional
492 properties: high charge carrier mobility ($\sim 10000 \text{ cm}^2 \text{ V}^{-1} \text{ s}^{-1}$),¹⁸⁰⁻¹⁸² high SSA ($2630 \text{ m}^2 \text{ g}^{-1}$),^{183,184}
493 excellent thermal conductivity ($\sim 3000 \text{ W m}^{-1} \text{ K}^{-1}$),¹⁸⁵ high Young's modulus (~ 1
494 TPa),¹⁸⁶ and high optical transparency (97.7%).¹⁸⁷ Due to these unique properties, graphene
495 has attracted most attention as a DSSC CE material among all of the carbon allotropes.^{188,114}
496 Pristine graphene has zero bandgaps, with no defects and functional groups.¹⁹⁰⁻¹⁹² Like
497 graphite, basal planes of graphene are low free energy active sites. Therefore, pristine graphene
498 acts like inert materials and shows very weak catalytic properties. However, creating defects
499 and surface modification or functionalization with heteroatoms opens the bandgap and, thus,
500 broadens its application in catalysis.



502 **Fig. 11.** Two-dimensional (2D) graphene is the foundation for 0D, 1D, and 3D carbon
503 materials. It can be folded into 0D buckyballs, rolled into 1D nanotubes, or piled into 3D
504 graphite.¹⁹³ Copyright 2007, Nature Publishing Group; reprinted with permission.¹⁵⁸

505

506 The edge sites and topological defects in graphene can tune the electronic structures of
507 basal planes. The edge sites usually include dangling groups and vacancies at the edge of the
508 carbon. The dangling bonds located at the edge of sp²-hybridized carbon basal planes usually
509 are high-energy sites and catalytic centers. Topological defects in nanocarbon materials can
510 occur as nonhexagonal units in the form of patterned defects or a random point mismatches.
511 Different research groups have used graphite and graphene nanoplatelets (GNPs), where edge
512 sites are only catalytic sites, as CEs in DSSCs and studied the effect of edge sites on catalytic
513 activity. The number of edge sites as well as catalytic activity increases as the graphite and
514 GNP particle size decreases.^{44,194,195} To increase topological defects, Kong and Li used a
515 template-directed chemical vapor deposition (CVD) approach to synthesize 3D nanomesh
516 graphene frameworks (NGFs) (**Fig. 12**).¹⁹⁶ To synthesize NGFs, they deposited graphene
517 frameworks on a MgO template, which they removed by hydrochloric acid washing. The result
518 was a 3D nanomesh graphene framework. They used field-emission-scanning electron
519 microscopy (FE-SEM), transmission electron microscopy (TEM), and Brunauer–Emmett–
520 Teller (BET) methods to confirm topological defects and mesoporosity. The synergetic effect
521 of a large surface area integrated with the improved surface edge defects make 3D NGFs a very
522 efficient electrocatalyst toward the I₃⁻ reduction reaction. Indeed, a DSSC with an NGF CE
523 displays a PCE of 7.32%, which is analogous to that of a Pt CE (7.28%).



524

525 **Fig. 12.** (a) Schematic illustration of the nanomesh graphene framework (NGF) preparation
 526 process. (b-d) Scanning electron microscopy (SEM), and (e) transmission electron microscopy
 527 (TEM) images of NGFs, respectively. (f) Nitrogen sorption isotherms of NGFs. (g) Nyquist
 528 plots of symmetric dummy cells, (h) CV curves, and (i) J-V plots of dye-sensitized solar cells
 529 with platinum (Pt) and NGFs electrodes. Copyright 2016, American Chemical Society and The
 530 Royal Society of Chemistry; reprinted with permission.¹⁹⁶

531

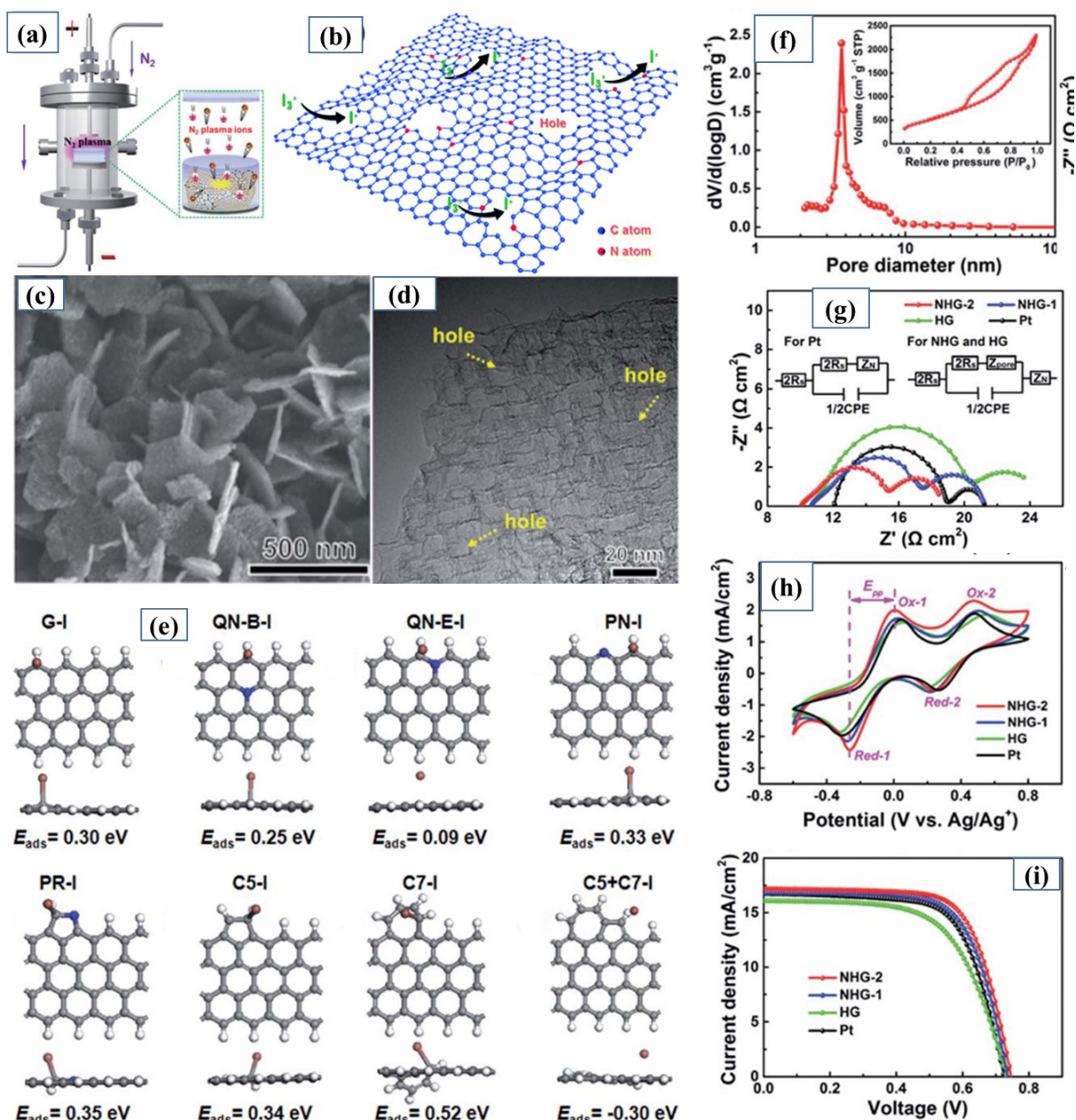
532 To date, different techniques have been used to produce “pristine” graphene, such as
 533 liquid exfoliation,¹⁹⁷ mechanical exfoliation (“Scotch Tape” method),¹⁸⁰ epitaxial growth,¹⁹⁸
 534 and chemical vapor deposition (CVD).¹⁹⁹ Modified Hummer methods are used to produce large
 535 quantities of graphene oxide (GO) through the exfoliation of graphite and subsequent

536 reduction.^{200,201} Graphene produced by this method is known as reduced graphene oxide (rGO);
537 it contains few oxygens as impurities. Xu *et al.* first applied chemically reduced graphene oxide
538 (CR-GO) film as a CE in a DSSC.²⁰² The PCE (2.2%) for CR-GO film as CE is higher
539 compared to bare FTO (PCE = 0.05%), but many developments would be needed to achieve
540 the efficiency of the typical Pt electrode (PCE = 4.0%). Although the oxygen functional group
541 in the graphene structure is considered to be a catalytic active site, highly oxygenated graphene
542 shows low electrical conductivity. Therefore, it is important to optimize the number of oxygen
543 functional groups in rGO. Aksay *et al.* investigated the performance of oxygen-functionalized
544 graphene sheets (OF-GS), synthesized via the thermal exfoliation of GO, as a CE in a DSSC.
545 They found that the charge transfer resistance of OF-GS is 10 times higher compared to that of
546 Pt without any applied potential. However, at the bias potential of 0.8 V, its charge transfer
547 resistance is similar to that of a Pt CE. They also explored the consequence of modifying
548 catalytic functional groups on OF-GS and found that increasing the content of oxygen
549 functional groups may augment the catalytic activity of OF-GS. A C-to-O ratio lower than 13
550 provides optimum efficiency for DSSCs, near to a Pt CE.²⁰³

551 Heteroatom (N, B, S, P, chlorine [Cl], selenium [Se], and Te, among others) doping is
552 also an effective method to enhance the catalytic activity of graphene-based materials.
553 Heteroatoms can be introduced directly into the graphene network by CVD or via a
554 solvothermal process during graphene generation.^{204,205} Furthermore, heteroatoms can be
555 doped through post-treatment of graphene or GO, such as thermal annealing, ball milling, and
556 plasma treatment.^{206–208} N-doped materials are by far the most studied doped graphene
557 materials. To use the synergetic effect of both topological defects and the N heteroatom, Wang
558 and Li synthesized nitrogen-doped holey graphene (NHG) (**Fig. 13**).²⁰⁸ The generated NHG
559 shows high conductivity (3100 S m^{-1}) and a distinctive holey scaffold with abundant edge-
560 induced topological defects and a large surface area ($1874 \text{ m}^2 \text{ g}^{-1}$). Due to these special

561 properties, NHG displays excellent electrocatalytic activity with extraordinary electrochemical
562 stability toward the I^-/I_3^- redox reaction. A DSSC fabricated with an NHG CE shows a PCE of
563 9.07%, which is higher than that of the Pt CE (8.19%). In addition, the authors performed
564 density-functional theory (DFT) calculations to further clarify the core mechanism after this
565 boosting performance. They found that pyridinic and pyrrolic N satisfy the interaction
566 threshold values of E_{ads} (0.33–1.20 eV) for I_3^- reduction. Furthermore, edge-induced
567 topological defects, including five-carbon and seven-carbon rings, can indeed act as
568 catalytically active sites to greatly enhance the catalytic activity for the IRR, especially a seven-
569 carbon ring.

570 To use the synergetic effect of different heteroatoms, multiple heteroatoms such as N, B,
571 P, S, and O, are doped into the graphene structure.^{209–212} The catalytic mechanism of different
572 heteroatoms is considered to be distinctive. Therefore, co-doping is hypothesized to
573 significantly enhance catalytic activity due to the greater influence in energy bandgap, spin,
574 and charge density. Furthermore, co-doping may increase the electrochemical stability and
575 introduce a new route for catalysis, where carbon atoms can also be an active site for
576 catalysts.^{212,213}



577

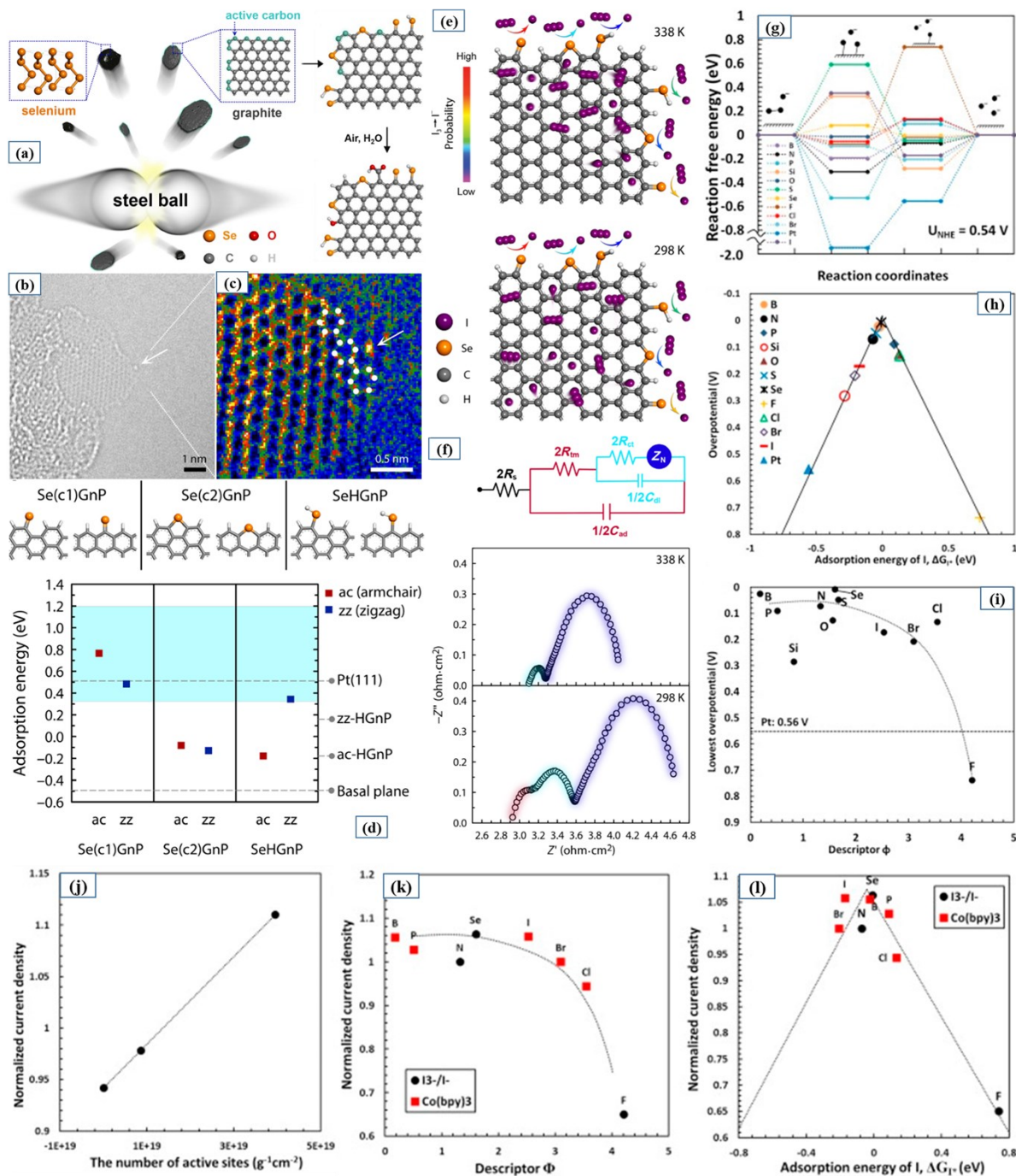
578 **Fig. 13.** (a, b) Schematic diagram of nitrogen-doped holey graphene (NHG) synthesis by N₂
 579 plasma treatment. (c) Scanning electron microscopy (SEM) and (d) high-resolution
 580 transmission electron microscopy (HR-TEM) images of NHG. (e) Different configurations of
 581 the inspected substrates and density–functional theory (DFT) calculations of adsorption energy
 582 for the iodine (I) atom. The white, gray, brown, and blue balls stand for H, C, I, and N, atoms,
 583 respectively. (f) The pore-size distribution of NHG (inset: the nitrogen sorption isotherms). (g)
 584 Nyquist plots of symmetric dummy cells, (h) CV curves, and (i) J-V plots of dye-sensitized

585 solar cells with different electrodes. Copyright 2017, The Royal Society of Chemistry
586 Reprinted with permission.²⁰⁸

587

588 Our group studied a series of edge-functionalized graphene nanoplatelets (EFGnPs) as
589 metal-free CEs in DSSCs with different sensitizers.^{207,214–224} We produced EFGnPs with a
590 simple and environmentally friendly method, namely ball milling the desire substances
591 (halogens, nonmetals, semimetals, or metalloids) with graphite (**Fig. 14a**). Edge-
592 functionalization reduces the van der Waals forces of the graphene layers and facilitates their
593 exfoliation. We utilized atomic-resolution transmission electron microscopy (AR-TEM) to
594 ensure the pristine graphene basal plane and edge-selective Se doping in the SeGnPs (**Fig. 14b**,
595 **c**). Our nonequilibrium Green's function (NEGF) and DFT calculations confirm that the single-
596 coordinated Se-doping (C=Se) for both the zigzag and armchair edges well satisfies the I atom
597 binding criterion, with adsorption energies of 0.48 and 0.77 eV, respectively (**Fig. 14d**).

598 Moreover, we elucidated the I_3^- reduction mechanism using NEGF and DFT calculations.
599 The iodine reduction reaction (IRR) simulated diagram on the SeGnP surface is shown in **Fig.**
600 **14e** based on electrochemical kinetics and DFT and NEGF results. The initial arc is considered
601 due to the transmission resistance (R_m) in addition to capacitance (C_{ad}) originated from the
602 adsorption of I^-/I_3^- on the graphitic basal plane, and the second arc is due to the R_{ct} with double-
603 layer capacitance (C_{dl}) with regard to IRR at the edge of the Se-doped graphene and electrolyte
604 interface (**Fig. 14f**, bottom diagram). We confirmed this by the monitoring the disappearance
605 of the first semicircle at the elevated temperature (**Fig. 14f**, top diagram). With increasing
606 temperature, thermodynamic variations of the graphene and I^-/I_3^- redox couple will rigorously
607 reduce the binding strength between the two and finally start desorption of I^-/I_3^- from the
608 graphitic basal plane.



609

610 **Fig. 14.** (a) Schematic representation of mechanochemically driven selenium-doped graphene
 611 nanoplatelets (SeGnPs). (b) An atomic-resolution transmission electron microscopy (AR-
 612 TEM) image obtained at the edge of SeGnPs. (c) Corresponding inverse fast Fourier transform
 613 (IFFT) images of a graphene edge with armchair and zigzag conformations. (d) We estimated
 614 the adsorption energies of the iodine (I) atom explicitly solvated by acetonitrile molecules for
 615 the representative single-coordinated, double-coordinated, and hydrogenated Se [Se(c1),

616 Se(c2), and SeH, respectively]–doped armchair (ac) and zigzag (zz) graphene edges (top
617 panel), and compared them with the undoped edge and basal plane cases (bottom panel). In the
618 bottom panel, the colored region indicates the IRR activity criterion. (e) The IRR mimetic
619 diagram on the SeGnP surface. (f) Nyquist plots of SeGnP-CEs and their equivalent circuit
620 (EC) at room temperature.²¹⁸ Copyright 2016, American Association for the Advancement of
621 Science; reprinted according to CC BY-SA 3.0). (g) Free energy diagram of platinum (Pt) (111)
622 surface and X-doped graphene. (h) Volcano plots of X-doped graphene and (i) the lowest
623 overpotential of each doped-graphene as a function of descriptor ϕ . Normalized current density
624 is presented as a function of (j) the number of active sites, (k) the descriptors, and (l) the
625 adsorption energy of I, ΔG_{I^*} on the graphene surface. Copyright 2018, Elsevier; reprinted with
626 permission.²²⁵

627

628 Recently, Xia *et al.* proposed a detailed design rule for p-block heteroatom-doped (X)
629 graphene as effective IRR catalysts using DFT calculations (**Fig. 14g–l**).²²⁵ Almost all of the
630 X-doped graphene nanoribbons have comparatively lower adsorption energy with respect to Pt
631 (-0.56 V). A heteroatom with higher electronegativity shows the highest polarization effect in
632 the graphene structure; however, strong electronegativity boosts its interaction with the
633 adsorbates and, consequently, leads to low catalytic activity. Therefore, the electronegativity
634 of the heteroatoms should be modest. In the volcano plots, boron (B)-, N-, O-, S-, and Se-doped
635 graphene sheets are located near the summit, where both the overpotential and the adsorption
636 energy are equivalent to zero; this location signifies the highest catalytic activities.
637 Furthermore, another descriptor:

638

$$\phi = E_X A_X / E_C A_C ,$$

639 where E_X and E_C are electronegativities of the dopant and carbon, A_X and A_C are electron
640 affinities of the dopant and carbon, describes the catalytic activity of doped carbon

641 nanomaterials for IRR in DSSCs. According to this descriptor, a lower ϕ value indicates better
642 catalytic activity. The dopant amount or number of active sites also play a critical role in
643 catalytic activity. The normalized current density increases with more active sites, and catalytic
644 activity is higher than that of Pt when the value of ϕ is smaller than 3. The detailed information
645 of graphene CEs and their electrocatalytic and photovoltaic properties in DSSCs are
646 summarized in **Table 5**.

647 **Table 5** Graphene counter electrodes (CEs) and their electrocatalytic and photovoltaic properties in dye-sensitized solar cells.

CE Materials	SSA (m ² g ⁻¹)	Substrate/Coating technology	Redox Couple	Sensitizer	R_s/R_{ct} (Ω cm ²)	$J_{sc}/V_{oc}/FF$ (mA cm ⁻² /V/%)	η^{CE}/η^{Pt} (%)	Ref	Year
GNB (graphite nanoball)	1329.16	ITO-g/drop casting	I ₃ /I ⁻	N719	-/0.77	16.59/0.70/67.0	7.88/8.38	194	2015
N-GNRs (graphene nanoribbons)		FTO-g/doctor blading	I ₃ /I ⁻	N719	2.58/0.23	15.18/0.78/72.1	8.57/7.84	226	2015
Graphene organogels	998.0	Ti mesh/mechanical pressure	I ₃ /I ⁻	N719	2.71/1.72 [†]	16.34/0.77/58.0	7.20/5.90	227	2016
aGNP	91.0	FTO-g/spray coating	I ₃ /I ⁻	N719	2.68/1.56	22.54/0.73/47.0	7.70/8.10	228	2016
NGF	1920.0	FTO-g/ screen printing	I ₃ /I ⁻	N719	5.74/3.61	14.70/0.736/67.7	7.32/7.28	196	2016
N-GNP	679.15	FTO-g/spray coating	I ₃ /I ⁻	N3	7.7/ 0.6	16.15/0.719/66.0	7.69/8.06	229	2016
3D graphene	575.0	FTO-g/doctor blading	I ₃ /I ⁻	N719	-/-	19.29/0.78/67.0	10.09/7.09	230	2016
rGO(-)/N-rGO(+)	-	FTO-g/spin coating	I ₃ /I ⁻	N719	4.1/9.9	20.59/0.73/48.91	7.03/7.14	211	2016
P-graphene	-	FTO-g/spray coating	I ₃ /I ⁻	N719	6.74/3.87	14.82/0.721/66.3	7.08/7.19	231	2017
GNPs	-	FTO-g/doctor blading	I ₃ /I ⁻	-	6.25/6.0*	15.5/0.69/65.0	7.01/6.23	195	2017
3D graphene	-	FTO-g/doctor blading	I ₃ /I ⁻	N719	-/-	16.60/0.78/64.0	8.25/-	232	2017
N-hole-graphene	-	FTO-g/spray coating	I ₃ /I ⁻	N719	5.03/1.92	17.19/0.74/70.9	9.07/8.19	208	2017
S-doped porous graphene	416	FTO-g/doctor blading	I₃/I⁻	N719	1.78/0.10	16.70/0.75/69.2	8.67/7.88	233	2017
N-graphene	-	Carbon cloth/CVD	I ₃ /I ⁻	N719	-/-	16.09/0.70/67.0	7.53/7.70	205	2018
GNPs	-	FTO-g/doctor blading	I ₃ /I ⁻	N3	5.05/1.68*	17.2/0.68/57.0	6.72/7.26	234	2018
N, S-graphene	-	Carbon cloth/CVD	I ₃ /I ⁻	N719	-/-	15.71/0.80/72.0	9.02/-	235	2019
Graphene	141.7	FTO-g/spray coating	I ₃ /I ⁻	N719	16.36/0.43*	14.71/0.75/68.0	7.48/7.64	210	2019
SnS ₂ @RGO	-	FTO-g/doctor blading	I ₃ /I ⁻	N719	8.98/3.62*	14.80/0.72/67.02	7.12/-	236	2015
Au/GNP	-	FTO-g/drop casting	Co ³⁺ /Co ²⁺	ADEK & LEG4	-/-	18.27/1.014/77.1	14.3/13.	14	2015

In ₂ S ₃ /rGO	-	FTO-g/spray coating	I ₃ /I ⁻	N719	3.11/1.16*	15.48/0.78/66.0	8.01/7.18	²³⁷	2015
rGO-CoS		FTO-g/spray coating & electrodeposition	I ₃ /I ⁻	N719	1.1/1.05*	17.02/0.77/63.0	8.34/7.50	²³⁸	2015
GD-PEDOT:PSS	-	FTO-g/drop casting	I ₃ /I ⁻	N719	-/3.96*	14.70/0.72/70.0	7.36/-	²³⁹	2015
N-graphene/PEDOT	-	FTO-g/drop casting & electro deposition	I ₃ /I ⁻	N719	7.78/1.43	15.60/0.74/72.0	8.30/8.17	²⁴⁰	2015
CoS/rGO	-	FTO-g/electrophoretic deposition	I ₃ /I ⁻	N719	8.02/1.79	18.58/0.77/63.0	9.39/7.34	²⁴¹	2015
Graphene/CNT-Pt	-	FTO-g/spray coating	I ₃ /I ⁻	N719	3.16/0.12	18.57/0.78/67.0	9.70/8.63	²⁴²	2015
CNT/graphene	-	FTO-g/spray coating	I ₃ /I ⁻	N719	-/1.3*	17.03/0.73/61.1	7.62/6.90	²⁴³	2015
CoTe/RGO	58.65	FTO-g/spin coating	I ₃ /I ⁻	N719	5.30/2.93	17.41/0.77/68.5	9.18/8.17	²⁴⁴	2015
PtNP-GDNS	-	FTO-g/drop casting	I₃/I⁻	N719	47.73/1.10	14.13/0.80/0.56	6.35/5.39	²⁴⁵	2015
GO/PEDOT-PSS	-	FTO-g/doctor blading	I ₃ /I ⁻	N719	-/-	13.48/0.77/68.3	7.065/-	²⁴⁶	2015
FGnPs	134.79	FTO-g/spray coating	Co ³⁺ /Co ²⁺	JK-306	-/0.29	14.44/0.96/71.5	10.01/9.61	²⁴⁷	2015
ClGnPs	550.0	FTO-g/spray coating	Co ³⁺ /Co ²⁺	JK-306	2.89/2.24	14.40/0.96/69.2	9.58/9.92	²¹⁹	2015
BrGnPs	595.0	FTO-g/spray coating	Co ³⁺ /Co ²⁺	JK-306	2.74/1.44	14.59/0.97/71.6	10.03/9.92	²¹⁹	2015
IGnPs	668.24	FTO-g/spray coating	Co ³⁺ /Co ²⁺	JK-306	2.74/0.46	14.81/0.98/71.3	10.31/9.92	²¹⁹	2015
RGO/MWCNTs/NiO	-	FTO-g/doctor blading	I ₃ /I ⁻	N719	-/-	16.80/0.71/68.0	8.13/-	²⁴⁸	2015
TiS ₂ -graphene	-	FTO-g/doctor blading	I ₃ /I ⁻	N719	2.32/0.63	17.76/0.72/68.5	8.80/8.00	^{249s}	2016
B, N-graphene	-	FTO-g/doctor blading	I ₃ /I ⁻	N719	4.0/0.3	15.3/0.77/69.0	8.08/6.34	²⁵⁰	2016
Graphene/CNF-Ni	-	FTO-g/spray coating	I ₃ /I ⁻	N719	4.23/0.72	14.31/0.84/60.0	7.14/7.59	²⁵¹	2016
CoN ₄ /graphene	-	FTO-g/spray coating	I ₃ /I ⁻	N719	-/-	17.32/0.72/67.36	8.40/7.98	²⁵²	2016
SbGnPs	302.0	FTO-g/spray coating	Co ³⁺ /Co ²⁺	SGT-021	1.40/0.094	17.21/ 0.93/ 75.53	12.08/ 11.09	²⁰⁷	2016
			I ₃ /I ⁻	N719	-/10.80	18.23/0.74/64.81	8.70/9.98	²¹⁴	2018
SeGnPs	105.69	FTO-g/spray coating	Co ³⁺ /Co ²⁺	SM315	3.20/0.13	16.27/ 0.88/77.0	10.98/10.11	²¹⁸	2016

			I ₃ /I ⁻	N719	2.92/0.23	18.16/ 0.69/ 0.73	9.17/9.07	218	2016
			Co ³⁺ /Co ²⁺	SGT-130		15.60/0.83/78.62	10.18/ 9.77	217	2016
TeGnP _s	590.09	FTO-g/spray coating	Co ³⁺ /Co ²⁺	SM315	1.54/0.15	16.53/0.92/75.9	11.58/11.03	217	2016
			I ₃ /I ⁻	N719	-/0.49	18.20/0.74/75.73	10.25/9.98	214	2018
GO		Cotton fabric/dip coating	I ₃ /I ⁻	N719	3.6/0.62*	14.75/0.66/70.92	6.93/8.44	253	2016
N, P-graphene	325.0	FTO-g/doctor blading	I ₃ /I ⁻	N719	-/-	15.91/0.77/69.97	8.57/7.58	206	2016
MoS ₂ /Graphene sheet	-	FTO-g/CVD	I ₃ /I ⁻	N719	1.6/1.7	16.1/0.66/67	7.1/7.4	254	2016
MoS ₂ /rGO	-	FTO-g/electrodeposition	I ₃ /I ⁻	N719	1.25/0.99	16.96/0.72/65.74	8.01/8.21	255	2016
Fe ₂ O ₃ /graphene	114.0	FTO-g/screen printing	I ₃ /I ⁻	N719	5.99/5.32	15.05/0.73/68.0	8.0/7.7	256	2016
NiCo ₂ S ₄ /graphene		FTO-g/drop casting	I ₃ /I ⁻	N719	8.13/1.72	15.62/0.72/70.5	7.98/8.01	257	2016
Graphene/FeS ₂	-	FTO-g/dip coating	I ₃ /I ⁻	N719	-/-	17.01/0.78/56.0	7.43/6.40	258	2016
g-C ₃ N ₄ /graphene	114.0	FTO-g/doctor blading	I ₃ /I ⁻	N3	-/0.9	14.91/0.72/66.0	7.13/7.37	259	2016
rGO-NiCo ₂ S ₄	-	FTO-g/spin coating	I ₃ /I ⁻	N719	4.85/0.18	16.40/0.75/66.1	8.15/7.23	260	2017
Co _{0.85} Se/RGO	-	FTO-g/spray coating	I ₃ /I ⁻	N719	10.95/0.95	16.01/0.71/69.0	7.81/7.55	261	2017
SrRuO ₃ /GQD	-	FTO-g/spin coating	I ₃ /I ⁻	N719	1.92/4.65	15.62/0.76/68	7.97/7.23	262	2017
PANI/GO	-	FTO-g/doctor blading	I ₃ /I ⁻	N719	3.62/0.87	15.72/0.77/68.0	8.19/7.37	263	2017
CoSe/graphene	-	ITO-g/doctor blading	I ₃ /I ⁻	N719	0.23/0.91 [†]	17.96/0.75/68.8	9.27/7.68	264	2017
Graphene dot/PEDOT:PSS	-	FTO-g/drop casting	I ₃ /I ⁻	N719	-/-	14.70/0.72/70.0	7.36/8.46	265	2017
FeS ₂ /S-graphene	-	-/-	I ₃ /I ⁻		-/11.2*	16.51/0.80/59.0	7.82/8.13	266	2017
TiN/N-graphene	270.0	FTO-g/doctor blading	I ₃ /I ⁻	N719	-/-	15.8/0.79/69.0	8.9/9.0	267	2017
CoFeS ₂ /rGO	-	FTO-g/doctor blading	I ₃ /I ⁻	N719	1.96/0.62	15.85/0.78/71.0	8.82/8.40	268	2017
N,S-graphene	405.0	FTO-g/drop casting	I ₃ /I ⁻	C106	10.93/0.48*	16.86/0.74/74.0	9.40/9.10	212	2017

W ₁₈ O ₄₉ -rGO	-	-/-	I ₃ /I ⁻	N719	-/-	17.18/0.70/60.0	7.23/7.39	269	2017
PtMo/RGO	-	-/-	I ₃ /I ⁻	N719	-/0.63*	18.73/0.74/65.31	9.11/8.03	270	2017
Fe ₃ O ₄ @N-RGO	88.0	FTO-g/doctor blading	I ₃ /I ⁻	N719	2.71/0.09	17.4/0.79/ 66.95	9.26/7.72	271	2018
MoS ₂ .GO/SWCNT	238.25	FTO-g/drop casting	I ₃ /I ⁻	N719	11.98/0.35	18.14/0.74/60.01	8.01/7.21	272	2018
rGO/Mn	-	FTO-g/drop casting	I ₃ /I ⁻	N719	-/-	17.20/0.74/58.0	7.47/7.11	273	2018
PEDOT/rGO	-	FTO-g/electrodeposition	I ₃ /I ⁻	N719	18.88/9.08	15.82/0.73/67.0	7.79/8.33	274	2018
NiCo ₂ S ₄ /rGO	-	FTO-g/drop casting	I ₃ /I ⁻	N719	-/-	17.34/0.76/57.0	7.48/7.24	275	2018
Co ₃ S ₄ /rGO	-	FTO-g/doctor blading	I ₃ /I ⁻	N719	3.05/ 0.145*	14.97/0.755/67.4	8.08/7.62	276	2018
In _{2.77} S ₄ /graphene	78.5	FTO-g/doctor blading	I ₃ /I ⁻	N719	2.8/0.28	14.92/0.74/66.0	7.32/6.48	277	2018
g-C ₃ N ₄ QD@3DG	119.5	FTO-g/doctor blading	I ₃ /I ⁻	N719	19.49/13.5*	15.14/0.719/68.0	7.46/-	278	2018
Graphene/NiMoS	-	Directly/electrodeposition	Gel electrolyte	N719	1.05/0.66*	15.0/0.73/64.0	7.0/5.1	279	2018
MoS ₂ /RGO	-	FTO-g/dip coating	I ₃ /I ⁻	N719	-/-	17.01/0.72/62.0	7.63/7.01	280	2018
Fe ₃ O ₄ @N-rGO	-	FTO-g/doctor blading	I ₃ /I ⁻	N719	3.26/0.14	17.0 /0.77/62.50	8.18/7.17	281	2018
CuS/ZnS@rGO	201.1	FTO-g/doctor blading	I ₃ /I ⁻	N719	4.17/0.21	17.58/0.73/66.0	8.45/7.61	281	2018
C-CW/FeS ₂ @RGO	100.65	FTO-g/doctor blading	I ₃ /I ⁻	N719	8.7/1.17 [†]	17.82/0.68/60.89	7.38/6.24	282	2018
Se-doped graphene	-	FTO-g/doctor blading	I ₃ /I ⁻	N719	0.5/-	17.05/0.74/67.0	8.42/7.74	283	2018
g-C ₃ N ₄ QD@3DG	-	FTO-g/doctor blading	I ₃ /I ⁻	N719	13.5/19.49	15.14/ 0.719/ 0.68	7.46/7.46	278	2018
SWCNH/rGO	-	FTO-g/spray coating	I ₃ /I ⁻	N719	15.0/13.2	17.22/0.73/65.0	8.27/8.36	284	2019
Ru/RGO	-	FTO-g/drop casting	I ₃ /I ⁻	N719	1.12/1.94	13.31/0.62/74.61	6.78/6.20	284	2019
RGO-3DGNs	-	Ni/CVD	I ₃ /I ⁻	N719	-/-	21.0/0.70/66.1	9.79/9.56	285	2019
Graphene/SWCNT	325.81	FTO-g/drop casting	I ₃ /I ⁻	N719	12.88/0.32	20.76/0.76/66.54	10.56/7.64	286	2019
MoS ₂ -rGO	56.90	FTO-g/-	I ₃ /I ⁻	N719	13.37/1.93*	16.75/0.76/61.6	7.83/-	287	2019

Co ₉ S ₈ /RGO	7.3	FTO-g/doctor blading	I ₃ /I ⁻	N719	16.53/0.78*	15.90/0.73/63.0	7.31/7.72	²⁸⁸	2019
CoS _{1.097} /Graphite paper	-	Directly	I ₃ /I ⁻	N719	0.59/1.32	13.96/0.70/71.5	6.99/6.43	²⁸⁹	2019
Graphene	141.7	FTO-g/spray coating	I ₃ /I ⁻	N719	16.36/0.43*	14.71/0.75/68.0	7.48/7.64	²¹⁰	2019

648 Abbreviations: FTO-g, fluorine-doped tin oxide glass; GnP, graphene nanoplatelet; GO, graphene oxide; NGF, nanomesh graphene framework; PEDOT:PSS, poly(3,4-
649 ethylenedioxythiophene) polystyrene sulfonate; rGO, reduced graphene oxide; REG-3DGN, reduced graphene oxide–three-dimensional graphene network; SSA, specific
650 surface area; SWCNT, single-walled carbon nanotube. *Charge transfer unit is Ω , †Charge transfer unit is $\Omega \text{ cm}^{-2}$

651

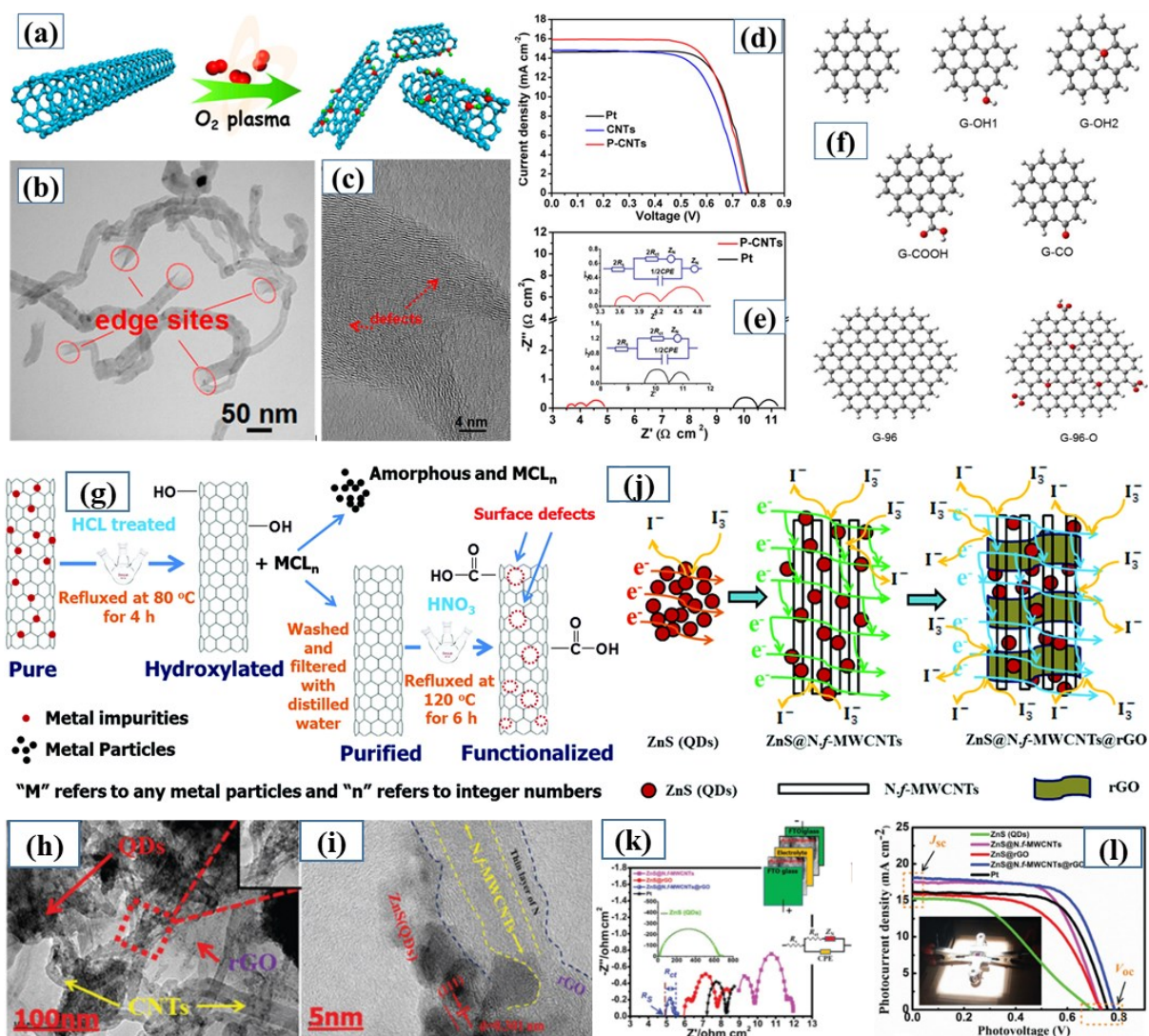
652 **2.2.4. Carbon nanotubes (CNTs) for dye-sensitized solar cells**

653 CNTs are continuous cylinders comprise one or more layers of graphene, with open or
654 closed ends.²⁹⁰ CNTs are associated with the fullerene structural group, also recognized as
655 tubular fullerenes or buckytubes. Considering the number of graphene layers, CNTs are called
656 single-walled carbon nanotubes (SWCNTs) or multi-walled carbon nanotubes (MWCNTs),
657 with a typical diameter of 0.8–2 nm or 5–20 nm, respectively. However, MWCNT diameters
658 can exceed 100 nm. MWCNTs are a collection of nested tubes that are held together by van
659 der Waals forces (similar to graphene sheets). They can have anywhere from 2 to more than
660 100 tubes (walls). CNT lengths range from less than 100 nm to a few centimeters, providing a
661 length-to-diameter ratio equal to 132,000,000:1, considerably higher than any other materials.
662 CNTs are bound with each other through “dispersion forces” and have diverse structures,
663 including a vertically-aligned CNT forest, CNT bundles, horizontally aligned CNTs, a random
664 network of interconnected CNTs, etc.

665 Pristine CNTs are seamless cylinders, but unlike pristine graphene, they have some
666 catalytic activity that originates from metallic impurities, pyramidalization, and misalignment
667 of pi-orbitals and sidewall defects.^{291,292} In 2003, Suzuki *et al.* first used SWCNTs as a CE in
668 DSSCs; they perform better compared to other carbon nanomaterials (carbon filament and
669 carbon nanohorn), with a PCE of 4.5%, which is analogous to the cell-based on Pt-sputtered
670 CE under the same conditions.²⁹³ Double-walled carbon nanotubes (DWCNTs) and triple-
671 walled carbon nanotubes (TWCNTs) are more catalytically active than SWCNTs and
672 MWCNTs.^{292,294} The lower catalytic activity of SWCNTs is likely due to the disruption of the
673 π -electron system and electronic conductivity of SWCNTs by the adsorption of foreign
674 elements during electrocatalytic processes. However, outer wall defects in DWCNTs act as
675 catalytic sites while the inner wall act as a metallic electron conductor.²⁹⁵ With regard to the
676 outer wall and inner tube distance in the range of electron tunneling, the effective electron

677 transmission from the outer wall to the inner tubes may occur through electron tunneling under
678 the electrochemical polarization driving force.²⁹⁶ This electron tunneling process would
679 become less favorable as the number of walls increases due to the decreasing polarization effect
680 across the inner tubes.²⁹² Therefore, CNTs with different walls show pyramidal catalytic
681 activity. Three different DSSCs based on SWCNTs, DWCNTs, and MWCNTs were fabricated
682 by Zhang *et al.* The PCE is comparable: 8.03% (DWCNTs) > 7.61% (SWCNTs) > 7.06%
683 (MWCNTs).

684 CNTs can be metallic or semiconductor, based upon how delocalized electrons dwell in
685 a one-dimensional (1D) density of states. However, SWCNT sidewall functionalization
686 substantially changes electrical properties through the localization of these electrons.
687 Furthermore, sidewall functionalization enhances the dispersibility and processability in
688 aqueous and organic solvents. Different covalent and non-covalent methods are used to
689 functionalize CNTs. Qiu *et al.* reported plasma-activated oxygen-functionalized carbon
690 nanotubes (P-CNTs) with abundant defect sites (**Fig. 15a–f**).²⁹⁷ DFT calculations and
691 experimental results confirmed the positive effects of oxygen toward the electrochemical
692 behaviors of I₃⁻ reduction. Furthermore, strong plasma activation cleaves the surface of the
693 CNT sidewall to generate more exposed open ends and edges. Notably, a DSSC with a P-
694 CNT CE shows a high PCE of 8.35%, clearly higher than the Pt CE performance (8.04%).
695 DFT calculations revealed that the oxygen species on the surface hydroxyl groups and the
696 carbonyl groups reduce the ionization energy of the P-CNTs through the adjustment of
697 electronic properties of neighboring carbon atoms. This efficiently decreases the charge
698 transfer resistance and hastens electron transfer.



699

700 **Fig. 15** (a) Schematic representation for O-functionalized plasma-activated carbon nanotube
 701 (P-CNT) synthesis. (b, c) High-resolution transmission electron microscopy (HR-TEM) image
 702 of P-CNTs. (d) J-V curves of dye-sensitized solar cells (DSSCs) and (e) Nyquist plots of
 703 symmetric dummy cells with platinum (Pt), carbon nanotube (CNT), and P-CNT electrodes.
 704 (f) Different atomic models diagram for O-functionalized P-CNTs. Copyright 2018, American
 705 Chemical Society; reprinted with permission.²⁹⁷. (g) Schematic illustration of the
 706 functionalization of multi-walled carbon nanotubes (MWCNTs). (h, i) HR-TEM images of
 707 ZnS@N.f-MWCNTs composite wrapped with reduced graphene oxide (rGO). (j) Increased
 708 performance mechanism of the ZnS@N.f-MWCNTs@rGO electrode. (k) Nyquist plots of

709 symmetric dummy cells and (l) J-V plots of DSSCs with different electrodes. Copyright 2020,
710 The Royal Society of Chemistry; reprinted with permission.²⁹⁸

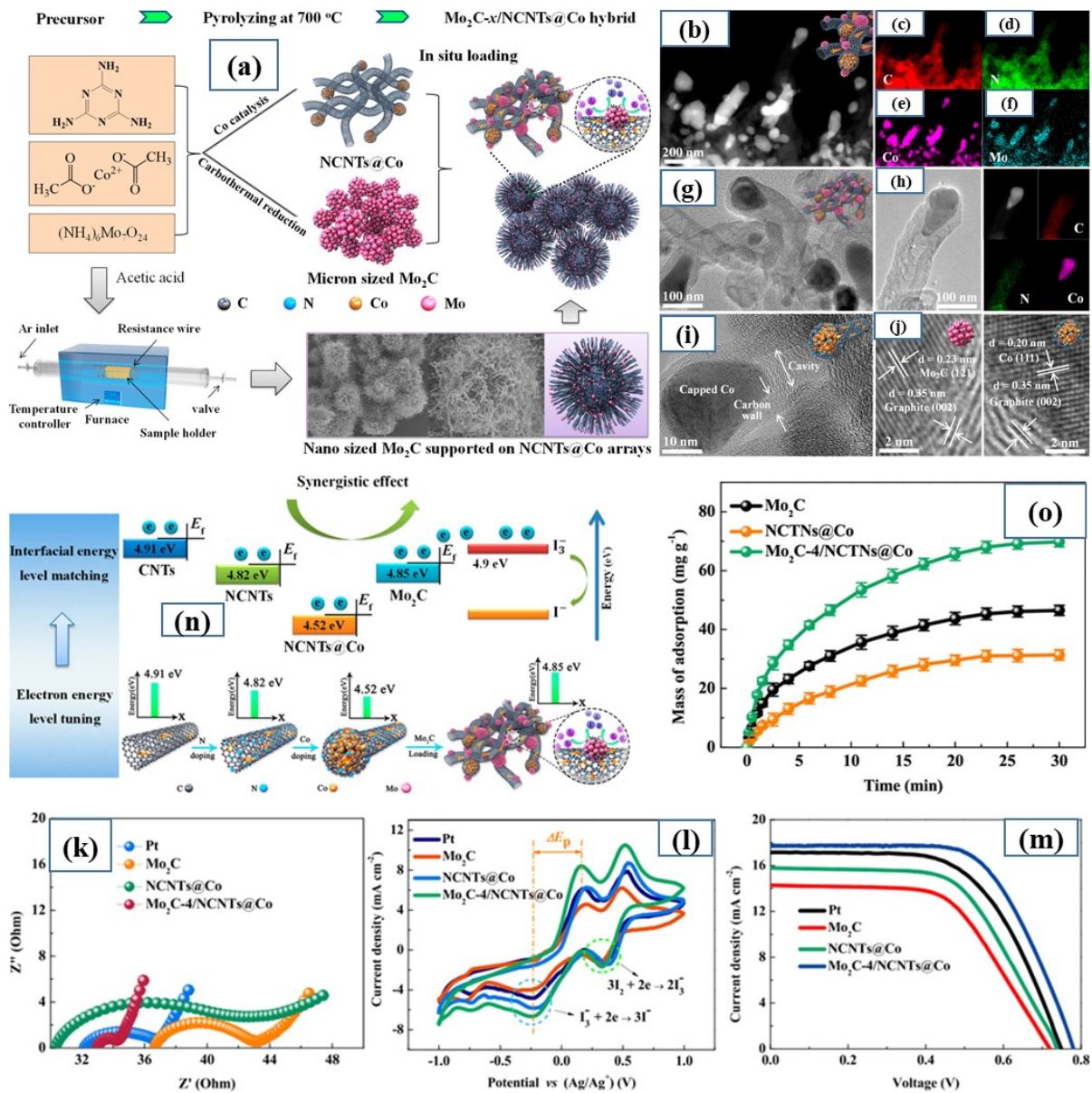
711

712 Unlike atomic size and electronegativity, the integration of heteroatoms will result in
713 charge rearrangement of adjacent carbon matrix and distort the lattice order, phenomena that
714 activate unique physicochemical properties. Among various doping elements, electron-rich
715 N and electron-deficient B are believed to be a likely candidate for the efficient chemical-
716 doping of carbon materials. This effect may be due to the lone-pair electron in N and electron
717 vacancy in B, which easily allows to polarize the chemically inactive sp^2 carbon network and
718 induce sufficient free-flowing π electrons to act as catalysts for electrochemical applications.
719 Besides, the incorporation of N and B may considerably enhance the conductivity of carbon
720 materials by escalating the density of n- and p-type charge carriers, respectively. To use the
721 synergetic effect of high surface area, edge defects, and heteroatom, Wu *et al.* prepared
722 bamboo-like N-doped carbon nanotubes (N-CNTs) by straight pyrolysis of nanostructured
723 Prussian blue analog (metal hexacyanoferrates). The pyrolysis temperature helped control the
724 structure of the resulting carbon materials. At 700°C, the authors obtained bamboo-like N-
725 CNTs with the desired catalytic properties.²⁹⁹

726 Chemically altering the CNT surface and incorporating low-cost metal-based
727 nanoparticles is another feasible way to improve the CNT catalytic activity. Specifically,
728 transition metals can influence the carbon structure: They can adjust the electronic structure,
729 WF, and electrical conductivity of carbon materials by electron-donating effect through
730 incompletely filled 3d orbital. Recently, NiS, FeS, FeC, CoTe, CoS, CoSe, and Co₂O₃ have
731 been reported as an efficient CE for a DSSC.^{300–306} Li *et al.* reported rGO wrapped N-doped
732 functionalized MWCNTs incorporated with zinc sulfide quantum dots (ZnS QDs) (**Fig. 15g–**

733 i).²⁹⁸ Initially, they functionalized MWCNTs with –COOH and –OH groups by using a
734 refluxing strategy. The functional groups act as sites for the nucleation of the ZnS(QDs) as
735 oxygen-containing groups. The ZnS@N.f-MWCNTs@rGO have an intertwined distinctive
736 hollow structure with a particular surface area that is suitable for use as a CE. The
737 electrochemical performance showed that at the electrolyte/CE interface, the ZnS@N.f-
738 MWCNTs@rGO electrode has a lower charge transfer resistance (R_{ct}) and a greater catalytic
739 ability than naked ZnS QDs.

740 Chen *et al.* reported Co-embedded and N-CNTs supported by Mo₂C nanoparticles
741 (Mo₂C/N-CNTs@Co) heterostructure as a highly efficient and stable electrocatalyst (Fig.
742 16).³⁰⁷ These authors used a simple and straightforward method to synthesize Mo₂C/N-
743 CNTs@Co by *in situ* metal precursor carbonization and nitridation, using cobalt acetate as a
744 Co precursor, (NH₄)₄Mo₇O₂₄ as a Mo precursor, and melamine as a C/N precursor. The DSSC
745 with a Mo₂C/N-CNTs@Co CE shows a high PCE of 8.82% and outstanding electrochemical
746 stability, with a remaining efficiency of 7.95% after constant illumination for 200 h; these
747 values are better than the DSSC with a Pt CE. Furthermore, the authors calculated higher
748 catalytic property of Mo₂C/N-CNTs@Co with DFT. Specifically, the WF of Co-embedded and
749 N- CNTs is correspondingly regulated from 4.91 to 4.52 eV with an electron-donating effect.
750 In addition, Mo₂C nanoparticles display a Pt-like 4d electronic configuration and present a
751 thriving matched WF (4.85 eV) with I/I₃⁻ redox couples (4.90 eV).



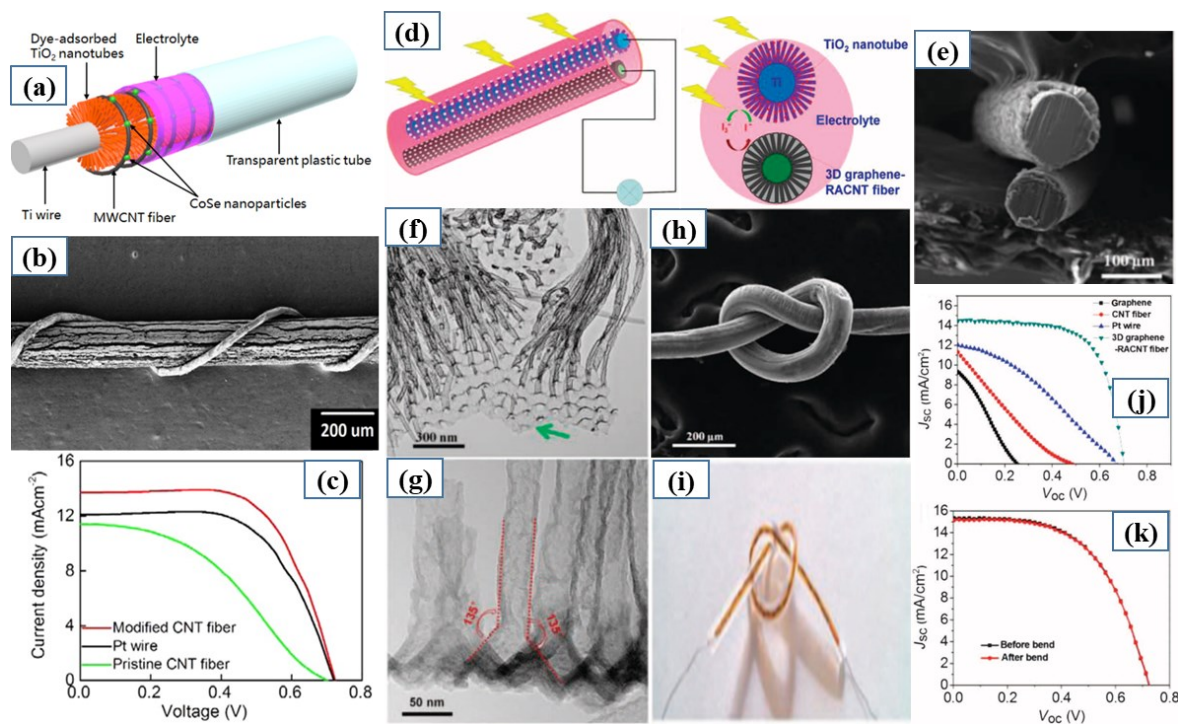
753

754 **Fig. 16.** Schematic presentation of the synthesis of $\text{Mo}_2\text{C}-x/\text{NCNTs}@Co$ hybrids (a). Annular
 755 dark-field transmission electron microscopy (TEM) images (b, g-j) and TEM mapping (c-f, h)
 756 of the $\text{Mo}_2\text{C}-4/\text{NCNTs}@Co$ hybrid and single NCNTs@Co in $\text{Mo}_2\text{C}-4/\text{NCNTs}@Co$. (k)
 757 Nyquist plots of symmetric dummy cells. (l) CV curves and (m) $J-V$ plots of DSSCs with
 758 different electrodes. (n) Schematic presentation of interfacial energy level matching of
 759 $\text{Mo}_2\text{C}/\text{NCNTs}@Co$ hybrid. (o) The adsorption capacity of I_3^- on $\text{Mo}_2\text{C}-4/\text{NCNTs}@Co$,

760 NCNTs@Co, and Mo₂C. (m) J–V curves of dye-sensitized solar cells based on different
761 electrodes. Copyright 2019, American Chemical Society; reprinted with permission.³⁰⁷

762

763 The elastic modulus and tensile strength of the CNTs are very high due to covalent
764 sp² bonds that form between the individual carbon atoms. Espinosa *et al.* observed that elastic
765 modulus and tensile strength of the cross-sectional area for individual MWNTs are 1 TPa and
766 100 GPa, respectively.³⁰⁸ The higher elastic modulus and tensile strength of the CNTs makes
767 them favorable for producing flexible and stretchable DSSCs. Different groups have recently
768 reported wire-like DSSCs with high photovoltaic efficiency that contain different structural
769 configurations by exploiting the 1D and flexible properties of CNTs.^{309–311} Ali *et al.*³⁰⁹ used
770 TiO₂ nanotubes and TiO₂ NP–modified Ti-wire as a working electrode and twisted a
771 CoSe@MWCNTs composite fiber as a CE around it. They sealed the resultant wire-like
772 DSSC into a transparent plastic tube with redox electrolyte (**Fig. 17a-c**). Xue *et al.*³¹⁰ utilized
773 TiO₂ nanotubes and TiO₂ NP–modified photoanode and a 3D graphene–modified CNT fiber
774 CE sidewise in the transparent fluorinated ethylene propylene (FET) tube containing the
775 electrolyte (**Fig. 17d-k**). Notably, the photovoltaic efficiency of the wire-like DSSCs
776 fabricated with modified CNT fiber CE is much higher compared to the Pt wire CE. The
777 detailed information of carbon nanotube counter electrodes and their electrocatalytic and
778 photovoltaic properties in DSSCs are summarized in **Table 6**.



779

780 **Fig. 17** (a) Schematic illustration of a wire-shaped dye-sensitized solar cell (DSSC) that
 781 comprises a working electrode on the inside and a counter electrode (CE) on the outside. (b) A
 782 scanning electron microscopy (SEM) image of electrochemically modified Ti wire twisted with
 783 a multi-walled carbon nanotube (MWCNT) fiber. (c) J-V curves of fiber-shaped DSSCs with
 784 different CEs. Copyright 2016, American Chemical Society; reprinted with permission.³⁰⁹ (d)
 785 Schematic illustration of wire-shaped DSSC containing a working electrode with a CE
 786 alongside it. (e) A SEM image of the cross-section view of the wire-shaped DSSC. (f, g) A
 787 transmission electron microscopy (TEM) image of a graphene sheet connected to the open tips
 788 of radially aligned CNTs. (h, i) An SEM image of a knot of the graphene-CNT fiber, as well
 789 as a knot of the flexible DSSC. (j) A J-V curve of DSSCs with different electrodes and (k) a
 790 J-V curve of a DSSC before and after bending with graphene-CNT fiber electrode.³¹⁰ Copyright
 791 2015, American Association for the Advancement of Science; reprinted under CC BY-SA 3.0.

793 **Table 6** Carbon nanotube (CNT) counter electrodes (CEs) and their electrocatalytic and photovoltaic properties in dye-sensitized solar cells.

CE materials	SSA (m ² g ⁻¹)	Substrate/coating technology	Redox couple	Sensitizer	R_s/R_{ct} (Ω cm ²)	$J_{sc}/V_{oc}/FF$ (mA cm ⁻² /V/%)	η^{CE}/η^{Pt} (%)	Ref	Year
N-CNT	261	FTO-g/electrophoretic deposition	I ₃ ⁻ /I ⁻	N719	26/2.1*	14.35/0.726/71.8	7.48/7.12	299	2016
CNH	-	FTO-g/drop casting	I ₃ ⁻ /I ⁻	N719		16.14/0.79/61.0	7.70/7.92	312	2016
MWCNT		Carbon fabric/spin coating	Quasi-solid electrolyte	N719	3.84/1.03*	15.34/0.72/76.16	8.44/ 8.90	313	2017
O-CNT	112	FTO-g/doctor blading	I ₃ ⁻ /I ⁻	N719	-/-	15.92/0.76/69.2	8.35/8.04	297	2019
SWCNT		FTO-g/screen printing	Cu ²⁺ /Cu ¹⁺	Y123	2.4/0.68	11.0/0.97/65.3	7.0/6.2	314	2019
CNT	250	FTO-g/-	I ₃ ⁻ /I ⁻	N719	-/-	20.0/0.64/69.0	8.8/8.7	315	2019
N-doped graphene/CNT		FTO-g/spin coating	I ₃ ⁻ /I ⁻	N719	-/1.78	16.23/0.77/54.2	6.74/ 6.89	316	2015
CNT/PPy/PEDOT		Carbon/electrodeposition	I ₃ ⁻ /I ⁻	N719	16.72/2.15*	14.99/0.76/63.0	7.17/7.20	317	2015
CNT ⁻ /CNT ⁺		FTO-g/dip coating	I ₃ ⁻ /I ⁻	N719	-/-	18.03/0.71/71.0	9.13/8.40	318	2015
CNT/Graphene	526.91	Al wire/CVD	I ₃ ⁻ /I ⁻	N719	-/-	14.50/0.70/67.0.	6.80/2.74	310	2015
CNT/Graphene		Cu-foil/CVD	I ₃ ⁻ /I ⁻	N719	-/-	16.6/0.72/66.0	7.9/7.0	319	2015
NiO-NF/MWCNT	111.2	FTO-g/doctor blading	I ₃ ⁻ /I ⁻	N719	7.94/0.54*	18.54/0.64/63.9	7.63/ 6.72	320	2015
MWCNT/enzyme		FTO-g/tape casting	I ₃ ⁻ /I ⁻	N719	4.41/0.7	14.57/0.69/74.48	7.52/8.00	321	2015
MoS ₂ /RGO-CNTs		FTO-g/electrophoretic deposition	I ₃ ⁻ /I ⁻	N719	10.18/1.65	14.59/0.76/67.0	7.46/ 7.23	322	2015
NG/CNT-OH	343.02	PET/-	I ₃ ⁻ /I ⁻	N719	4.8/1.93	13.62/0.71/65.31	6.36/ 5.74	323	2016
AC/MWCNT		FTO-g/tape casting	I ₃ ⁻ /I ⁻	N719	4.05/0.30*	16.07/0.75/83.0	10.05/ 9.30	324	2016
PPy/MWCNT		FTO-g/spin coating & electrodeposition	I ₃ ⁻ /I ⁻	N719	6.8/38.15	17.56/0.74/55.0	7.15/7.76	325	2016
g-C ₃ N ₄ /MWCNT		FTO-g/doctor blading	I ₃ ⁻ /I ⁻	N3	8.2/1.05	14.20/0.72/62.0	6.34/6.84	326	2016
CNT/Pt	482.4	FTO-g/-	I ₃ ⁻ /I ⁻	N719	-/-	16.57/0.78/70.0	8.77/7.01	327	2016

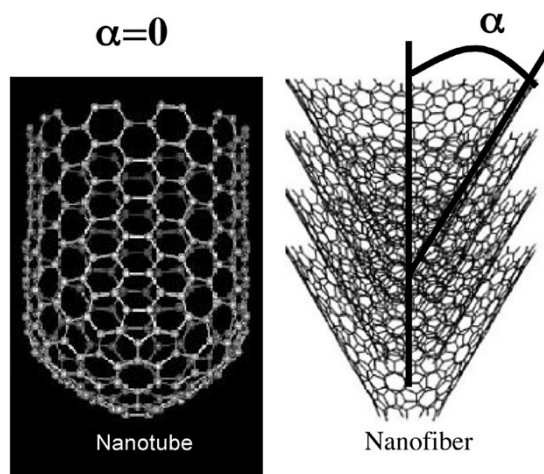
MWCNTs/TiO ₂		FTO-g/doctor blading	I ₃ ⁻ /I ⁻	N719	-/-	20.1/0.66/60.0	7.95/7.38	328	2016
CNTs/VS ₂		FTO-g/doctor blading	I ₃ ⁻ /I ⁻	N719	6.83/2.85	15.57/0.75/68.2	8.02/ 6.49	329	2017
PPy/MWCNT		FTO-g/spin coating & electrochemical deposition	I ₃ ⁻ /I ⁻	N719	-/-	17.50/0.76/53.0	7.07/-	330	2017
MoS ₂ /CNT		FTO-g/CVD & electrochemical deposition	I ₃ ⁻ /I ⁻	N719	13.52/1.09	16.65/0.74/66.0	7.83/7.15	331	2017
Co-Ni/MWCNTs		FTO-g/spray coating & PLD	I ₃ ⁻ /I ⁻	N719	-/-	14.68/0.63/72.2	6.68/6.22	332	2017
BCNT		ITO-g/drop casting	I ₃ ⁻ /I ⁻	N719	-/0.28	17.3/0.72/63.0	7.91/8.03	333	2017
CN _x /CNT		FTO-g/doctor blading	I ₃ ⁻ /I ⁻	N719	-/6.15	16.30/0.73/61.5	7.38/7.13	334	2017
Ni-NCNTs	123	FTO-g/doctor blading	I ₃ ⁻ /I ⁻	N719	13.51/1.30	16.64/0.79/68.0	8.94/7.53	335	2017
CoNi@CNTs		FTO-g/spin coating	I ₃ ⁻ /I ⁻	N719	7.84/1.38	18.3/0.76/65.0	9.04/7.88	336	2017
f-MC/MWCNT	735.3174	FTO-g/doctor blading	gel electrolyte	N719	2.7/0.6	15.9/0.714/74.2	8.42/8.11	133	2017
N-O-GQD/CNT/CF		ITO-g/electrophoretic deposition	I ₃ ⁻ /I ⁻	N719	1.38/0.30	15.77/0.81/60.0.	7.68/6.90	337	2017
PANI/GNP/MWCNT		FTO-g/electrophoretic deposition	I ₃ ⁻ /I ⁻	N719	-/-	18.21/0.78/54.0	7.67/7.62	338	2017
Pt NPs@f-MWCNT		ITO-g/drop casting	I ₃ ⁻ /I ⁻	N719	11.39/0.12	18.59/0.71/63.0	8.31/6.59	339	2017
CuMnSnS ₄ /CNT		FTO-g/doctor blading	I ₃ ⁻ /I ⁻	N719	1.99/1.08	16.53/0.75/72.0	8.97/8.37	340	2017
Fe _{1-x} S/Fe ₃ C-NCNTs	72.0	FTO-g/doctor blading	I ₃ ⁻ /I ⁻	N719	12.31/0.78*	16.19/0.80/67.0	8.67/7.75	341	2018
Ni/MWCNT		Ni-foil/spray coating	gel electrolyte	N719	0.42/ 0.12	14.7/0.69/73.0	7.43/6.72	341	2018
BCNT		-/-	I ₃ ⁻ /I ⁻	N719	-/0.26	16.2/0.70/63.0	7.17/7.98	342	2018
MWCNTs		FTO-g/drop casting	gel electrolyte	N719	-/-	23.22/0.58/52.0	7.07/5.75	343	2018
CNT-CoS ₂		FTO-g/-	I ₃ ⁻ /I ⁻	N719	4.77/3.22	16.51/763/71.0	8.92/7.32	305	2018
CoSe ₂ /MWCNTs		FTO-g/doctor blading	I ₃ ⁻ /I ⁻	N719	2.58/0.97	16.61/0.75/70.0	8.72/8.14	306	2018

Co@N-CNT		FTO-g/spin coating	I ₃ /I ⁻	N719	8.87/0.11*	15.87/0.72/71.1	8.18/7.54	344	2018
CNT-Ni(OH) ₂		FTO-g/CBD & CVD	I ₃ /I ⁻	N719	7.95/1.55*	15.48/0.71/67.0	7.36/6.65	345	2018
Mo ₂ C/NCNTs@Co	164	FTO-g/doctor blading	I ₃ /I ⁻	N719	15.85/1.34*	17.73/0.78/64.0	8.82/7.69	307	2019
CoTe ₂ @NCNTs and		FTO-g/spin coating	I ₃ /I ⁻	N719	14.83/0.40*	17.89/0.79/64.0	9.02/8.03	300	2019
MWCNT/PEDOT:PSS		FTO-g/spin coating	I ₃ /I ⁻	-	-/-	13.40/0.80/61.7	6.70/7.60	346	2019
Ni ₃ S ₂ @MWCNT	-	-/-	I ₃ /I ⁻	N719	8.01/7.25*	17.25/0.75/56.0	7.48/7.24	347	2019
Ni MWCNT	180.85	FTO-g/doctor blading	I ₃ /I ⁻	N719	-/-	22.55/0.76/57.0	9.72/8.85	348	2019
MWCNT		FTO-g/doctor blading	I ₃ /I ⁻	N719	-/-	15.40/0.75/62.0	7.15/6.33	349	2019
CoSe@NPC/NCNT	55.6	FTO-g/doctor blading	I ₃ /I ⁻	N719	10.30/3.56*	16.00/0.71/67.0	7.58/7.27	302	2019
Ru/MWNT		FTO-g/spin coating	I ₃ /I ⁻	N719	-/-	12.5/0.83/65.9	6.80/6.90	350	2019
Co ₃ O ₄ @f-MWCNT		FTO-g/doctor blading	I ₃ /I ⁻	N719	2.71/0.15	17.09/0.75/65.7	8.42/7.81	301	2019
NiCoP-CNT		FTO-g/doctor blading	I ₃ /I ⁻	N719	14.01/ 5.41	13.94/0.75/68.0	7.24/7.12	351	2019
NiS/CNTs		FTO-g/-	I ₃ /I ⁻	N719	5.31/0.28	22.87/724/65.0	10.82/8.03	304	2019
ZnS@N.f-MWCNTs	306.24	FTO-g/doctor blading	I ₃ /I ⁻	N719	2.48/0.1	18.12/0.78/66.5	9.40/8.20	298	2020

794 Abbreviations: CBD, chemical bath deposition; CVD, chemical vapor deposition; FTO-g, fluorine-doped tin oxide glass; GNP, graphene nanoplatelets; IDO-g, indium tin oxide
795 glass; MW, multi-walled; PANI, polyaniline; PEDOT:PSS, PPy, poly(3,4-ethylenedioxythiophene) polystyrene sulfonate; polypyrrole; SSA, specific surface area; SW, single-
796 walled. *Charge transfer unit is Ω ,

797 2.2.5. Carbon nanofibers (CNFs) for dye-sensitized solar cells

798 CNFs comprise MWCNTs, where stacked graphene layers are organized as cones, cups,
799 or plates (**Fig. 18**). Unlike MWCNTs, stacked graphene layers in CNFs are less ordered and
800 mostly graphitic. Depending upon the CNF type, diameters range from 50–200 nm (almost 10
801 times larger than MWCNTs), and the walls are thicker compared to CNTs.



802

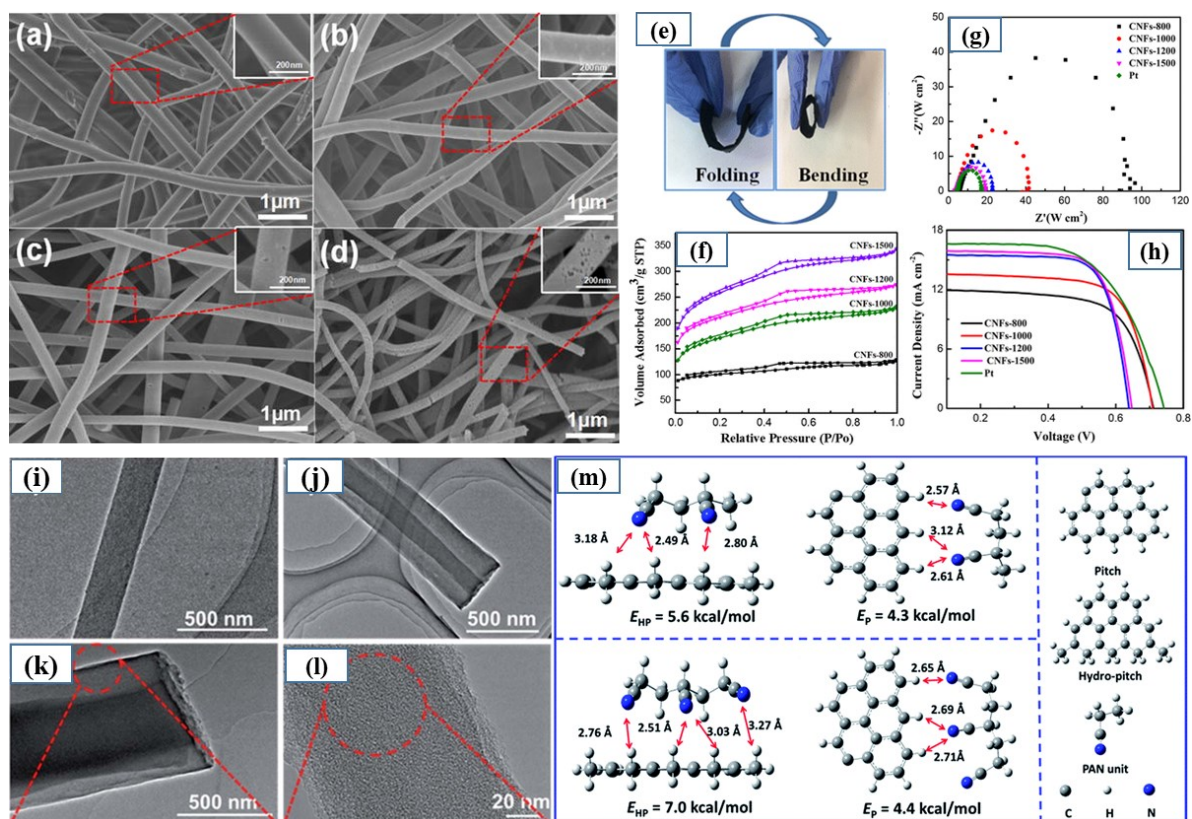
803 **Fig. 18** Structural dissimilarities between carbon nanotubes and carbon nanofibers. Copyright
804 2007, IOP Publishing; reprinted with permission.³⁵²

805

806 CNFs have high mechanical strength, high electrical conductivity, a large surface area,
807 and high catalytic activity, all of which are almost comparable to CNTs.^{352–354} However, the
808 CNF synthetic process is easier and cheaper compared to CNTs. Hence, CNFs are a hopeful
809 candidate as a CE for DSSCs.³⁵⁵ Electrospinning (ES)³⁵⁶ and vapor deposition, including
810 catalytic chemical vapor deposition (CCVD),³⁵⁷ arc discharge,²⁹⁰ and radio frequency glow
811 discharges,³⁵⁸ are usually applied to synthesize CNFs. Among these methods, ES and CCVD
812 are the most widely used methods to generate CNFs. Joshi *et al.*³⁵⁵ first employed ES CNFs as
813 an electrocatalyst and low-cost alternative to Pt for I_3^- reduction in DSSCs. The CNF CE
814 exhibits low charge transfer resistance, high capacitance, and fast reaction rates for I_3^-

815 reduction. The CNF-based DSSC reaches an η of 5.5% under one sun illumination. These
816 authors also noted that the FF and η may be significantly enhanced by using thinner and highly
817 porous CNFs to reduce the thickness of the CE.

818 The CNF catalytic properties rely on the degree of graphitization, structural defects,
819 functional heteroatoms, and surface area. Highly graphitic CNFs feature a well-developed
820 graphene orientation in CNFs structure, and high-temperature heat treatments can considerably
821 prompt the orientation of the graphene layer and increase the extent of graphitization of CNFs.
822 Liu and Wang synthesized a flexible CNF mat using alkaline lignin-based solutions containing
823 poly (vinyl alcohol) via ES (**Fig. 19a–h**).³⁵⁹ They examined the effect of carbonization
824 temperature. Notably, graphitizing degree and SSA remarkably increase when carbonization is
825 performed $> 1000^{\circ}\text{C}$. The CNF obtained at 1500°C as binder-free CE in DSSC shows the
826 maximum PCE (up to 7.60%), comparable to that of the DSSCs with a typical Pt CE (7.67%).
827 However, the porosity in CNFs decreases the conductivity due to decreasing contact between
828 the carbon crystalline domain. To increase the catalytic activity and conductivity, Qiu *et al.*
829 reported coaxial CNFs synthesized from hydrogenated pitch and polyacrylonitrile (PAN) by
830 ES (**Fig. 19i–m**).³⁶⁰ Planar aromatic hydro-pitch (HP) molecules are more easily transformed
831 into an optically anisotropic, graphitizable carbon structure, while PAN forms a carbonaceous
832 structure with a high N content and abundant defects. Benefiting from the diverse
833 configuration, their procedure produced a novel coaxial core/shell structure, where HP provides
834 the core phase structure and PAN yields the outer shell phase. CNFs containing dual phases
835 show unique characteristics as CEs in DSSCs: The outer shell provides active sites for
836 catalyzing I_3^- reduction and the core phase mediates charge transport.



837

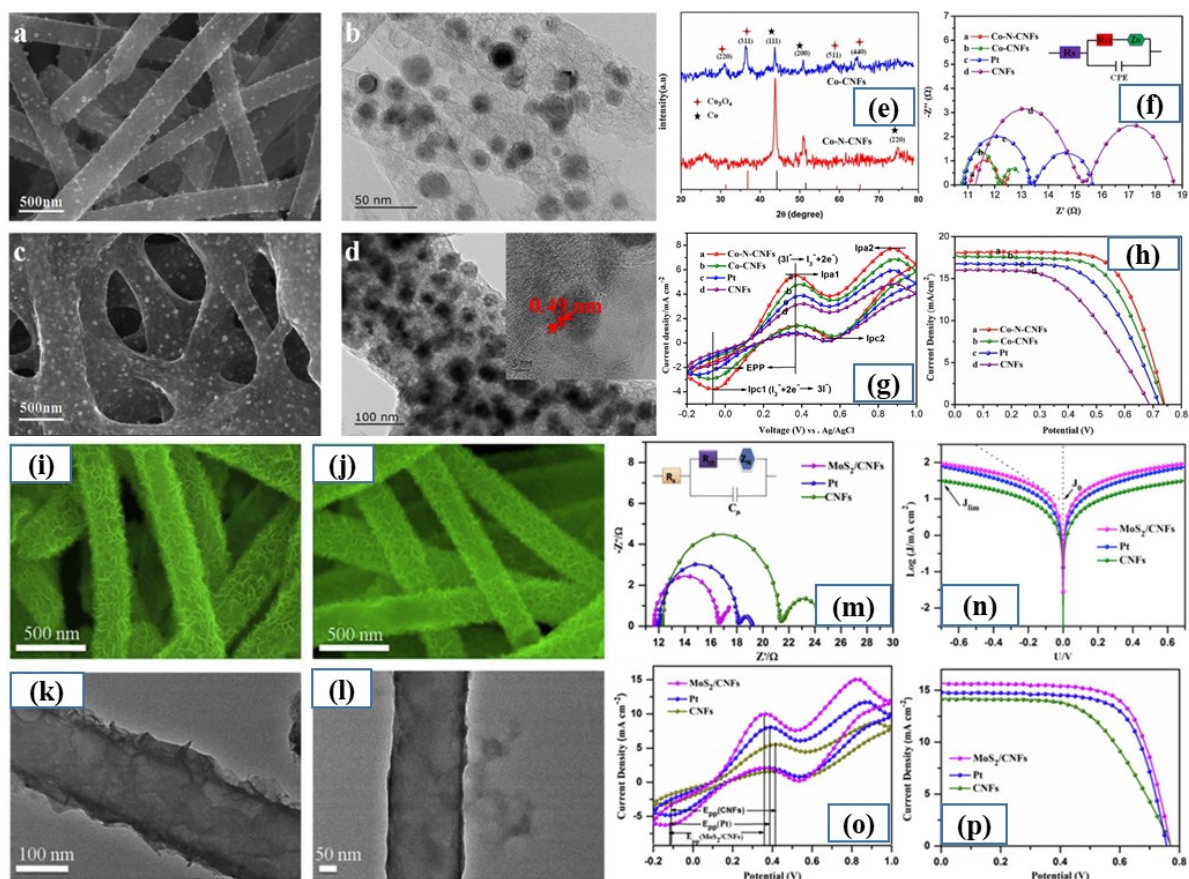
838 **Fig. 19** Scanning electron microscopy (SEM) images of carbon nanofibers (CNFs) prepared at
 839 varying carbonization temperatures: (a) 800°C, (b) 1000°C, (c) 1200°C, and (d) 1500°C. (e)
 840 Flexibility of CNF mats. (f) N₂ adsorption/desorption isotherms of different CNFs. (g) Nyquist
 841 plots of electrochemical impedance spectroscopy (EIS) for dye-sensitized solar cells (DSSCs)
 842 measured at open-circuit voltage under one sun illumination. (h) J-V curves of the DSSCs with
 843 different counter electrodes (CEs). Copyright 2018, Springer-Verlag; reprinted with
 844 permission.³⁵⁹ (i-l) Transmission electron microscopy (TEM) images of coaxial CNFs. (m) The
 845 three-dimensional arrangements and binding energies between pitch molecules and
 846 polyacrylonitrile (PAN) units. Copyright 2018, The Royal Society of Chemistry; reprinted with
 847 permission.³⁶⁰

848

849 CNFs are considered to be one of the best supports for catalytic NPs and polymers due to
 850 their low cost, high surface area, thermal and electrical conductivities, and stability. Many

851 researchers have reported that composite CNFs as CEs in DSSCs to increase the catalytic
852 activity and photovoltaic efficiency.^{361–365} Several methodologies have been used to synthesize
853 CNF-supported catalytic NPs.^{366–368} Zhang reported *in situ* synthesis of Co and N-doped carbon
854 nanofibers (Co-N-CNFs) from PAN and $\text{Co}(\text{NO}_3)_2 \cdot 6\text{H}_2\text{O}$ via ES (**Fig. 20a–h**).³⁶⁶ The N-
855 heteroatom plays a critical role in the nucleation and growth mechanism of metallic NPs,
856 discussed in the previous section. Furthermore, the N-heteroatom increased the hydrophilic
857 nature and interaction between Co NPs and the carbon substrate. This factor offers additional
858 advantages to the catalytic behavior of Co-N-CNFs. DSSCs fabricated using Co-N-CNFs-
859 based CE display a high PCE of 9.05% at one sun illumination, which is significantly higher
860 than that of the most commonly used Pt CE (7.1%).

861 Transition metal sulfides are considered to be a proficient alternative to valuable Pt metals
862 due to their low cost, exceptional redox properties, and high conductivity. High catalytic
863 activity of transition metal sulfides are expected because of their high SSAs and unique
864 structures, as well as their similar electronic properties with Pt. Recently, Wu *et al.* prepared
865 flower-like nanosheet molybdenum sulfide on carbon nanofibers (MoS_2/CNFs) via
866 impregnation of Mo and S precursor into the CNFs, followed by hydrothermal synthesis of
867 MoS_2 (**Fig. 20i–p**).³⁶⁹ The MoS_2/CNF composites exhibit good performance as a CE in a
868 DSSC. A DSSC with MoS_2/CNF CEs delivers a PCE of 8.46%, which is even higher than that
869 of the DSSC with CNF CE (6.59%) or Pt CE (7.65%) in the identical conditions.



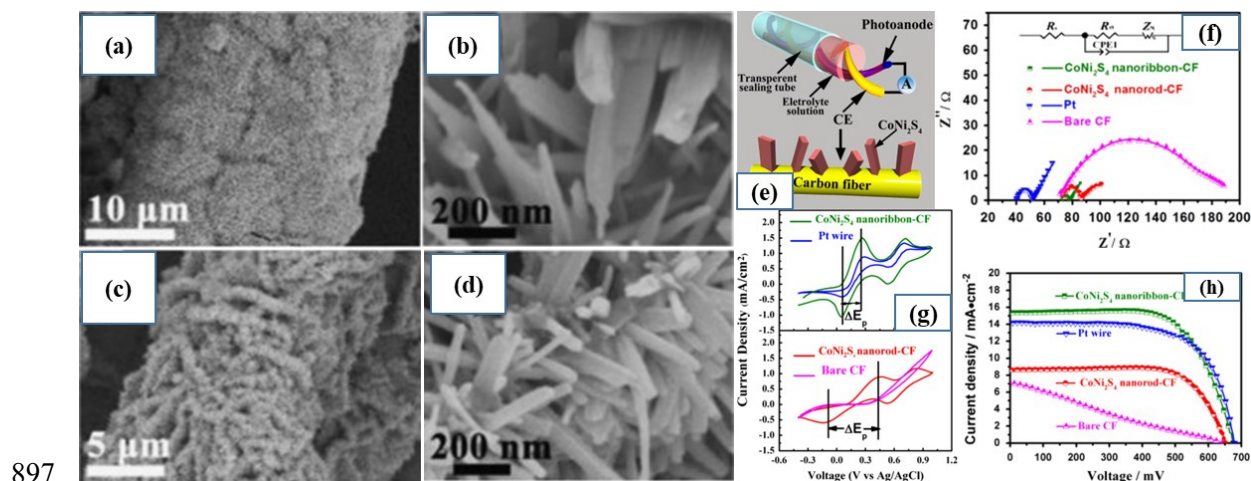
870

871 **Fig. 20** (a) Scanning electron microscopy (SEM) and (b) transmission electron microscopy
 872 (TEM) images of cobalt- and nitrogen-doped carbon nanofiber (Co-CNF) composite. (c) SEM
 873 and (d) TEM images of Co-N-CNF composite (inset: high-resolution lattice pattern of Co). (e)
 874 X-ray diffraction (XRD) patterns of the Co-CNFs and Co-N-CNFs. (f) Electrochemical
 875 impedance spectroscopy (EIS) Nyquist plots of the symmetrical cells. (g) CV and (h) J-V
 876 curves of dye-sensitized solar cells (DSSCs) fabricated with different counter electrodes (CEs).
 877 Copyright 2019, Elsevier; reprinted with permission.³⁶⁶ (i, j) Field emission (FE)-SEM images
 878 of MoS₂/CNFs with flower-like morphologies, (k, l) High resolution (HR)-TEM images of
 879 MoS₂/CNFs composites. (m) Nyquist and (n) Tafel plots of symmetrical cells, (o) CV of
 880 different CEs, and (p) J-V curve of the DSSCs using the obtained CEs. Copyright 2018,
 881 Elsevier; reprinted with permission.³⁶⁹

882

883 The mechanical strength of CNFs is similar—but slightly lower—compared to CNTs. This
 884 lower mechanical strength is due to the irregular organization of the graphene layers. The
 885 strength of CNFs can reach 12 GPa (and even up to 30 GPa); therefore, CNFs have also been
 886 explored to fabricate flexible and fiber-shaped DSSCs.^{362,370–372} Zou prepared
 887 CoNi₂S₄ nanoribbon and nanorod on carbon fibers and used them as CEs in fiber-shaped dye-
 888 sensitized solar cells (FDSSCs) (**Fig. 21**).³⁶⁸ CoNi₂S₄ nanoribbon-CF-based FDSSC show a
 889 high PCE of 7.03%, which is superior to the Pt wire CE (6.45%). Notably, the
 890 CoNi₂S₄ nanorod-CF-based DSSC show a PCE of 4.10%. The higher conversion efficiency of
 891 CoNi₂S₄ nanoribbon-CF-based FDSSC compared to nanorod-CF-based FDSSC is due to their
 892 intrinsic properties as well as their different morphological structure. The unique open crystal
 893 facet likely contributes to the noteworthy difference in PCE when compared to two 1D
 894 CoNi₂S₄ nanostructures. The detailed information of graphene CEs and their electrocatalytic
 895 and photovoltaic properties in DSSCs are summarized in **Table 7**.

896



898 **Fig. 21** Field emission scanning electron microscopy (FE-SEM) images of (a, b) CoNi₂S₄
 899 nanoribbon and (c, d) for CoNi₂S₄ nanorod at different magnifications. (e) Schematic structure
 900 of the fiber-shaped dye-sensitized solar cell (FDSSC). (f) Nyquist plots of the symmetric cells.

901 (e) CV curves and (h) J-V curves of FDSSCs based on different counter electrodes. Copyright
902 2015, Elsevier; reprinted with permission.³⁶⁹

903 **Table 7** Carbon nanofiber (CNF) counter electrodes (CEs) and their electrocatalytic and photovoltaic properties in dye-sensitized solar cells.

CE materials	Precursor/SSA (m ² g ⁻¹)	Substrate/coating technology	Redox couple	Sensitizer	R_s/R_{ct} (Ω cm ²)	$J_{sc}/V_{oc}/FF$ (mA cm ⁻² /V/%)	η^{CE}/η^{Pt} (%)	Ref	Year
CNF	Acetylene/156	FTO-g/doctor blading	I ₃ ⁻ /I ⁻	N3	-/1.1	15.51/0.70/62.0	6.74/7.25	373	2016
PCNF	Lignin & PVA/941	FTO-g/spray coating	I ₃ ⁻ /I ⁻	N719	-/-	15.94/0.65/73.0	7.60/7.67	359	2018
PCNF	hydro-pitch (HP) & PAN/560	FTO-g/doctor blading	I ₃ ⁻ /I ⁻	N719	-/-	14.16/0.76/65.0	6.92/6.34	360	2018
G-CNF/Pt	PAN/-	FTO-g/spin coating	I ₃ ⁻ /I ⁻	N719	3.16/0.12	18.57/0.78/67.0	9.70/8.63	242	2015
Pt/CNF	Commercial/-	FTO-g/spray coating	Co ³⁺ /Co ²⁺	YD2-o-C8	11.65/1.60	15.52/0.85/68.0	8.97/9.41	365	2015
Pt/CNF	Commercial/-	FTO-g/spray coating	I ₃ ⁻ /I ⁻	N719	11.79/1.56	14.44/0.79/65.0	7.40/7.88	365	2015
CoNi ₂ S ₄ -CNF	Commercial/8.61	Directly	I ₃ ⁻ /I ⁻	N719	36.3/2.55	15.3/0.68/67.7	7.03/6.45	368	2015
CNF/Pt	PAN/-	FTO-g/spray coating	I ₃ ⁻ /I ⁻	N719	1.03/0.52	13.33/0.83/68.8	7.6/7.4	367	2015
Co ₃ S ₄ /CNF	PAN/26.07	FTO-g/spray coating	Co ³⁺ /Co ²⁺	YD2-o-C8	10.05/1.2	16.57/0.77/72.0	9.23/8.38	374	2016
Pt/CNF	PVA/-	FTO-g/doctor blading	I ₃ ⁻ /I ⁻	N719	3.76/1.20	13.15/0.80/66.0	6.94/7.29	375	2016
Mo-Pt ₃ Ni/CNF	PAN/-	FTO-g/spray coating	I ₃ ⁻ /I ⁻	N719	-/-	16.94/0.774/72.3	9.47/7.1	376	2016
p-GN@CuInS ₂ /CNF	PAN/ 814	FTO-g/doctor blading	I ₃ ⁻ /I ⁻	N719	9.71/0.81 [†]	17.53/0.69/59.81	7.23/6.34	377	2016
Cr-Pt ₃ Ni/CNF	PAN/-	FTO-g/spray coating	I ₃ ⁻ /I ⁻	N719	7.65/1.22	17.53/0.69/59.81	7.23/ 6.34	377	2016
G/CNF-Ni	PAN/-	FTO-g/spray coating	I ₃ ⁻ /I ⁻	N719	4.23/0.72	14.31/0.84/ 60.0	7.14/ 7.59	377	2016
MnO ₂ /CNF	PAN/-	FTO-g/spray coating	I ₃ ⁻ /I ⁻	N719	4.53/1.62	16.15/0.78/70.0	8.86/ 8.27	378	2017
Co ₉ S ₈ /CNF	PAN/-	FTO-g/doctor blading	I ₃ ⁻ /I ⁻	N719	-/-	23.91/0.68/51.8	8.37/8.50	379	2018
MoS ₂ /CNF	PAN/-	FTO-g/spray coating	I ₃ ⁻ /I ⁻	N719	5.85/2.50	15.64/0.77/70.2	8.46/7.65	380	2018
MoO ₂ /CNF	PAN/-	FTO-g/spray coating	I ₃ ⁻ /I ⁻	N719	8.4/0.65 [†]	21.12/0.722/50.0	7.60/7.34	380	2018
Re-Pt ₃ Ni/CNF	PAN/-	FTO-g/spray coating	I ₃ ⁻ /I ⁻	N719	16.81/0.77 [†]	16.81/0.77/0.72	9.36/7.33	381	2018

Fe ₂ O ₃ /CNF	PAN/290.7	FTO-g/spray coating	I ₃ ⁻ /I ⁻	N719	4.61/0.42	16.61/0.72/62.0	7.41/6.94	³⁸²	2019
Ni ₃ S ₄ @C/CNF	PAN, Glucose & Urea/75.4	FTO-g/spray coating	I ₃ ⁻ /I ⁻	N719	6.00/1.65	15.41/0.77/70.0	8.29/7.35	³⁸³	2019
Pt-Ni ₂ P-CNF	PAN/-	FTO-g/spray coating	I ₃ ⁻ /I ⁻	N719	7.65/1.09	16.30/ 0.78/72.0	9.11/7.84	³⁸⁴	2019
Co/N-CNF	PAN, PVP & Urea/-	FTO-g/spray coating	I ₃ ⁻ /I ⁻	N719	5.65/0.64	18.02/0.74/68.0	9.05/7.10	³⁶⁶	2019

904 Abbreviations: FTO-g, fluorine-doped titanium oxide glass; PAN, polyacrylonitrile; SSA, specific surface area. †Charge transfer unit is Ω cm

3. Perovskite Solar Cells (PSCs)

3.1. Working principle of Perovskite Solar Cells

Perovskite materials present excellent light absorption; they are derived from calcium titanate (CaTiO_3). The perovskite material can be described by the formula AMX_3 , where A is an organic or inorganic cation (MA= methylammonium, FA = formamidinium, and Cs = cesium), M is a metal cation (such as lead [Pb], tin [Sn], or mixtures thereof)—with smaller size than that of the A cation—and X is generally a halogen anion (such as Cl, bromine [Br], iodine [I], or mixtures thereof). The perovskite crystal structure is depicted in **Fig. 22**. PSCs have experienced rapid development: the PCE has increased from 3.8 to 25.2% within 11 years³⁸⁵, mainly due to the following advantageous features: 1) perovskites exhibit broad spectral absorption^{386,387} from visible to near-infrared; and 2) perovskite materials possess a high absorption coefficient,^{388,389} high charge carrier mobilities,³⁹⁰ long carrier diffusion lengths,^{391,392} and small exciton binding energy.³⁹³

The general operating principles of PSCs are illustrated in **Fig. 22**. When incident light is irradiated to the perovskite layer through a transparent substrate (indium tin oxide [ITO] or FTO glass), photons with an energy greater than the forbidden band width of the perovskite can excite the electrons from the valence band to the conduction band, generating electron-hole pairs in the perovskite film. Then, the hole and electron are separated and transferred from the perovskite to the hole transporting materials (HTMs) and electron transporting materials (ETMs) simultaneously (**Fig. 22c**). The injected electrons diffuse through the ETM and reach the BE to complete the circuit, where they combine with diffuse holes at the BE. Furthermore, undesired reactions, such as exciton annihilation, non-radiative recombination and the recombination of holes and electrons at

the three interfaces (ETM/perovskite, perovskite/HTM and ETM/HTM), reduce the efficiency of the device.

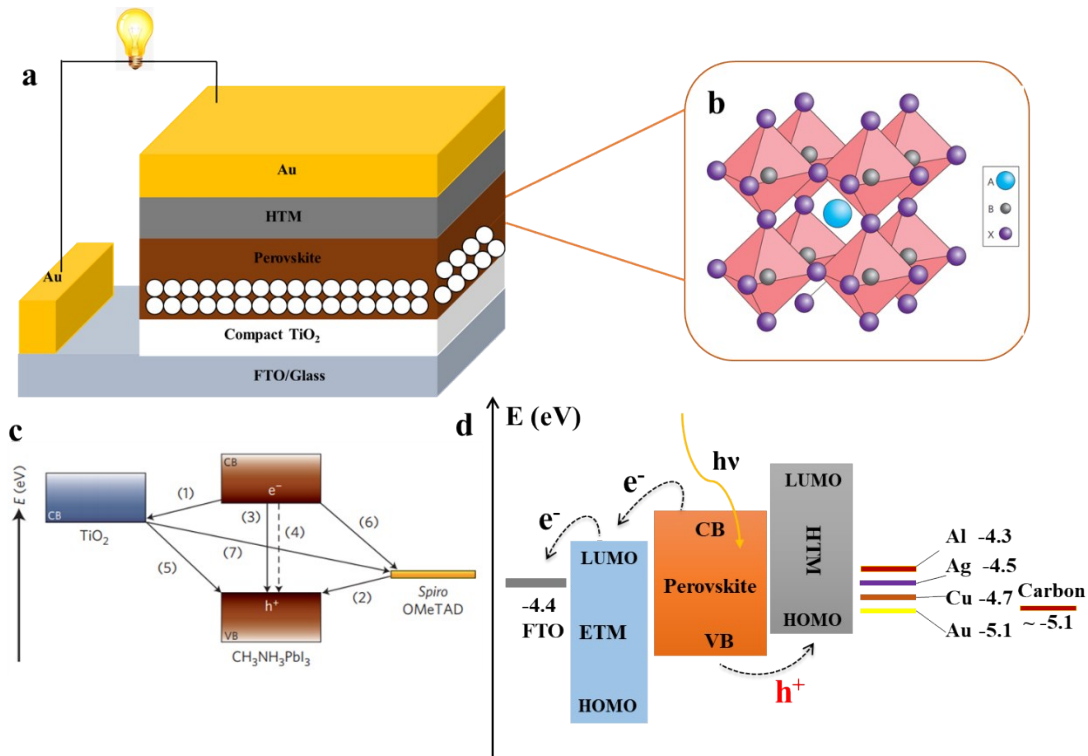


Fig. 22 a) A schematic of perovskite solar cell (PSC) architecture. b) The crystal structure of perovskite film. c) A schematic diagram of the energy levels and electron transfer processes in a HTM/perovskite/TiO₂ cell. d) An energy level diagram of related materials in PSCs that vary in the back electrode.

3.2 Back electrodes (BEs) for PSCs

The BE in a PSC plays a vital role in hole extraction and collection process from the valence band (VB) of perovskite layer or the HOMO of the HTM to the BE. In contrast to a CE in a DSSC, a BEs in a PSC does not require electrocatalytic activity. However, a BE requires a suitable WF for better energy level alignment and hole collection from the

perovskite layer or the HOMO of the HTM. Furthermore, a BE's electric conductivity and film morphology should also be seriously considered to reduce the series resistance and make a good physical contact in the interface of perovskite/BE layers, which are crucial for the photovoltaic performance of device. Currently, the most widely used BEs in state-of-the-art PSCs are noble metals, such as Au and Ag. These metals possess a low sheet resistance (R_{sq}) as well as high light reflectivity. However, Ag reacts with the iodide ions in the perovskite layer to generate AgX, which degrades perovskite film.^{394–396} On the other hand, Au BEs usually faces metal migration through the HTM into perovskite films. This phenomenon leads to the dramatic performance degradation of the devices.^{397–399} These Au and Ag drawbacks will hamper the scalable commercialization and long-term stability of PSCs.

Al has a low WF of 4.3 eV and is typically used as a BE in inverted PSCs. However, Al exhibits high constraints as a PSC electrode due to its high reduced power originating from its comparatively low standard reduction potential of -1.66 V. Zhao *et al.* employed *in situ* X-ray diffraction (XRD) to show that Al⁰ can reduce Pb⁺ to Pb⁰ in H₂O and dimethylformamide (DMF) even without the requirement of oxygen or light, and thus convert TiO₂/Al₂O₃/carbon (MAPbI₃) to (CH₃NH₃)₄PbI₆·2H₂O and later methylammonium iodide (MAI).⁴⁰⁰ In addition, some alternative non-metal BEs have already been developed for PSCs, including carbon and the polymer poly(3,4-ethylenedioxythiophene) polystyrene sulfonate (PEDOT:PSS). To replace the expensive metal electrode, various carbon BEs have been developed as alternatives; they present excellent function due to their hydrophobic features, suitable electronic properties, and excellent chemical and thermal stability.⁴⁰¹ In the following section, we comprehensively

illustrate and emphasize the development of various carbons as alternative BEs to metal electrodes (Ag, Al, and Au). We present the characteristics of different carbon BEs, their fabrication methods, and the performance of devices with carbon-based BEs. We hope that this review will give researchers more insights into non-metal carbon BEs for PSCs and their contribution to boost future PSC commercialization.

3.3. Carbon BEs for PSCs

Carbon materials are abundant, low cost, and have high electrical conductivity, chemical stability, diversity, and modifiability.⁴⁰² They usually have a WF of 5.0 eV, which is close to that of Au (5.1 eV). Hence, they can be potential BEs for PSC. Carbon pastes (usually a composite of graphite and CB), CNTs, or graphene have been used in carbon-based PSCs.⁴⁰³

3.3.1. Carbon pastes for PSCs

Carbon pastes composed of graphite and CB are the earliest and most popular carbon materials used in PSC devices. So far, there are two main device configurations for the carbon pastes as PSC BE applications (**Fig. 23**). One architectural design consists of a mesoporous triple layer with an insulator space layer, also known as meso-PSC (**Fig. 23a**). In this device, before the deposition of the perovskite layer, an ETM of mesoporous TiO₂, an insulator spacer layer (ZrO₂ or Al₂O₃), and a mesoporous carbon BE layer are sequentially deposited. The obtained scaffold is then processed at a high temperature to improve the adhesion and physical contact of the assembled layers. Finally, the perovskite film is formed via the infiltration of perovskite precursor solution through the mesoporous triple layer of TiO₂/ZrO₂/carbon. The insulating ZrO₂ layer prohibits direct contact of carbon with the TiO₂ layer. In this architecture, various parameters may affect perovskite

precursor infiltration, such as the size of graphite, CB, the thickness, and even the morphology of carbon film, as well as the related parameters of insulating spacer layer (ZrO_2). Hence, these parameters should be thoughtfully considered.

A conventional type PSC represents another design architecture (**Fig. 23b**); it excludes the insulating spacer layer. The carbon electrode is deposited onto top of the perovskite film; thus, the carbon film should be processed at low temperature to avoid the thermal degradation of the perovskite film. Additionally, the processing solvent for the carbon paste should not damage the under perovskite film. Therefore, the following aspects should be seriously considered when employing carbon paste for conventional PSCs; (i) processing temperature; (ii) processing solvent for carbon paste; (iii) deposition method; (iv) the WF of the carbon film, to enable efficient hole extraction and collection; and (v) the conductivity of carbon film.

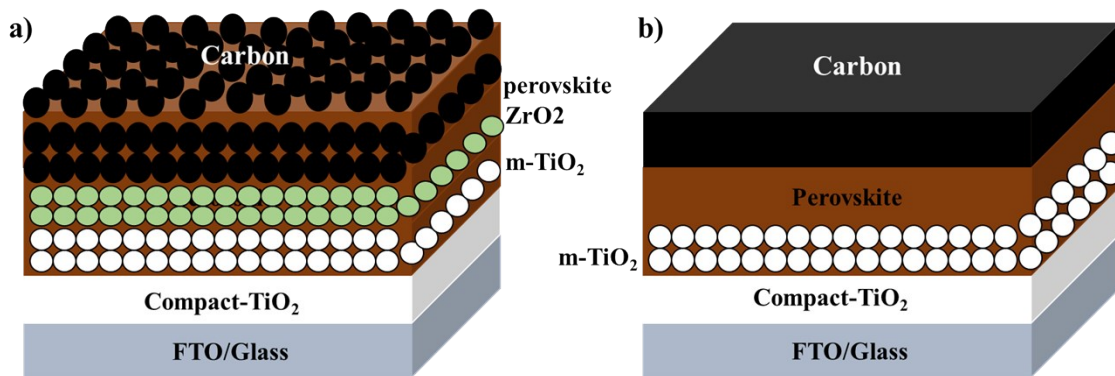


Fig. 23. A schematic structure of device configurations for a carbon back electrode (BE)–based perovskite solar cell (PSC). a) A triple mesoporous layer containing an insulator spacer layer (ZrO_2 or Al_2O_3). b) A conventional HTM-free carbon BE–based PSC.

3.3.1.1. Device configuration with mesoporous triple layers including an insulator space layer

For the mesoporous triple layer C-PSC device configuration, an insulating layer of ZrO_2 ,^{404,405} Al_2O_3 ,⁴⁰⁶ or SiO_2 ⁴⁰⁷ is required to be inserted between the TiO_2 and carbon layer. This insulating layer plays a vital role to prevent the ETM from making direct physical contact with the CB electrode. The carbon paste is finally deposited on the top of the FTO substrate/compact TiO_2 /mesoporous- TiO_2 / ZrO_2 or Al_2O_3 insulating layer. In addition, the TiO_2 /insulator layer (ZrO_2 or Al_2O_3)/ mesoporous carbon layer serve as the scaffold to support the deposition of perovskite light absorbing layer by the infiltration-drying-crystallization process.^{407–413}

Generally, carbon paste electrodes employ CB and graphite as the main components. They are usually applied in mesoporous triple layer with insulator layer type PSCs due to the mesoporous character. Graphite is the vital component with regard to determining the porosity and conductivity of a CB electrode. In 2014, Han *et al.* first investigated the effect of graphite size in the CB/graphite BE on the device performance of HTM-free mesoscopic PSCs.⁴¹⁴ They demonstrated that an 8 μm graphite carbon BE possessing a larger pore size is beneficial for the filling of perovskite precursors through the mesoporous carbon layer. Meanwhile, the conductivity characterization results indicated that 8 μm graphite carbon BE exhibits a smaller R_{sq} (square resistance) and, hence, a higher PCE up to 11.65%, with a FF value of 0.72, compared with other graphite size-based devices (**Fig. 24a–h**).

Increasing the conductivity of carbon BEs can help lower the series resistance of the device; this endeavor increases the FF value of a PSC. The introduction of functional

additives of acetic acid and titanium(IV) isopropoxide to carbon paste prior to the ball milling process increase the conductivity.⁴¹⁵ The electrical conductivity of this newly developed carbon film is up to $1.13 \times 10^4 \text{ Sm}^{-1}$ due to the *in situ* generation of newly complex polymeric Ti–O–Ti species that act as a binder and plasticizer. Thus, a PSC based on a carbon paste BE treated by acetic acid and titanium(IV) isopropoxide achieves a high efficiency of 14.04%.

Heteroatom doping of carbons has been widely used for CNTs⁴¹⁶ and graphene.^{417,418} Furthermore, the hole extraction ability and a WF of carbon BE are crucial for HTM-free carbon-based PSCs (C-PSCs).⁴¹⁹ Thus, doping the graphite with heteroatoms may be a feasible strategy for tuning the WF and conductivity of a graphite-based BE.^{420,421} One study doped graphite with B by a ball milling process of graphite powder with a 5% mass ratio of boron carbide (B_4C) followed carbonization at 900°C for 2 h prior to the graphitization. This process increases the WF and enhances conductivity due to higher graphitization.³⁹ Thus, the hole extraction from perovskite to the carbon electrode is facilitated, leading to much improved efficiency from 12.4% for the pristine graphite BE-based PSC to 13.6% for the boron-doped BE-based PSC due to an improved open-circuit voltage and FF. In another study, oxygen-rich carbon black (ORC), which has a high oxygen content, elevates the WF of a BE and improves the interface contact between carbon BE and perovskite layer.⁴²² When combined with the p-type characteristic of ORC, the hole extraction from perovskite to a ORC BE is considerably enhanced. Thus, an HTM-free C-PSC based on ORC BE exhibits a higher V_{OC} of 980 mV compared to an oxygen-deficient carbon black (ODC)-based device with a V_{OC} of 880mV (**Fig. 24i–k**).

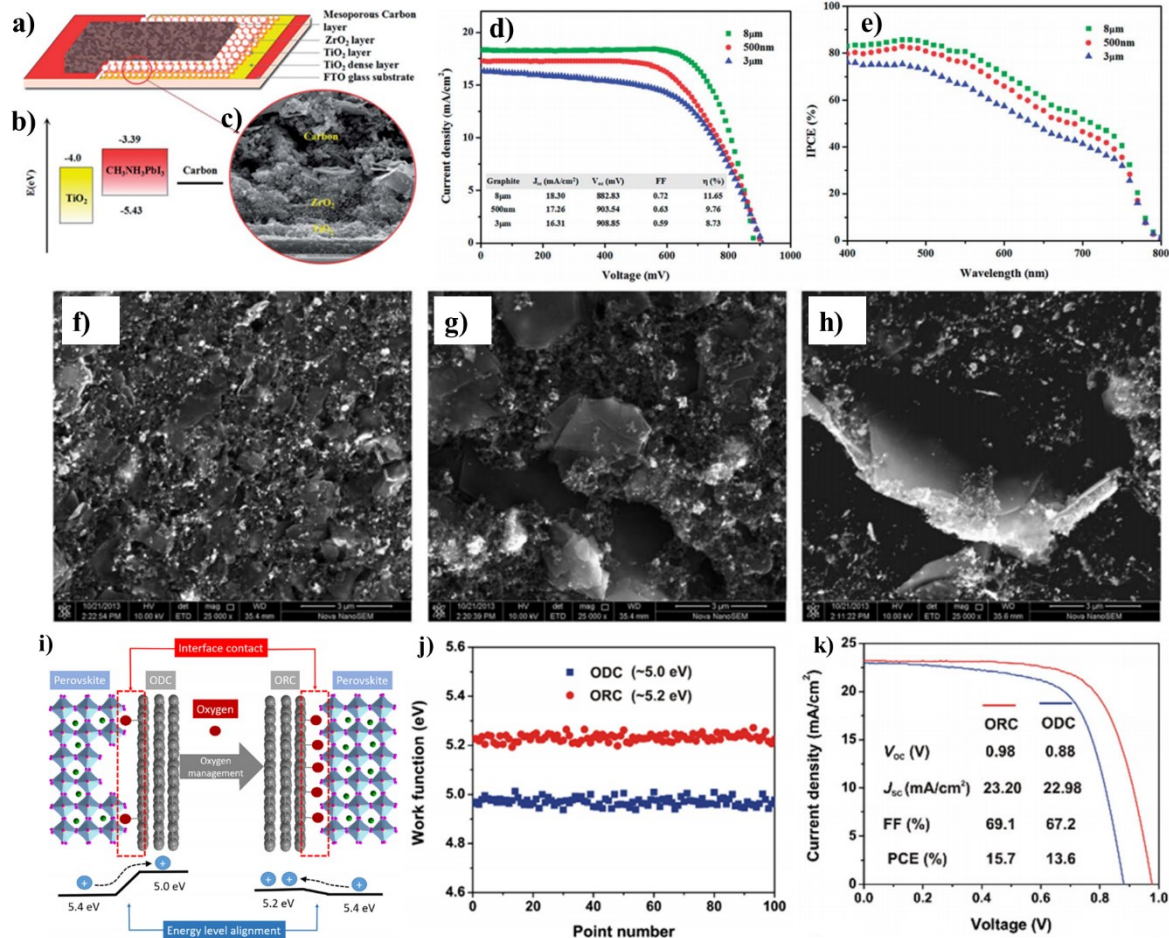


Fig. 24 a) The schematic structure of a carbon back electrode (BE)–based perovskite solar cell (PSC). b) The energy level diagram of related components in device. c) A cross-sectional scanning electron microscopy (SEM) image of a PSC. d) J–V curves of carbon BE–based PSC with different graphite sizes. e) The corresponding IPCE curves. f–h) Surface SEM images of carbon BE with different graphite particle sizes: 500 nm, 3 μm, and 8 μm, respectively. Copyright 2015, The Royal Society of Chemistry; reprinted with permission.⁴¹⁴ i) Schematic illustration of oxygen-deficient carbon black (ODC) and oxygen-rich carbon black (ORC) film, interfacial contact, and energy level alignment of perovskite/carbon. j) Work function curves of ODC and ORC film. k) J–V curves of C-

Based on the features of triple mesoporous layer device structure, the penetration of perovskite solution through carbon and ZrO₂ films to reach the ETM is crucial. The main role of the insulating spacer layer for C-PSCs is to separate the ETM and carbon BE, and thus prevent the electrons in the ETM from being transported to the carbon electrode. To improve the separating property of the insulating layer and ensure high performance in C-PSCs, many factors should be considered: the particle size of the insulating spacer layer, film morphology, a wide bandgap of the spacer layer, the thickness of the insulating layer and interfacial contact of the perovskite/ZrO₂ (or Al₂O₃).^{405,409,423,424} A device without a ZrO₂ spacer layer shows rather poor device performance, delivering a PCE of only 1.56% because the electrons in the TiO₂ may directly leak to the carbon BE. The efficiency improves markedly to 5.92% in the presence of 0.3 μm ZrO₂, and it further increases to 10.3% when inserting a 1 μm ZrO₂ film. However, a very thick ZrO₂ layer may limit the carrier diffusion length and decrease the device efficiency.^{391,392} Han *et al.*⁴²⁵ systematically investigated the spacer layer parameters of design points for the triple mesoporous layer structures of C-PSCs. They proposed that an efficient spacer layer for C-PSCs should possess the following features: a) pore size > 100 nm, b) high porosity, and c) excellent insulating property with an ultra-thin film thickness.

Zhou *et al.*⁴⁰⁷ investigated SiO₂ paste as a low cost insulating layer to replace ZrO₂. With this replacement, the PCE is 13.09%, which is comparable to a device with a ZrO₂ spacer layer. Furthermore, the PCE of devices without encapsulation decreases from the

initial value of 13.09% to the final value 12.33% after storage under ambient air conditions for 104 days (50–70% relative humidity). The authors mainly attributed this loss to the thick and condensed carbon films providing a heavy barrier against air ($\text{H}_2\text{O}/\text{O}_2$) as well as the chemical stability of SiO_2 paste.

Inserting a P-type layer (NiO ⁴¹⁰ or WO_3 ^{426,427}) between the insulating layer and carbon film is also an efficient way to improve photovoltaic performance because it reduces carrier recombination and benefits the hole extraction rate. In 2015, Wang *et al.* employed $\text{NiO}/\text{Al}_2\text{O}_3$ as a spacer layer to prevent the direct contact of TiO_2 and carbon BE in MAPbI_3 -based C-PSCs.⁴¹⁰ The presence of an NiO layer between Al_2O_3 and the carbon BE significantly improves the J_{sc} value from 17.59 mA cm^{-2} for the parent $\text{TiO}_2/\text{Al}_2\text{O}_3/\text{carbon}$ (MAPbI_3)-based device to 21.62 mA cm^{-2} for the $\text{TiO}_2/\text{Al}_2\text{O}_3/\text{NiO}/\text{carbon}$ (MAPbI_3)-based device (**Fig. 25a–c**). Moreover, the NiO -containing device provides a higher V_{oc} value of 915 mV, compared to 896 mV for the parent device without the NiO layer, due to the reduced charge carrier recombination. This outcome is attributed to the dual roles of the spacer layer as well as the HTM. The PCE of the device with the NiO layer is markedly higher (15.03%) compared to that of the device without NiO (11.2%). Considering the appropriate position of the WO_3 conduction band, Bhandari *et al.* incorporated p-type inorganic WO_3 nanoparticle into the carbon BE to promote hole extraction at the perovskite/carbon interface for C-PSCs.^{426,427} It was found that the device performance can be significantly influenced depending on the amount of incorporated WO_3 additive into the carbon BE. The optimal amount of WO_3 additive by volume (7.5%) gives the highest device PCE (10.3%), compared to 7.4% for the control device without WO_3 additive.

Compared to conventional HTM-based PSCs, recombination at the interfaces of ETM/perovskite and perovskite/BE, where the generated electrons recombine with holes, is a more serious issue in HTM-free C-PSCs due to the direct contact of carbon and TiO₂.^{428,429} Therefore, the V_{OC} value of C-PSCs are usually lower compared to conventional HTM-based PSCs. To avoid the recombination at the interfaces of ETM/perovskite and perovskite/BE is crucial to increase the V_{OC} value of C-PSCs. Surface modification of ETMs by insulating materials, such as MgO,⁴³⁰ Al₂O₃,^{431,432} or La₂O₃,⁴³³ suppresses the charge recombination and enhances the V_{OC} of devices in conventional PSCs. Similarly, the surface modification of the mesoporous TiO₂ by inserting an additional ultrathin Al₂O₃ layer with a ZrO₂ spacer layer increases the efficiency—due to minor charge recombination—and thus enhances the V_{OC} of the device (**Fig. 25d–f**).⁴³⁴ Furthermore, inserting a thin Al₂O₃ insulating layer is favored to reduce the expensive ZrO₂ spacer layer without a loss of efficiency.⁴³⁵

From the aspect of perovskite composition engineering, partially substituting the MA cation with a 5-AVA group,⁴¹¹ or replacing the anion of I⁻ with BF₄⁻,⁴³⁶ or introducing a triple cation to the perovskite film can help to deposit a high quality perovskite film with low defect concentrations and improve carrier transport. These factors lead to better device performance. The incorporation of 5-AVA to perovskite precursor decreases defect concentrations and improve pore filling via the formation of linear hydrogen-bonded chains between COOH and NH₃⁺ groups from 5-AVA and I⁻ ions from the PbI₆ octahedron. Thus, a (5-AVA)_x(MA)_{1-x}PbI₃-based PSC shows a significantly improved efficiency (up to 11.6%) compared to 7.2% for a MAPbI₃-based device. Besides, a (5-AVA)_x(MA)_{1-x}PbI₃-based device exhibits long-term stability (> 1000 h) under full sunlight in ambient air (**Fig.**

25g–i). Based on the same device configuration, partially substituting I of perovskite with BF_4^- markedly improves efficiency from 10.54% to 13.24% due to enhanced charge transport and reduced charge recombination (**Fig. 25j–l**).⁴³⁶ Using triple cation perovskite $\text{Cs}_{0.05}(\text{FA}_{0.4}\text{MA}_{0.6})_{0.95}\text{PbI}_{2.8}\text{Br}_{0.2}$ as a light absorber material—instead of MAPbI_3 —demonstrated that the presence of Cs in perovskite layer can extend the carrier diffusion length (electron diffusion lengths of 140 nm and hole diffusion lengths of 1.9 μm). These alterations benefit charge transport in mesoporous layers.⁴³⁷ Therefore, PSCs based on $\text{Cs}_{0.05}(\text{FA}_{0.4}\text{MA}_{0.6})_{0.95}\text{PbI}_{2.8}\text{Br}_{0.2}$ show a PCE of 17.02%, with a J_{SC} of 23.4 mA/cm^2 , a V_{OC} of 1.008 V, and a FF of 0.72. Meanwhile, a devices based on the Cs doped triple cation exhibited excellent stability, with a retention of > 90% initial PCE after stored in dark conditions at 85°C for 1020 h.

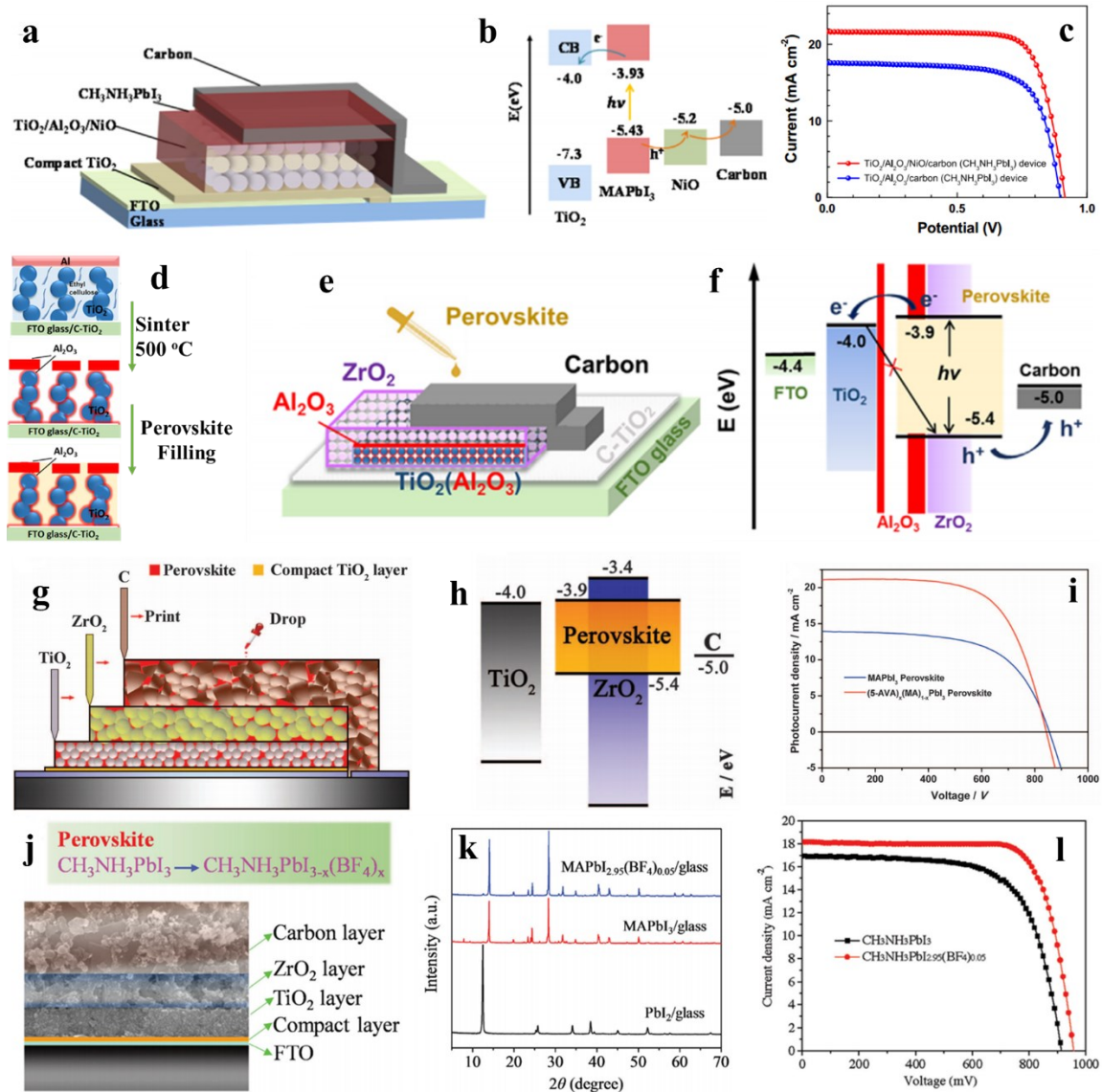


Fig. 25 (a) Configuration of a fluorine-doped tin oxide (FTO)/c-TiO₂/m-TiO₂/Al₂O₃/NiO/carbon (MAPbI₃) device. (b) An energy level diagram of the corresponding carbon-based perovskite solar cell (C-PSC). (c) J-V curves for champion devices of TiO₂/Al₂O₃/NiO/carbon (MAPbI₃) configuration and regular TiO₂/Al₂O₃/carbon (MAPbI₃) (blue squares). Copyright 2015, Elsevier; reprinted with permission.⁴¹⁰. (d) Formation process of a bifunctional Al₂O₃ interlayer. (e) Device structure of hole-conductor-free C-PSCs with an Al₂O₃ interlayer and (f) the corresponding

energy band diagram. Copyright 2018, WILEY-VCH; reprinted with permission.⁴³⁴ (g) Schematic configuration of an FTO/c-TiO₂/m-TiO₂/ZrO₂/C/perovskite mesoscopic solar cell prepared by printing process. (h) Energy level diagram of the related materials. (i) J-V curves of (5-AVA)_x(MA)_{1-x}PbI₃ (red curve) and MAPbI₃-based PSCs measured under one sun simulation. Reprinted with permission.⁴¹¹ Copyright 2014, American Association for the Advancement of Science. (j) Structure of a mesoporous C-PSC device. (k) X-ray diffraction (XRD) spectra of PbI₂/glass, MAPbI₃/glass, and MAPbI_{2.95}(BF₄)_{0.05}/glass devices. (l) J-V curve of C-PSCs based on different perovskite composition. Copyright 2016, WILEY-VCH; reprinted with permission.⁴³⁶

Zhang *et al.*⁴³⁸ pre-passivated the triple mesoporous layer of TiO₂/ZrO₂/C by dipping the mesoporous triple layer scaffold into a 0.2 mM PbI₂ solution in DMF for 30 min at room temperature. They then rinsed the triple layer scaffold in DMF to get rid of loosely bound PbI₂. X-ray photoelectron spectroscopy (XPS) characterization showed the formation of C–O–Pb linkages via the reaction of –OH on the carbon surface with PbI₂. The PCE of the pre-passivated device significantly improves to 7.3% compared to the device without pretreatment of PbI₂ by one-step method for perovskite deposition (2.21%). This increased efficiency is due to the reduced carrier recombination.

Investigation on the precursor solvent showed that an optimized DMF/dimethyl sulfoxide (DMSO) ratio (0.93:0.07, v/v) provides better wettability and excellent perovskite film quality because of a suitable compromise between the solvent's polarity and viscosity.⁴³⁹ The device based on this optimal solvent has a PCE of 13.89% due to the improved light harvesting ability and the enhanced charge separation of the perovskite

(**Fig. 26a–c**). Additives, like guanidinium chloride (GuCl), improve the quality of the $\text{CH}_3\text{NH}_3\text{PbI}_3$ perovskite absorber and suppress recombination in the device (**Fig. 26d**).⁴⁴⁰ The suppressed recombination at the TiO_2 /perovskite interface is considered due to the exchange hydrogen-bonding interaction between $-\text{C}(\text{NH}_2)_3^+$ and halide ions (from $\text{N}-\text{H}\cdots\text{Cl}^-$ to $\text{N}-\text{H}\cdots\text{I}^-$). The three $-\text{NH}_2$ groups in GuCl may increase the linking of the neighboring MAPbI_3 , thus helping the crystal growth in contact with each other more tightly (**Fig. 26e–j**). A device with pristine MAPbI_3 shows a PCE of 9.10% with a V_{OC} of 0.88 V, a J_{SC} of 15.10 mA cm^{-2} , a FF of 0.68. The device fabricated with $\text{MAPbI}_3 \cdot x\text{GuCl}$ presents a much higher PCE of 14.35% and V_{OC} of 1.00 V, and an enhanced J_{SC} of 19.31 mA cm^{-2} and a FF of 0.743.

The perovskite layer is sensitive and unstable when exposed to water and moisture, ultraviolet light, and thermal stress.^{441–443} Beyond PSC degradation due to the poor perovskite layer stability, device instability can be also accelerated by the instability of the other layers in the full device. For example, the dopants used in organic HTM layer are hydrophilic and, consequently, reduce device stability.^{444,445} Thus, it is crucial to improve the stability of the perovskite layer, HTM, and BE to ensure the full device is stable. Rong *et al.* carried out moisture-induced transformation of perovskite crystals in a triple-layer scaffold of $\text{TiO}_2/\text{ZrO}_2/\text{carbon}$ to fabricate printable mesoscopic solar cells. The employed ammonium chloride (NH_4Cl) as an additive to assist the perovskite crystallization, wherein the formation and transition of intermediate $\text{CH}_3\text{NH}_3\text{X} \cdot \text{NH}_4\text{PbX}_3(\text{H}_2\text{O})_2$ ($\text{X}=\text{I}$ or Cl) enables high-quality perovskite $\text{CH}_3\text{NH}_3\text{PbI}_3$ crystals with a preferential growth orientation (**Fig. 26k, l**). A device based on $\text{CH}_3\text{NH}_3\text{PbI}_3$ achieves an average PCE of 13.92%, with a champion efficiency of 15.60% and a lifetime of over 130 days in ambient

air with 35% relative humidity. This design and strategy suggest promising prospects for further mass production of perovskite-based photovoltaics and will significantly promote the development of perovskite-based photovoltaics.⁴⁴⁶

In 2017, Nazeeruddin *et al.* prepared triple mesoporous layer structure carbon electrode-based PSCs that are stable for 1 year by the combination of incorporation of moisture stable 2D perovskite layer and HTM-free carbon-based BE (**Fig. 26m, n**).³¹ This ultra-stability is due to the use of mixed perovskites—2D perovskite (5-AVA)₂PbI₄ and 3D perovskite CH₃NH₃PbI₃—which form a 2D/3D interface in the devices. The 10 × 10 cm² PSC solar modules prepared via a fully printable industrial-scale process show 11.2% efficiency and the device stability for > 10,000 h with zero loss in efficiency measured under controlled standard conditions. **Table 8** shows the summary information of carbon-based perovskite solar cells with device structure of TiO₂/insulating spacer layer/carbon past/perovskite.

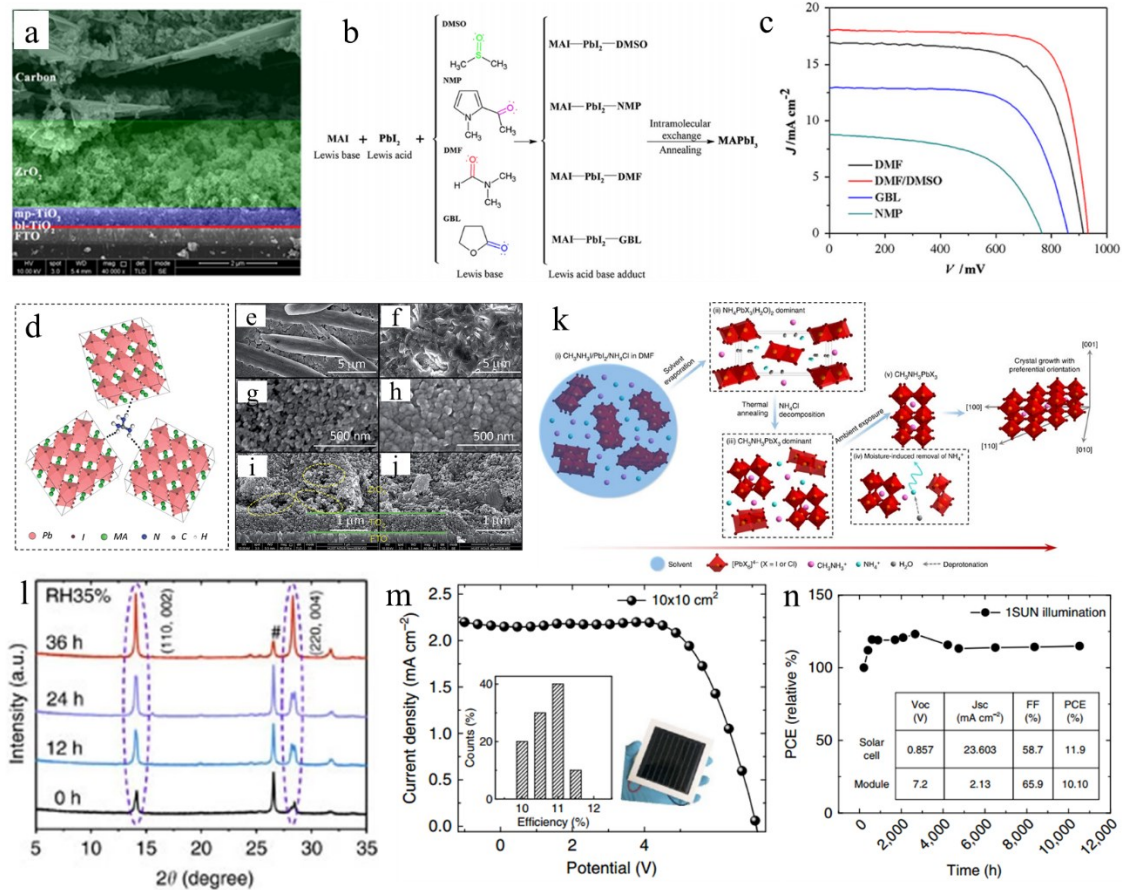


Fig. 26 (a) A cross-sectional scanning electron microscopy (SEM) image of a practical carbon-based perovskite solar cell (C-PSC). (b) The formation process of an intermediate phase and MAPbI₃ film from dimethyl sulfoxide (DMSO), dimethylformamide (DMF), gamma butyrolactone (GBL), and *N*-Methyl-2-pyrrolidone (NMP) as the solvent for the perovskite precursor. (c) J-V curves of C-PSCs based on various solvents. Copyright 2016, Elsevier; reprinted with permission.⁴³⁹ (d) Schematic illustration of three neighboring grain structures cross-linked by hydrogen-bonding interactions (N–H···I) of the iodide with the ammonium end groups of guanidinium chloride (GuCl) species. (e and f) Surface SEM images of MAPbI₃ and MAPbI₃·*x*GuCl films on fluorine-doped tin oxide (FTO) substrates. (g and h) Surface SEM images of MAPbI₃ and MAPbI₃·*x*GuCl (*x* = 0.25) infiltrated

mesoporous TiO₂ films. (i and j) Cross sectional SEM images of the mesoporous scaffold (TiO₂/ZrO₂) infiltrated with MAPbI₃ and MAPbI₃·xGuCl ($x = 0.25$). Copyright 2017, The Royal Society of Chemistry; reprinted with permission.⁴⁴⁰ (k) Schematic view of the crystal growth process of perovskite CH₃NH₃PbX₃ in the presence of ammonium and moisture. (l) X-ray diffraction patterns of intermediate infiltrated in TiO₂/ZrO₂/carbon triple layer during ambient exposure (RH35% for 36 h). Copyright 2017, Nature Publishing Group; reprinted with permission.⁴⁴⁶ (m) J-V curve using two-dimensional (2D)/three-dimensional (3D) perovskite with 3% AVAI in a hole transporting material (HTM)-free 10 × 10 cm² module. (n) Typical module stability test under one sun AM 1.5 G conditions at a stabilized temperature of 55°C and short circuit conditions. Copyright 2017, Nature Publishing Group; reprinted with permission.³¹

Table 8 Summary of photovoltaic parameters for carbon-based perovskite solar cells with device structure of TiO₂/insulating spacer layer/carbon past/perovskite.

Device configuration	Deposition method	Thermal Treatment	V_{oc} (mV)	J_{sc} (mA cm ⁻²)	FF	η (%)	Ref.
FTO/c-TiO ₂ /m-TiO ₂ /0- μ m ZrO ₂ /Carbon/MAPbI ₃	Screen-printing	400°C/30 min	0.59	7.03	0.37	1.56	405
FTO/c-TiO ₂ /m-TiO ₂ /0.3- μ m ZrO ₂ /Carbon/MAPbI ₃	Screen-printing	400°C/30 min	0.79	11.52	0.64	5.92	405
FTO/c-TiO ₂ /m-TiO ₂ /0.5- μ m ZrO ₂ /Carbon/MAPbI ₃	Screen-printing	400°C/30 min	0.85	15.74	0.67	9.02	405
FTO/c-TiO ₂ /m-TiO ₂ /1- μ m ZrO ₂ /Carbon/MAPbI ₃	Screen-printing	400°C/30 min	0.9	17.42	0.66	10.30	405
FTO/c-TiO ₂ /m-TiO ₂ /1.4- μ m ZrO ₂ /Carbon/MAPbI ₃	Screen-printing	400°C/30 min	0.85	19.60	0.55	9.29	405
FTO/c-TiO ₂ /m-TiO ₂ /m-Al ₂ O ₃ /0-nm NiO/Carbon/MAPbI ₃	blade-coating	400°C/30 min	815	16.11	0.66	8.67	410
FTO/c-TiO ₂ /m-TiO ₂ /m-Al ₂ O ₃ /400-nm NiO/Carbon/MAPbI ₃	blade-coating	400°C/30 min	902	18.19	0.71	11.65	410
FTO/c-TiO ₂ /m-TiO ₂ /m-Al ₂ O ₃ /600-nm NiO/Carbon/MAPbI ₃	blade-coating	400°C/30 min	904	18.99	0.70	12.01	410
FTO/c-TiO ₂ /m-TiO ₂ /m-Al ₂ O ₃ /800-nm NiO/Carbon/MAPbI ₃	blade-coating	400°C/30 min	923	20.14	0.72	13.39	410
FTO/c-TiO ₂ /m-TiO ₂ /m-Al ₂ O ₃ /1200-nm NiO/Carbon/MAPbI ₃	blade-coating	400°C/30 min	915	19.35	0.71	12.57	410
FTO/c-TiO ₂ /m-TiO ₂ /ZrO ₂ /Carbon/No PbI ₂ pretreatment/MAPbI ₃ (one-step)	Screen-printing	100°C/15 min	740	4.91	0.60	2.21	438

FTO/c-TiO ₂ /m-TiO ₂ /ZrO ₂ /Carbon/PbI ₂ pretreatment/MAPbI ₃ (one-step)	Screen-printing	100°C/15 min	900	13.38	0.54	6.55	438
FTO/c-TiO ₂ /m-TiO ₂ /ZrO ₂ /Carbon/No PbI ₂ pretreatment/MAPbI ₃ (two-step)	Screen-printing	100°C/15 min	910	14.51	0.54	7.08	438
FTO/c-TiO ₂ /m-TiO ₂ /ZrO ₂ /Carbon/PbI ₂ pretreatment/MAPbI ₃ (two-step)	Screen-printing	100°C/15 min	930	15.32	0.51	7.30	438
FTO/c-TiO ₂ /m-TiO ₂ /m-Al ₂ O ₃ /Carbon (0% WO ₃ additive) /MAPbI ₃	Screen-printing	450°C/30 min	788.8	15.16	0.62	7.40	426
FTO/c-TiO ₂ /m-TiO ₂ /m-Al ₂ O ₃ /Carbon (containing 5% WO ₃ additive) /MAPbI ₃	Screen-printing	450°C/30 min	801.3	16.4	0.60 5	7.95	426
FTO/c-TiO ₂ /m-TiO ₂ /m-Al ₂ O ₃ /Carbon (containing 7.5% WO ₃ additive) /MAPbI ₃	Screen-printing	450°C/30 min	842.3	21.1	0.58	10.30	426
FTO/c-TiO ₂ /m-TiO ₂ /m-Al ₂ O ₃ /Carbon (containing 10% WO ₃ additive)/MAPbI ₃	Screen-printing	450°C/30 min	840.4	19.3	0.56	9.15	426
FTO/c-TiO ₂ /m-TiO ₂ /ZrO ₂ /Carbon black & 500 nm size of graphite /MAPbI ₃ (two-step)	Screen-printing	400°C/30 min	903.5	17.26	0.63	9.76	414
FTO/c-TiO ₂ /m-TiO ₂ /ZrO ₂ /Carbon black & 3 μm size of graphite/MAPbI ₃ (two-step)	Screen-printing	400°C/30 min	908.9	16.31	0.59	8.73	414
FTO/c-TiO ₂ /m-TiO ₂ /ZrO ₂ /Carbon black & 8 μm size of graphite /MAPbI ₃ (two-step)	Screen-printing	400°C/30 min	882.8	18.30	0.72	11.65	414
FTO/c-TiO ₂ /m-TiO ₂ /ZrO ₂ /Carbon/(5-AVA) _x MA _{1-x} PbI ₃ with formamide additive in precursor	Screen-printing	400°C/40 min	930	23.7	0.69	15.21	447
FTO/c-TiO ₂ /m-TiO ₂ /ZrO ₂ /Carbon/(5-AVA) _x MA _{1-x} PbI ₃ with acetamide additive in precursor	Screen-printing	400°C/40 min	930	23.69	0.71	15.51	447
FTO/c-TiO ₂ /m-TiO ₂ /ZrO ₂ /Carbon/(5-AVA) _x MA _{1-x} PbI ₃ with urea additive in precursor	Screen-printing	400°C/40 min	920	23.63	0.69	15.07	447
FTO/c-TiO ₂ /m-TiO ₂ /ZrO ₂ /Carbon/(5-AVA) _x MA _{1-x} PbI ₃ (control)	Screen-printing	400°C/40 min	900	23.53	0.67	14.26	447
FTO/c-TiO ₂ /m-TiO ₂ /ZrO ₂ /Carbon/MAPbI ₃	Screen-printing	400°C/30 min	855	13.9	0.61	7.2	448

FTO/c-TiO ₂ /m-TiO ₂ /ZrO ₂ /Carbon/ (5-AVA) _x MA _{1-x} PbI ₃	Screen-printing	400°C/30 min	843	21.1	0.65	11.6	448
FTO/c-TiO ₂ /m-TiO ₂ /ZrO ₂ /Carbon/MAPbI ₃	Screen-printing	400°C/30 min	914	16.92	0.68	10.54	436
FTO/c-TiO ₂ /m-TiO ₂ /ZrO ₂ /Carbon/MAPbI _{2.95} (BF ₄) _{0.05}	Screen-printing	400°C/30 min	957	18.15	0.76	13.24	436
FTO/c-TiO ₂ /m-TiO ₂ /ZrO ₂ /Carbon/MAPbI ₃ /precursor solvent:DMF	Screen-printing	400°C/30 min	914	16.92	0.68	10.54	439
FTO/c-TiO ₂ /m-TiO ₂ /ZrO ₂ /Carbon/MAPbI ₃ /precursor solvent:DMF/DMSO	Screen-printing	400°C/30 min	932	18.07	0.76	12.79	439
FTO/c-TiO ₂ /m-TiO ₂ /ZrO ₂ /Carbon/MAPbI ₃ /precursor solvent:GBL	Screen-printing	400°C/30 min	859	12.93	0.67	7.47	439
FTO/c-TiO ₂ /m-TiO ₂ /ZrO ₂ /Carbon/MAPbI ₃ /precursor solvent:NMP	Screen-printing	400°C/30 min	766	8.78	0.56	3.77	439
FTO/c-TiO ₂ /m-TiO ₂ /super thin Al ₂ O ₃ /ZrO ₂ /Carbon/ MA _{0.965} (5-AVA) _{0.035} PbI ₃	Screen-printing	-	900	22.81	0.70	14.39	435
FTO/c-TiO ₂ /m-TiO ₂ /No ZrO ₂ /Carbon/ (5-AVA) _x MA _{1-x} PbI ₃	Screen-printing	400°C/30 min	605	16.21	0.66	6.52	425
FTO/c-TiO ₂ /m-TiO ₂ /5 nm size of ZrO ₂ /Carbon/ (5-AVA) _x MA _{1-x} PbI ₃	Screen-printing	400°C/30 min	871	16.06	0.67	9.42	425
FTO/c-TiO ₂ /m-TiO ₂ /10 nm size of ZrO ₂ /Carbon/ (5-AVA) _x MA _{1-x} PbI ₃	Screen-printing	400°C/30 min	908	18.26	0.71	11.77	425
FTO/c-TiO ₂ /m-TiO ₂ /20 nm size of ZrO ₂ /Carbon/ (5-AVA) _x MA _{1-x} PbI ₃	Screen-printing	400°C/30 min	871	19.10	0.71	11.86	425
FTO/c-TiO ₂ /m-TiO ₂ /60 nm size of ZrO ₂ /Carbon/ (5-AVA) _x MA _{1-x} PbI ₃	Screen-printing	400°C/30 min	865	18.19	0.70	11.08	425
FTO/c-TiO ₂ /m-TiO ₂ /100 nm size of ZrO ₂ /Carbon/ (5-AVA) _x MA _{1-x} PbI ₃	Screen-printing	400°C/30 min	808	18.62	0.67	10.10	425
FTO/c-TiO ₂ /m-TiO ₂ /1.2 μm ZrO ₂ /graphite: oxygen-deficient carbon black/(5-AVA) _x MA _{1-x} PbI ₃	Screen-printing	400°C/30 min	880	22.98	0.67	13.6	422

FTO/c-TiO ₂ /m-TiO ₂ /1.2 μm ZrO ₂ /graphite: oxygen-rich carbon black/(5-AVA) _x MA _{1-x} PbI ₃	Screen-printing	400°C/30 min	980	23.2	0.69	15.7	422
FTO/c-TiO ₂ /m-TiO ₂ /ZrO ₂ /carbon/(5-AVA) _x MA _{1-x} PbI ₃	Screen-printing	400°C/40 min	920	22.75	0.67	13.98	449
FTO/c-SnO ₂ /m-TiO ₂ /ZrO ₂ /carbon/(5-AVA) _x MA _{1-x} PbI ₃	Screen-printing	400°C/40 min	900	22.92	0.67	13.77	449

Abbreviations: DMF, dimethylformamide; DMSO, dimethyl sulfoxide; FTO, fluorine-doped tin oxide; GBL, gamma butyrolactone; NMP, N-Methyl-2-pyrrolidone

3.3.1.2. Conventional device architecture without an insulating layer

A triple mesoporous layer-based C-PSC requires an additional ZrO_2 insulating layer and high processing temperature for interfacial bonding. These factors increase the energy cost. Furthermore, its application for a flexible C-PSC is limited due to high temperature processing. However, the conventional device architecture for a C-PSC usually comprises FTO/c- TiO_2 /m- TiO_2 /perovskite/carbon paste or FTO/c- TiO_2 /m- TiO_2 /perovskite/HTM/carbon paste. In the above device configuration, perovskite is first deposited onto the mesoporous TiO_2 layer. Except for the perovskite crystal infiltrated into mesoporous TiO_2 , a perovskite capping layer is also built; it physically prevents direct contact of TiO_2 and the carbon BE. Thus, an insulating spacer layer is not required to reduce carrier recombination. Then, a carbon BE is deposited on top of the perovskite layer or HTM layer. Finally, the device is sintered at a low temperature—considering the instability of the perovskite layer. Moreover, low-temperature ($< 150^\circ\text{C}$) processing allows the device fabrication on the flexible substrate. Given the features of conventional device architecture for C-PSCs, in this section we discuss the carbon film, HTM incorporation, and ETM optimization.

Ma *et al.*⁴⁵⁰ developed a carbon electrode by doctor-blade coating carbon paste dispersed in chlorobenzene, followed by drying at 70°C for 40 min. The authors showed that the square resistance of carbon film is decreased as its thickness increases. And thus giving effect toward the photovoltaic performance of the device. At the optimal carbon film thickness ($\sim 20 \mu\text{m}$), the PCE is 9.08% (**Fig. 27a–g**).

A graphite layer tends to produce an interspace between the graphite flakes and perovskites due to its lamellar nature.⁴⁵¹ Thus, without a spacer layer, a HTM-free

conventional C-PSC device usually suffers from poor contact at perovskite/carbon interface. To improve the contact sites at the perovskite/carbon BE interface, Meng *et al.* investigated the effect of graphite flake size on C-PSC performance. A carbon BE made of small graphite flakes exhibits higher performance compared to when larger graphite flakes are used. This phenomenon occurs because BEs made with smaller graphite particles have more contact sites with the perovskite film and thus there is reduced charge transfer resistance during hole extraction from the perovskite to carbon BEs.⁴⁵¹ The PCE is further improved to a maximum of 10.2% when incorporating 20 wt% small CB particles (**Fig. 27h–j**). Hagfeldt *et al.*⁴⁵² developed a CB BE by incorporating a low-cost carbon cloth into the carbon paste. When a carbon cloth is embedded into carbon paste as BE for a PSC, the device exhibits a PCE up to 15.29%, with a J_{SC} of 20.4 mA/cm², an excellent V_{OC} of 1.12 V, and a high FF of 0.67. By contrast, an insulating carbon fiber embedded into the carbon paste as a control BE shows a poor PCE (8.7%) with a very low FF (0.429).

Bio-carbons are a potential carbon material with an ultra-low-cost; they can be prepared by biomass pyrolysis. Very recently, Gao *et al.*⁴⁵³ developed economical and eco-friendly bio-carbons as PSC BEs. The authors examined four biomasses—corn stalks, peanut shells, *Phragmites australis*, and bamboo chopsticks—to prepare bio-carbons via a carbonization process under nitrogen flow. The device performance of C-PSCs based on different bio-carbon BEs is affected by the combination effects from the morphology of these bio-carbons, the interfacial connection, WF, and the sheet resistance of the bio-carbons. Bamboo chopstick bio-carbons exhibit a suitable WF (4.80 eV) for better energy level alignment, lower radiative recombination, and faster carrier transport in C-PSCs compared to other bio-carbon BE based devices. Thus, the C-PSCs based on bamboo

chopstick bio-carbon BE produce the highest PCE of 12.82% (Fig. 28a–g). PSCs based on a bio-carbon BE are more stable than that of conventional devices. Indeed, they maintain 87% of the initial PCE after stored at room temperature for 2000 h.

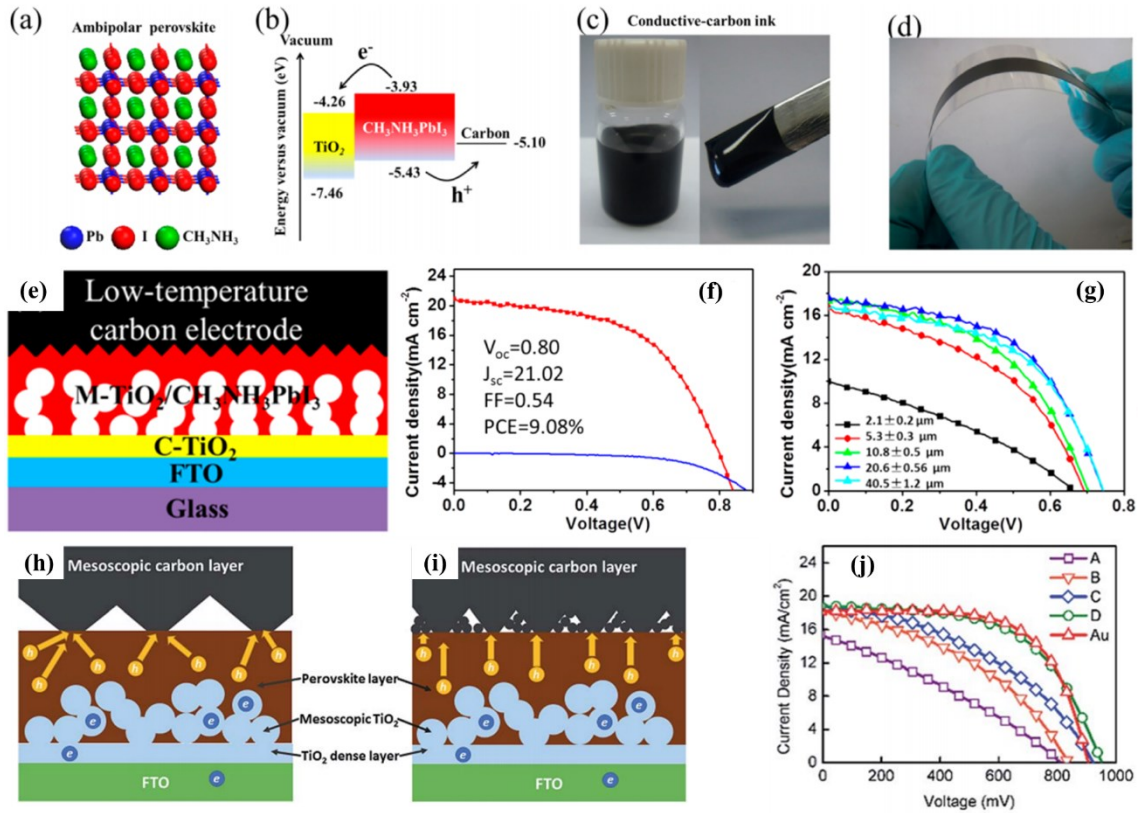


Fig. 27 a) The crystal structure of $\text{CH}_3\text{NH}_3\text{PbI}_3$. (b) An energy-level diagram of TiO_2 , $\text{CH}_3\text{NH}_3\text{PbI}_3$, and carbon. (c) Images of conductive carbon ink. (d) Conductive carbon film prepared on a plastic substrate at 70°C . (e) A schematic of the device architecture. (f) J-V characteristics of the best performing m- $\text{TiO}_2/\text{CH}_3\text{NH}_3\text{PbI}_3/\text{carbon}$ -perovskite solar cell (C-PSC) device based on a low-temperature processed carbon back electrode. (g) J-V curves of a m- $\text{TiO}_2/\text{CH}_3\text{NH}_3\text{PbI}_3/\text{C}$ -PSC devices based on various carbon back electrode (BE) thicknesses. Copyright 2014, American Chemical Society; reprinted with permission.⁴⁵⁰ A scheme of the charge transfer in a hole transporting medium (HTM)-free

CH₃NH₃PbI₃/TiO₂ heterojunction solar cells with a BE consisting of h) large graphite flakes or i) smaller graphite flakes and carbon black particles. j) The J-V curves of a HTM-free C-PSC device with various BEs. Copyright 2014, The Royal Society of Chemistry; reprinted with permission.⁴⁵¹

With regard to conventional C-PSCs, the carbon layer is directly deposited on top of the pre-deposited perovskite films. Thus, the processing solvent for the carbon paste should not damage the underlying perovskite film. The ideal processing solvent for carbon paste should possess the following properties: (i) the solvent should not dissolve the lower perovskite film; and (ii) the solvent should sufficiently dissolve the binder to ensure the homogeneity of the carbon film. Based on a detailed investigation, propylene glycol monomethyl ether acetate (PGMEA) emerged as the processing solvent for carbon paste that is most friendly to perovskite.⁴⁵⁴ A C-PSC device based on the PGMEA method shows a much higher PCE of 13.5% compared to using a device with a commercial carbon BE (5.26%). Furthermore, some fast solvent evaporation processes may be used to avoid the damage of underlying perovskite layer. Yang *et al.*⁴⁵⁵ used a simple and efficient gas pump process to significantly shorten the solvent evaporation time in the carbon paste. This procedure leads to a uniform and continuous surface morphology in the perovskite film. The as-prepared C-PrSCs based on gas pump method showed a PCE of 12.3% and a V_{OC} of 1.03 V, values that are much higher than that of the control device, with a PCE of 4.73% and V_{OC} of 0.81 V.

Separate fabrication of a carbon film followed by stacking it on the perovskite layer represents another solution to avoid possible damage to the perovskite layer. However,

there is reduced interfacial bonding at the perovskite and carbon interface. To address this drawback, Meng *et al.*⁴⁵⁶ fabricated a free-standing flexible carbon film containing 20%wt thermoplastic poly(vinyl acetate) (PVAc) as a BE by doctor blading. They then directly hot-pressed the BE on top of perovskite film at 85°C. Strong interfacial bonding is formed during hot pressing due to the thermoplasticity of PVAc. After optimizing the weight ratio of graphite flakes and CB in the carbon film, the champion device based on the free-standing carbon film exhibits a PCE of 13.53%.

To improve interface contact between the perovskite layer and carbon BE, while maintaining efficient charge separations and enhancing the hole extraction ability, HTMs are usually inserted between the perovskite layer and carbon BE.^{452,457–461} Sun *et al.* observed a remarkable PCE of 16.1% by incorporating CuPc nanorods as an HTM to enhance hole extraction between the MAPbI₃ film and carbon BE (**Fig. 28h–k**).⁴⁶² The CuPc nanorods are usually deposited via thermal vapor deposition, which is complicated (e.g. high-vacuum conditions are required) and costly due to the poor solubility of CuPc. To improve CuPc solubility, the authors developed a solution-processable CuPc-TIPS with hydrophobic triisopropylsilylethynyl (TIPS) groups. The champion C-PSC based on CuPc-TIPS exhibits the highest efficiency of 14.0%. Furthermore, the device exhibits good long-term stability in the dark at ambient conditions (~ 35% relative humidity). After 720 h, the best device maintained about 90% of its initial PCE (from 14.0% to 12.5%) because the hydrophobic CuPc-TIPS HTM interlayer prevents moisture from penetrating the perovskite layer.⁴⁶³ Another group incorporated the small organic molecule 5,10,15-triphenyl-5Hdiindolo[3,2-a:3',2'-c]carbazole (TPDI) into C-PSCs as a HTM; this process does not require a vacuum. This device has a PCE 15.5% and a FF up to 0.75.⁴⁶⁴ Li *et al.*⁴⁶⁵

incorporated an inorganic HTM (NiO_x nanoparticles) into carbon paste and found a PCE of 13.26% compared to 10.29% of a device with a pure carbon BE. Moreover, the C-PSC maintains 85% of the initial efficiency after storage at ambient conditions for 800 h.

From perovskite film processing, to improve the interfacial contact of perovskite/carbon layer, Meng *et al.*⁴⁶⁶ proposed a solvent engineering method based on a two-step sequential method to realize a uniform and compact perovskite capping layer. They hypothesized that this process will enhance the contact between the perovskite layer and the carbon BE (mainly composed of CB and graphite flakes). They obtained the highest PCE of 14.38% with a FF of 0.65 and a PCE of 10% for the device with a 1 cm^2 area.⁴⁶⁶ Moreover, through colloidal engineering to form ultra-even perovskite layer, they further boosted the efficiency of the C-PSC to 14.58%.⁴⁶⁷

Some strategies from the aspects of the ETMs optimization, such as the optimization of TiO_2 thickness,⁴⁶⁸ the chemical doping of TiO_2 ^{469–471} or SnO_2 ,⁴⁵⁸ the size and morphology of TiO_2 ,^{472–475} its surface modification,^{476–478} and a bilayer of $\text{TiO}_2/\text{SnO}_2$ ⁴⁷⁹ improve C-PSC performance.

It was observed that the TiO_2 thickness also affected the device performance. In 2014, Sun's group⁴⁶⁸ deposited a low-temperature-processed (100°C) carbon BE by doctor-blading technology. They then deposited the carbon BE on the already-deposited perovskite layer. After optimization, the HTM-free perovskite/ TiO_2 device achieves a remarkable efficiency of 8.31% and excellent stability over 800 h (see **Fig. 28 I-o**).

To improve the electron injection efficiency as well as the stability of C-PSCs upon exposure to UV light, Zhao *et al.*⁴⁶⁹ developed W-doped TiO_2 to enhance electron

conductivity. The C-PSC based on W-TiO₂ exhibits a high PCE up to 12.06% with an improved J_{SC} and FF value due to facilitated electron transfer efficiency. Another group investigated Ni-doped rutile TiO₂ as an ETM in planar C-PSCs.⁴⁷⁰ Ni doping shifted up the Fermi level of TiO₂ and also increases its electron mobility; these phenomena enhance electron extraction and carrier transport. The planar C-PSC based on 0.01 M Ni doped TiO₂ as the ETM (optimal doping level) and with CuPc as the HTM has a PCE up to 17.46%, which is higher than that of using pristine TiO₂, with a PCE of 15.82%. The device also exhibits excellent stability, with a retention of > 97% of its initial efficiency after stored in ambient air for 1200 h. These works indicate that TiO₂ with appropriate heteroatom doping can improve the efficiency and enhance the stability of C-PSCs.

Coating an additional layer (MgTiO₃,⁴⁷⁶ PC₆₁BM,⁴⁷⁷ or MgO^{478,480}) onto the surface of TiO₂ was demonstrated to be an effective strategy to improve device performance by reducing interfacial charge recombination. Huang *et al.*⁴⁷⁸ coated an ultrathin wide bandgap MgO layer onto mesoporous TiO₂. Together with modulating perovskite crystallization with a terephthalic acid additive, the C-PSC device shows a high average PCE of 14.29%. Considering the high temperature sintering and photocatalytic-activity of the TiO₂, Zhou *et al.*⁴⁸¹ employed SnO₂ with high electron mobility and low photo-catalytic activity as the ETM for planar C-PSCs. With (FAPbI₃)_{0.97}(MAPbBr₃)_{0.03} as the light harvesting material and CuPc as the HTM, the prepared C-PSC based on SnO₂ shows a higher PCE of 14.2% compared to a C-PSC based on TiO₂ (10.46%), with excellent storage stability up to 3600 h. Later, Liao *et al.*⁴⁷⁹ utilized a TiO₂/SnO₂ bilayer as the ETM and CuPc as the HTM for C-PSCs. Attributed to the better energy level alignment and inhibited electron-hole recombination, C-PSCs based on the TiO₂/SnO₂ bilayer shows a best efficiency of 15.39%

and excellent stability over 1200 h. **Table 9** exhibits the summary information of carbon-based perovskite solar cells with device structure of TiO₂/perovskite/carbon past.

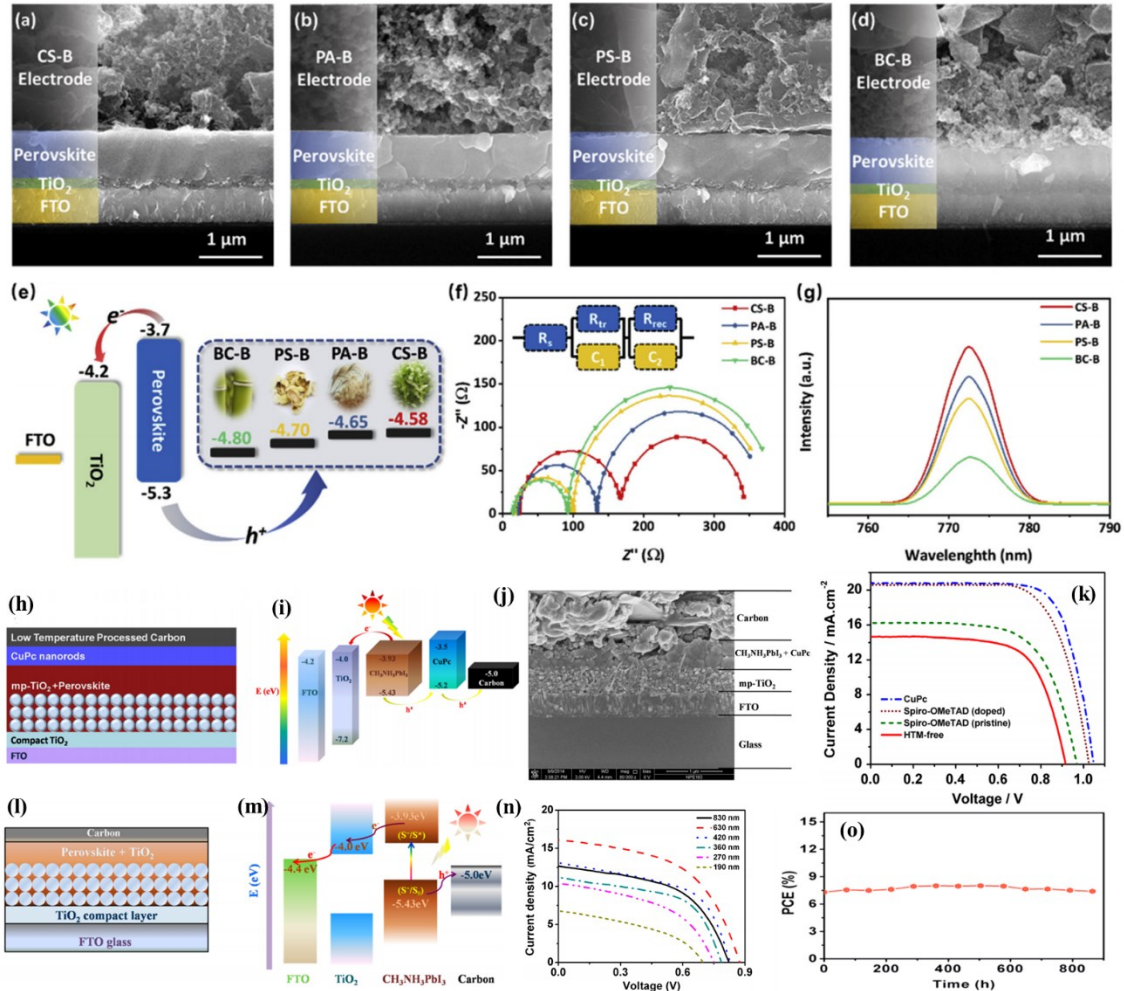


Fig. 28 Cross-sectional scanning electron microscopy (SEM) images of a carbon-based perovskite solar cell (C-PSC) with a (a) corn stalk-based back electrode (CS-B), (b) *Phragmites australis*-based back electrode (PA-B), (c) peanut shell-based back electrode (PS-B), and (d) BC-B (bamboo chopstick-based back electrode). (e) Energy level diagram of the C-PSC devices based on different bio-carbon electrodes. (f) The Nyquist plots and the fitted equivalent circuit were carried out based on different bio-carbon BEs. (g) The steady-state PL spectra of the fluorine-doped tin oxide (FTO)/c-TiO₂/m-TiO₂/perovskite/biocarbon BEs. Copyright 2020, Elsevier; reprinted with permission.⁴⁵³ (h) A schematic of the entire device configuration. (i) The corresponding energy level

diagram. (j) Cross-sectional view of the whole device. (k) J-V curves of C-PSC based on various hole transporting media (HTM) measured under one sun illumination. Copyright 2016, Elsevier; reprinted with permission.⁴⁶² (l) Device configuration of the C-PSC. (m) Energy levels diagrams of various device components. (n) J-V curves of C-PSCs based on different TiO₂ film thicknesses. (o) Long-term monitoring of the device performance stored in ambient atmosphere at room temperature without encapsulation. Copyright 2014, American Chemical Society; reprinted with permission.⁴⁶⁸

Table 9. Summary of photovoltaic parameters for different carbon-based perovskite solar cells with the conventional device configuration TiO₂/perovskite/carbon past.

Device configuration	Deposition method	Thermal treatment	V_{OC} (mV)	J_{SC} (mA cm ⁻²)	FF	η (%)	Ref.
FTO/c-TiO ₂ /190 nm m-TiO ₂ /MAPbI ₃ /Carbon	doctor-blading	100°C/30 min	700	6.94	41.09	2.00	468
FTO/c-TiO ₂ /270 nm m-TiO ₂ /MAPbI ₃ /Carbon	doctor-blading	100°C/30 min	750	10.43	47.72	3.71	468
FTO/c-TiO ₂ /360 nm m-TiO ₂ /MAPbI ₃ /Carbon	doctor-blading	100°C/30 min	780	11.43	55.08	4.91	468
FTO/c-TiO ₂ /420 nm m-TiO ₂ /MAPbI ₃ /Carbon	doctor-blading	100°C/30 min	830	13.41	54.28	6.02	468
FTO/c-TiO ₂ /630 nm m-TiO ₂ /MAPbI ₃ /Carbon	doctor-blading	100°C/30 min	870	16.10	52.60	7.40	468
FTO/c-TiO ₂ /830 nm m-TiO ₂ /MAPbI ₃ /Carbon	doctor-blading	100°C/30 min	820	12.67	52.60	5.48	468
FTO/c-TiO ₂ /450 nm m-TiO ₂ /MAPbI ₃ (by sequential deposition)/Carbon paste (composed of 95 wt% graphite flakes [20 μ m in size] + 0 wt% carbon black)	screen-printing	Room temperature 15 min	816.3	15.29	0.30	3.76	451
FTO/c-TiO ₂ /450 nm m-TiO ₂ /MAPbI ₃ (by sequential deposition)/Carbon paste (composed of 95 wt% graphite flake (3 μ m in size) + 0 wt% carbon black)	screen-printing	Room temperature 15 min	837.2	18.30	0.40	6.16	451
FTO/c-TiO ₂ /450 nm m-TiO ₂ /MAPbI ₃ (by sequential	screen-printing	Room temperature	921.2	18.85	0.42	7.21	451

deposition)/Carbon paste (composed of 95 wt% graphite flake (1 μ m in size) + 0 wt% carbon black)		15 min						
FTO/c-TiO ₂ /450 nm m-TiO ₂ /MAPbI ₃ (by sequential deposition)/Carbon paste (composed of 75 wt% graphite flake (1 μ m in size) + 20 wt% carbon black)	screen-printing	Room temperature 15 min	953	18.73	0.57	10.2	451	
FTO/c-TiO ₂ /450 nm m-TiO ₂ /MAPbI ₃ (by sequential deposition)/Au (as control device)	screen-printing	Room temperature 15 min	911	18.15	0.65	10.73	451	
FTO/c-TiO ₂ /m-TiO ₂ /MAPbI ₃ /CuPc/Carbon	doctor-blading	100°C/30 min	1050	20.8	0.74	16.1	462	
FTO/c-TiO ₂ /m-TiO ₂ /MAPbI ₃ /doped spiro-OMeTAD/Carbon	doctor-blading	100°C/30 min	1030	20.6	0.71	15.0	462	
FTO/c-TiO ₂ /m-TiO ₂ /MAPbI ₃ /non-doped spiro-OMeTAD/Carbon	doctor-blading	100°C/30 min	970	16.2	0.66	10.4	462	
FTO/c-TiO ₂ /m-TiO ₂ /MAPbI ₃ /HTM-free/Carbon	doctor-blading	100°C/30 min	920	14.7	0.67	9.0	462	
FTO/c-TiO ₂ /m-TiO ₂ /(FAPbI ₃) _{0.85} (MAPbBr ₃) _{0.15} / pristine CuPc- TIPS/Carbon	doctor-blading	100°C/30 min	1010	21.4	0.65	14.0	463	
FTO/c-TiO ₂ /m-TiO ₂ /(FAPbI ₃) _{0.85} (MAPbBr ₃) _{0.15} / pristine spiro- OMeTAD /Carbon	doctor-blading	100°C/30 min	980	18.1	0.56	9.9	463	
FTO/c-TiO ₂ /m-TiO ₂ /(FAPbI ₃) _{0.85} (MAPbBr ₃) _{0.15} / doped spiro- OMeTAD/Carbon	doctor-blading	100°C/30 min	1020	22.2	0.70	15.8	463	
FTO/c-TiO ₂ /m-TiO ₂ /MAPbI ₃ /doped-TPDI/Carbon	doctor-blading	100°C/30 min	1030	20.1	0.75	15.5	464	

FTO/c-TiO ₂ /m-TiO ₂ /MAPbI ₃ /pristine-TPDI/Carbon	doctor-blading	100°C/30 min	1030	18.7	0.71	13.6	464
FTO/Ni doped TiO ₂ / Cs ₅ (MA _{0.17} FA _{0.83}) ₉₅ Pb(I _{0.83} Br _{0.17}) ₃ /CuPc/Carbon	doctor-blading	85°C/15 min	1073	22.41	0.726	17.46	470
FTO/TiO ₂ /Cs ₅ (MA _{0.17} FA _{0.83}) ₉₅ Pb(I _{0.83} Br _{0.17}) ₃ /CuPc/Carbon	doctor-blading	85°C/15 min	1040	21.76	0.699	15.82	470
FTO/Ni doped TiO ₂ /Cs ₅ (MA _{0.17} FA _{0.83}) ₉₅ Pb(I _{0.83} Br _{0.17}) ₃ /Carbon	doctor-blading	85°C/15 min	913	18.94	0.624	10.79	470
FTO/TiO ₂ /Cs ₅ (MA _{0.17} FA _{0.83}) ₉₅ Pb(I _{0.83} Br _{0.17}) ₃ /Carbon	doctor-blading	85°C/15 min	875	18.15	0.609	9.67	470
	doctor						
FTO/c-TiO ₂ /m-TiO ₂ /Cs ₅ (MA _{0.17} FA _{0.83}) ₉₅ Pb(I _{0.83} Br _{0.17}) ₃ / spiro-OMeTAD/Carbon cloth embedded in carbon paste	blading/hot- pressure transfer	70°C/10 min	1120	20.42	0.670	15.29	452
	Doctor-						
FTO/c-TiO ₂ /m-TiO ₂ /Cs ₅ (MA _{0.17} FA _{0.83}) ₉₅ Pb(I _{0.83} Br _{0.17}) ₃ /spiro-OMeTAD/insulating cloth embedded in carbon paste	blading/hot- pressure transfer	70°C/10 min	1080	18.42	0.429	8.7	452
	doctor-blading						
FTO/c-TiO ₂ /m-TiO ₂ /MAPbI ₃ /free-standing carbon film (Graphite/CB=1:0)	/Hot-press	85°C/15 s	967	18.77	0.566	10.27	456
	doctor-blading						
FTO/c-TiO ₂ /m-TiO ₂ /MAPbI ₃ /free-standing carbon film (Graphite/CB=5:1)	/Hot-press	85°C/15 s	982	20.03	0.581	11.43	456
	doctor-blading						
FTO/c-TiO ₂ /m-TiO ₂ /MAPbI ₃ /free-standing carbon film (Graphite/CB=3:1)	/Hot-press	85°C/15 s	1002	21.30	0.634	13.53	456

FTO/c-TiO ₂ /m-TiO ₂ /MAPbI ₃ /free-standing carbon film (Graphite/CB=2:1)	doctor-blading /Hot-press	85°C/15 s	973	20.57	0.623	12.47	456
FTO/c-TiO ₂ /m-TiO ₂ /MAPbI ₃ /Commercial carbon paste (control)	doctor-blade	100°C/-	930	11.73	0.480	5.26	454
FTO/c-TiO ₂ /m-TiO ₂ /MAPbI ₃ /Carbon paste (processing solvent: PGMEA)	doctor-blade	100°C/-	1050	20.25	0.630	13.5	454
FTO/c-TiO ₂ /m-TiO ₂ /MAPbI ₃ /Carbon paste (processing solvent: terpineol)	doctor-blade	100°C/-	730	18.20	0.360	4.77	454
FTO/c-TiO ₂ /m-TiO ₂ /MAPbI ₃ /Carbon (slow drying)	screen-printing	100°C/20 min	810	14.6	0.400	4.73	455
FTO/c-TiO ₂ /m-TiO ₂ /MAPbI ₃ /Carbon (gas pump involved fast drying)	screen-printing	100°C/3 min	1030	21.4	0.560	12.3	455
Abbreviations: FTO, fluorine-doped tin oxide; PGMEA, propylene glycol monomethyl ether acetate.							

3.3.2. Carbon nanotubes (CNTs) for PSCs

CNTs possess excellent thermal and electrical conductivity and are very hydrophobic and highly stable. Hence, they have attracted much attention for electronic and optoelectronic applications.⁴⁸² CNTs have been employed as p-type contacts for organic or inorganic solar cells.^{483,484} They possess a suitable WF value in the range of 4.7 to 5.1 eV,^{485,486} enabling them to be a potential BE or HTM for PSCs. In this section, we summarize the recent progress of CNTs as BEs, including their function in the hole transporting layer. Based on their characteristics, an isolated CNT layer has usually been applied as a BE for conventional C-PSC devices. On the other hand, CNTs with a p-type character and high mobility can be an efficient additive to embed into perovskite layer^{487,488} or the carbon film^{488,489} to improve the hole extraction at the perovskite/carbon BE interface.

Li *et al.* first employed CNTs as a PSC BE.⁴⁹⁰ They dripped anti-solvent toluene onto the top of the CNT film after the deposition on the perovskite layer to improve the physical interfacial contact of CH₃NH₃PbI₃/CNTs. Toluene does not damage the underlying perovskite film; rather, it wets the surface of both films and thus improves the CH₃NH₃PbI₃/CNT contact. The photoluminescence quenching results indicate the strong adhesion through van der Waals interactions between CH₃NH₃PbI₃ and CNT films. Thus, PSC devices based on this laminated CNT show a PCE of 6.87%, which is higher than 5.14% from a device with an Au BE (**Fig. 29a–e**). However, the interfacial surface contact between perovskite and CNT suffered an inferior contact. To improve the interfacial surface between the staking of perovskite and CNT, Jang *et al.*⁴⁸⁷ dripped anti-solvent containing multi-walled carbon nanotubes (MWCNTs) on perovskite layer prior to the thermal annealing of the perovskite film. This process successfully incorporates MWCNTs

into the grain boundaries of the perovskite film to form CNT-perovskite heterojunction, providing channel for rapid hole extraction from perovskite to carbon back electrode. The device based on carbon BE prepared by screen printing by utilizing this strategy showed a high efficiency of 13.57% with less hysteresis, which is attributed to the improved interfacial contact of perovskite and the carbon BE and reduced series resistance (R_s) and charge transfer resistance (R_h).

Yang *et al.*⁴²⁹ successfully deposited an MWCNT film onto a perovskite film with a seamless contact at the interface of perovskite/MWCNT by a simple ultrasound spray method. The control device based on drop-casted MWCNT BE exhibits a poor PCE of 12.08%, J_{SC} of 19.31 mA/cm², FF of 0.712, and V_{OC} of 0.88. However, a C-PSC based on ultrasound spray MWCNT BE shows a higher PCE up to 14.07%, as well as an improved J_{SC} of 21.03 mA/cm² and a remarkably high FF of 0.744 and V_{OC} of 0.899 V. This device also shows excellent long-term stability and exhibits almost zero PCE loss after storage in a dry box (15% relative humidity) for 3000 h. Li *et al.* proposed a CNT bridging method for device fabrication by incorporating SWCNTs in both the perovskite and carbon layers to form a high-quality perovskite/carbon interface (**Fig. 29f-i**).⁴⁸⁸ The penetrated CNT bridges into both the CH₃NH₃PbI₃ layer and the carbon BE not only facilitated hole extraction at the interface of CNTs inserted CH₃NH₃PbI₃ film/CNTs incorporated carbon films but also promoted the conductivity of the carbon BE. Attributed to such merits, the prepared C-PSC shows a high PCE up to 15.73% with a good FF of 0.72. Moreover, the CNT bridging method enables the PSC to retain an excellent long-term stability over 90 days under severe conditions (65 ± 5% relative humidity at 25 ± 5°C and 25 ± 5% relative humidity at 75 ± 5°C).

When MWCNT BE was compared with graphite and CB BE. They found that MWCNT tightly attaches to the perovskite layer to form a consecutive and crack-free thin film. The compact MWCNT morphology with the improved contact with the perovskite layer enhances the FF and photovoltaic performance of a HTM-free C-PSC. Furthermore, the MWCNT-based device shows a negligible hysteresis effect. By optimizing the thickness of PbI_2 precursor layer and MWCNT layer, a hysteresis-free PCE of 12.67% with an FF of up to 0.80 was achieved.⁴⁹¹ Due to the better hole extraction and hole mobility of CNTs compared to CB, Wang *et al.*⁴⁸⁹ used a BE that comprises printed carbon paste containing SWCNTs on the top of Al_2O_3 . With this technique, hole extraction from the perovskite to carbon BE is significantly boosted owing to the excellent hole mobility of SWCNTs. After optimization, the champion device based on a carbon BE containing 0.05 wt% SWCNTs achieves an efficiency up to 14.7%, with a high V_{OC} of 1.01 V and a FF of 0.69.⁴⁸⁹ Under the same conditions, the control device without SWCNTs in the carbon BE shows a lower PCE of 9.9% ($V_{\text{OC}} = 0.889$ V and FF = 0.55). SWCNT incorporation in the carbon BE modifies the WF and also reduces the charge recombination. These phenomena are helpful to improve the V_{OC} and FF of the device performance.

To increase V_{OC} and hole extraction efficiency, optimum energy level alignment is crucial. The WF of MWCNT is very high compared to the valence band (VB) of perovskite; hence, doping MWCNT with atoms that are electron deficient or rich can provide better energy level alignment with perovskite. Yang *et al.*⁴⁹² doped MWCNTs with B to decrease the WF and boost hole extraction at the perovskite/MWCNT interface (**Fig. 29j–l**). Together with the benefits of an additional physical barrier (Al_2O_3) layer coating onto m-TiO_2 to reduce the charge recombination, this device achieves a high PCE up to 15.23%.

Moreover, the device maintains 85% and 93% of its highest PCE without encapsulation after 2 weeks of storage under thermal stress (80°C) and high humidity (~65% at 25°C), respectively. These outcomes are attributed to the hydrophobic characteristic of the MWCNTs and the compact interlinked MWCNT network films.

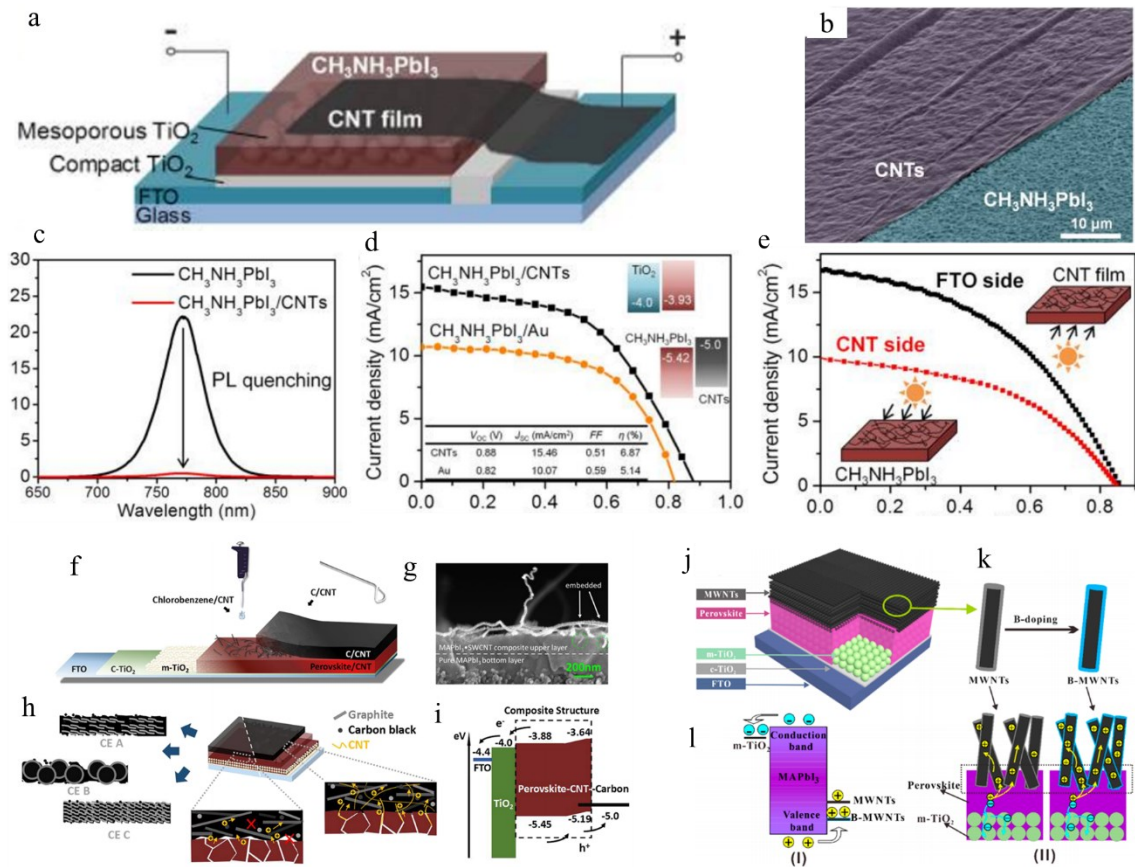


Fig. 29 (a) Schematic of a perovskite solar cell (PSC) with a carbon nanotube (CNT) back electrode (BE). (b) A tilted scanning electron microscopy (SEM) image of CH₃NH₃PbI₃ perovskite substrate (blue) partly covered by a CNT electrode (purple). (c) Steady-state photoluminescence (PL) spectra of perovskite and perovskite/CNTs. (d) J-V curves of PSCs based on Au or CNT BEs under one sun illumination. (e) J-V curves of PSCs based

on CNT BE under different illumination direction. Copyright 2014, American Chemical Society; reprinted with permission.⁴⁹⁰ (f) The schematic for device fabrication of paintable PSCs based on the CNT bridge method. (g) A cross-sectional SEM image of CNTs embedded in MAPbI₃. (h) A schematic of hole extraction and transport at the MAPbI₃/different carbon BE interface with/without the CNT bridging. (i) An energy level diagram of the related layers in a C-PSC device. Copyright 2019, American Chemical Society; reprinted with permission.⁴⁸⁸ A schematic illustration of cell configuration, boron (B) doping of multi-walled carbon nanotube (MWCNTs), and charge behavior in C-PSCs. (j) A schematic illustration of the C-PSC configuration. (k) A schematic diagram of B doping of MWNTs to B-MWNTs. (l) A schematic illustration of charge transfer enhancement by B-MWNTs through in I shows reduced E_F of MWNTs, while II presents what happens when increasing the number of conduction carriers in the B-MWNT electrode. The intimate interface between perovskite and MWNTs is marked by black dotted rectangle in II. Copyright 2017, American Chemical Society; reprinted with permission.⁴⁹²

Insertion of an HTM in the perovskite/CNT interface is an effective way to boost hole extraction and reduce interfacial recombination. Aitola *et al.*⁴⁹³ developed a spiro-OMeTAD infiltrated SWCNT as a C-PSC BE. They deposited the SWCNT film, prepared by the CVD method, on top of the perovskite film by a press-transfer process. They then densified the coated SWCNT film by dropping a small amount of chlorobenzene. To lower the SWCNT BE sheet resistance, they transferred double SWCNT layers onto the perovskite film. The C-PSC device with the above-described BE but without an HTM

shows a poor efficiency of 11%. By contrast, a device based on spiro-OMeTAD infiltrated SWCNT BE has a PCE up to 15.5%. Choi *et al.*⁴⁹⁴ developed carbon sandwiched PSCs with C₆₀ as the ETM and MAPbI₃ as perovskite light absorbing film, together with the infiltration of spiro-OMeTAD into SWCNT. The prepared PSC device shows a markedly higher PCE (17%) compared to polymeric poly(triaryl amine) (PTAA) and poly(3-hexylthiophene) (P3HT) HTM. Indeed, this is a record-high PCE among the laminated CNT BE-based PSCs. Wu *et al.* inserted an inorganic copper(I) thiocyanate (CuSCN) as an HTM between the perovskite and the carbon BE to reduce the electron recombination process.⁴⁸² As a result, the updated CuSCN and CNT incorporated C-PSC device exhibits a V_{OC} of 1.01 V and a PCE up to 17.58%, as well as enhanced long-term stability (**Fig. 30a–d**).

Guo *et al.*⁴⁹⁵ developed a flexible PSC with an all-carbon electrode by using graphene as a transparent anode and CNTs as the BE. A flexible device containing this all-carbon electrode with and without spiro-OMeTAD HTM shows a PCE of 11.9% and 8.4%, respectively (**Fig. 30e–h**). The devices also exhibit good robustness against mechanical deformation compared to counterparts fabricated on a flexible ITO substrate. The flexible PSC with an all-carbon electrode also shows noticeably enhanced stability compared to the flexible PSCs based on Au or Ag BE under continuous light soaking or 60°C thermal stress in air, retaining over 90% of its original PCEs after 1000 h. To enhance the built-in potential and reduce the non-radiative recombination in C-PSCs, Yang *et al.*⁴⁹⁶ inserted an ultrathin ferroelectric perovskite oxide (PbTiO₃) layer between the TiO₂ layer and the perovskite film. The prepared C-PSC shows a remarkable PCE of 16.37%. The significantly improved V_{OC} and PCE are mainly attributed to the enhanced built-in potential in the prepared C-

PSC device and reduced non-radiative recombination due to the incorporation of a ferroelectric PbTiO_3 layer (**Fig. 30i–l**). **Table 10** shows the summary information of carbon-based perovskite solar cells with conventional device configuration and using carbon nanotubes (CNTs) as the back electrode.

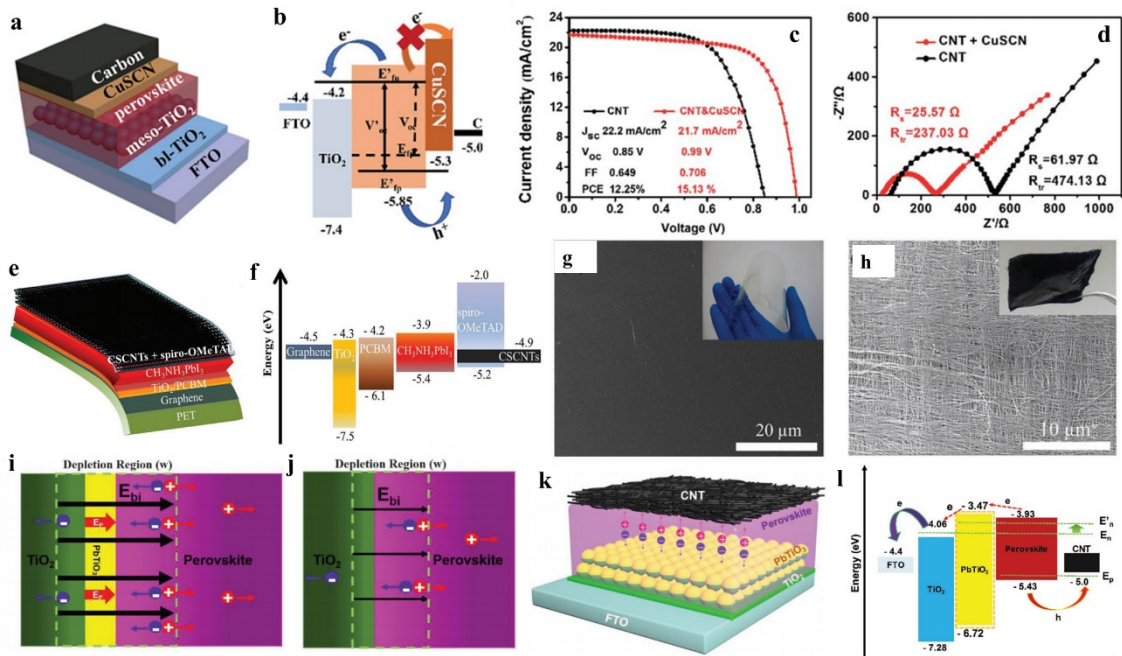


Fig. 30 a) A schematic of a carbon-based perovskite solar cell (C-PSC) with copper(I) thiocyanate (CuSCN) and b) the corresponding energy level diagram of each layer. c) J-V curves and d) the impedance spectra of the HTM-free and CuSCN-based C-PSCs. Copyright 2019, The Royal Society of Chemistry; reprinted with permission.⁴⁸² e) A schematic of a flexible PSC with an all-carbon electrode and f) the corresponding energy level diagram of each layer. Surface scanning electron microscopy (SEM) images of g) graphene/polyethylene terephthalate (PET) substrate and h) cup-stacked carbon nanotubes (CSCNTs). The insets in (g) and (h) show a photograph of the graphene/PET and CSCNTs,

respectively. Copyright 2018, WILEY-VCH; Reprinted with permission.⁴⁹⁵ Schematic diagrams presenting the depletion regions in C-PSC devices i) with and j) without the ferroelectric oxide PbTiO_3 . k) A schematic of a C-PSC device with PbTiO_3 and l) the energy level diagram of each layer. Copyright 2019, WILEY-VCH; reprinted with permission.⁴⁹⁶

Table 10. Summary of photovoltaic parameters of carbon-based perovskite solar cells with a conventional device configuration and using carbon nanotubes (CNTs) as the back electrode.

Device configuration	Deposition method	Thermal treatment	V_{OC} (mV)	J_{SC} (mA cm ⁻²)	FF	η (%)	Ref.
FTO/c-TiO ₂ /mp-TiO ₂ /MAPbI ₃ /spiro-OMeTAD/Au (control)			820	10.7	0.59	5.14	490
FTO/c-TiO ₂ /mp-TiO ₂ /MAPbI ₃ /CNTs	Lamination	-/-	0.88	15.46	0.51	6.87	490
FTO/c-TiO ₂ /mp-TiO ₂ /MAPbI ₃ /spiro-OMeTAD/CNTs	Lamination	-/-	1000	18.1	0.55	9.9	490
FTO/c-TiO ₂ /mp-TiO ₂ /MAPbI ₃ /MWCNTs	Drop-casting	50°C/5 min	0.88	18.00	0.80	12.67	491
FTO/c-TiO ₂ /mp-TiO ₂ /MAPbI ₃ /CNTs@P3HT	drop-casting	50°C/10 min and 100°C/20 min	0.91	22.71	0.65	13.43	497
FTO/c-TiO ₂ /mp-TiO ₂ /Al ₂ O ₃ /CSCNT-25/(MAPbI ₃)	Physical stacking	-/-	0.878	14.43	0.53	6.81	498
FTO/c-TiO ₂ /mp-TiO ₂ /Al ₂ O ₃ /CSCNT-50/(MAPbI ₃)	Physical stacking	-/-	0.849	14.91	0.68	8.60	498
FTO/c-TiO ₂ /mp-TiO ₂ /Al ₂ O ₃ /CSCNT-75/(MAPbI ₃)	Physical stacking	-/-	0.823	15.81	0.64	8.35	498
FTO/c-TiO ₂ /mp-TiO ₂ /Al ₂ O ₃ /T-CSCNT-50/(MAPbI ₃)	Physical stacking	-/-	0.84	16.21	0.69	9.37	498
FTO/c-TiO ₂ /mp-TiO ₂ /Al ₂ O ₃ /I-CSCNT-50/(MAPbI ₃)	Physical stacking	-/-	0.853	17.22	0.71	10.54	498
FTO/c-TiO ₂ /mp-TiO ₂ /MAPbI ₃ /carbon black: flaky	doctor-blading	100°C/60 min	0.936	19.44	0.64	11.72	488

graphite of 12 500 mesh=1:3 (mass ratio)								
FTO/c-TiO ₂ /mp-TiO ₂ /MAPbI ₃ /carbon black: 8 μm spheroidal graphite=1:3 (mass ratio)	doctor-blading	100°C/60 min	0.941	19.76	0.68	12.63	488	
FTO/c-TiO ₂ /mp-TiO ₂ /MAPbI ₃ /carbon black: flaky graphite of 15,000 mesh=1:3 (mass ratio)	doctor-blading	100°C/60 min	0.950	20.92	0.70	13.86	488	
FTO/c-TiO ₂ /mp-TiO ₂ /MAPbI ₃ (incorporated SWCNTs by dripping anti-solvent)/ carbon black: flaky graphite of 15,000 mesh=1:3 (mass ratio) containing SWCNTs	doctor-blading	100°C/60 min	0.974	22.36	0.72	15.73	488	
FTO/c-TiO ₂ /m-TiO ₂ /MAPbI ₃ /CNTs	lamination process	-/-	0.860	16.7	0.440	6.29	490	
FTO/c-TiO ₂ /m-TiO ₂ /MAPbI ₃ /CNTs	lamination process	-/-	0.850	9.9	0.460	3.88*	490	

Abbreviations: FTO, fluorine-doped tin oxide; MW, multi-walled; SW, single-walled. *Indicates the efficiency from back side containing semi-transparent CNT electrode

3.3.3. Graphene for PSCs

Graphene, a 2D material, possesses excellent electric conductivity and high mobility, transparency, mechanical flexibility, and specific surface area. Thus, graphene is also considered to be an ideal BE with transparency for C-PSCs. Yan *et al.*⁴⁹⁹ prepared a semi-transparent PSC by employing stacked multilayer graphene as a transparent BE onto a PEDOT:PSS layer (**Fig. 31a–d**). They deposited the transparent graphene BE on perovskite films by a facile lamination process under pressure at low temperature ($\approx 60^\circ\text{C}$), which is compatible with printing and roll-to-roll processing. After optimization, the device with a double-layer graphene BE exhibits the maximum PCE of $12.02\% \pm 0.32\%$ under illumination from the FTO side and $11.65\% \pm 0.35\%$ under illumination from the graphene side. Their work indicates that graphene may be an ideal transparent BE material for metal electrode free-based PSCs and tandem photovoltaic devices that utilize perovskite.⁵⁰⁰

Zhu *et al.*⁵⁰¹ developed nitrogen-doped graphene frameworks (N-GFs) as an excellent carbon BE for an HTM-free C-PSC. The WF of the graphene frameworks are decreased from 5.22 eV of GF to 4.92 eV of N-GF, and thus leading to a more efficient hole extraction from the perovskite film to the carbon BE. A C-PSC with a N-GF-based BE shows a PCE of 10.32%, higher than the PCE of a C-PSC using an undoped graphene frameworks (**Fig. 31e–h**). This enhanced performance is probably due to the superiority of N-GFs in enabling increased charge extraction and transport with reduced charge recombination. This work demonstrates that an N-GF may be a potential BE material to replace expensive organic HTM and noble metal electrodes (Au/Ag) for constructing efficient and low-cost HTM-free C-PSC devices.

Considering the difficult deposition of large scale CVD graphene, rGO is another potential carbon BE material for C-PSCs. Yang *et al.*⁵⁰² employed rGO to investigate the effects of WF of graphene on device performance (**Fig. 31i-l**). First, GO is chemically cleaved from expanded natural graphite flakes, and then single-layer graphene (SG), with a WF of 4.8 eV, and multilayer graphene (MG), with WF of 5.0 eV, are synthesized from the reduction of their oxide (SGO and MGO, respectively) at 1000°C under an argon atmosphere. Notably, there is a Schottky junction with a rectifying characteristic formed at the MG/perovskite interface that enables effective hole extraction and electron blocking. However, the SG/perovskite interface contact exhibits an ohmic contact behavior with recombination. Thus, the PSC based on a MG BE shows a much high PCE of 11.5%, with a J_{sc} of 16.7 mA cm⁻², a FF of 0.73, and a V_{oc} of 0.943 V, compared to a SG-based PSC, with a PCE of 6.7%, a J_{sc} of 14.2 mA cm⁻², a FF of 0.54, and a V_{oc} of 0.878 V.

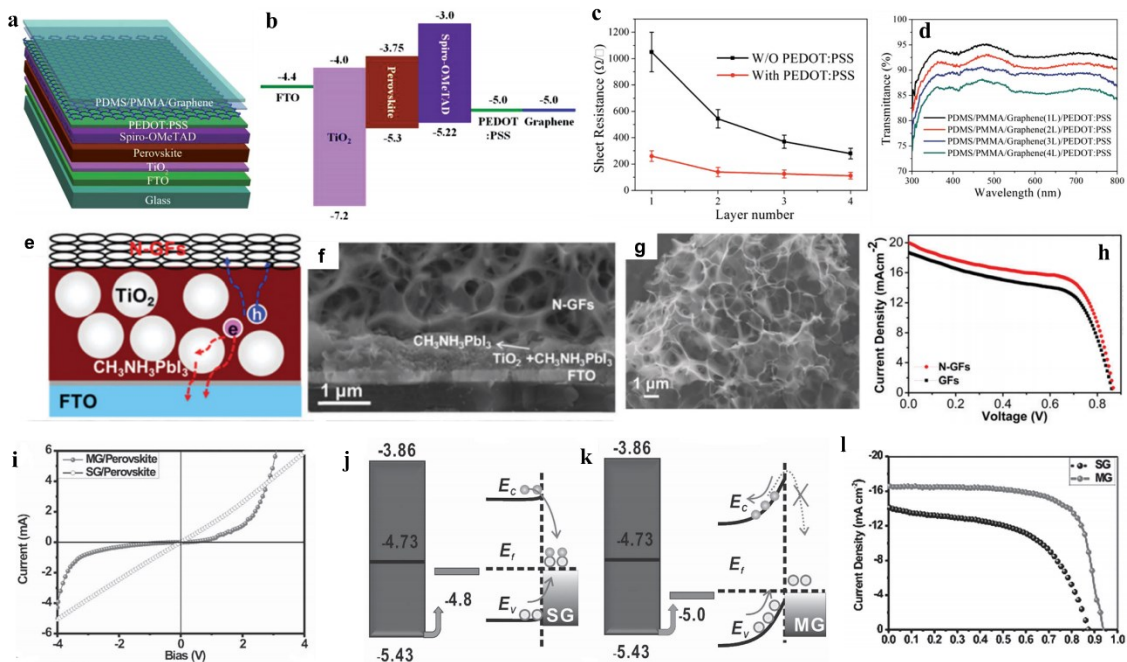


Fig. 31 a) A schematic for a semitransparent carbon-based perovskite solar cell (C-PSC) and b) the energy level diagram of each related layer. c) The R_{sh} of one to four layers of

stacked graphene films before and after poly(3,4-ethylenedioxythiophene) polystyrene sulfonate (PEDOT:PSS) doping. d) The UV-Vis transmittance spectra of PEDOT:PSS-doped transparent stacked graphene electrodes that vary in the number of graphene layers. Copyright 2015, WILEY-VCH; reprinted with permission.⁴⁹⁹ e) A schematic for a $\text{TiO}_2/\text{CH}_3\text{NH}_3\text{PbI}_3/\text{N-GF}$ structure layer, a f) cross-sectional scanning electron microscopy (SEM) image of $\text{TiO}_2/\text{CH}_3\text{NH}_3\text{PbI}_3/\text{N-GF}$ cells, and a g) surface SEM image of nitrogen-doped graphene framework (N-GF) on top of $\text{TiO}_2/\text{CH}_3\text{NH}_3\text{PbI}_3$. h) J-V curves of PSCs based on N-GF and GF BEs. Copyright 2018, The Royal Society of Chemistry; reprinted with permission.⁵⁰¹ i) Transport characterization of interface between graphene and perovskite. j) A schematic diagram of ohmic contact in single-layer graphene (SG)/perovskite with possible recombination. k) A schematic diagram of a Schottky junction in multi-layer graphene (MG)/perovskite with directional charge transfer. l) J-V curves for SG- and MG-based PSCs. Copyright 2015, WILEY-VCH; reprinted with permission.⁵⁰²

Hu *et al.* prepared a 3D honeycomb-like structured graphene (3DHG) by the reaction of potassium with CO_2 and employed it as a BE for HTM-free C-PSCs.⁵⁰³ They deposited the 3DHG on top of perovskite layer by doctor blading. The 3DHG exhibits excellent performance as a BE for an HTM-free C-PSC device, leading to a PCE of 10.06% (**Fig. 32a–f**). Shi *et al.* proposed an innovative modular architecture design for C-PSCs by stacking a semi-cell A and charge collector B together (**Fig. 32g–k**). The individual semi-cell A consisted of FTO/ SnO_2 /perovskite/spiro-OMeTAD and the charge collector B fabricated by spraying a carbon source in isopropyl alcohol onto an FTO substrate.⁵⁰⁴ They

compared commercial CB, graphite sheet (GS), and graphene. With graphene, there is sufficient interfacial contact of graphene with adjacent layers through deformation to fit the surface fluctuation of the adjacent functional layers. Thus, graphene is the best carbon BE for C-PSC in this experiment. Based on a graphene BE, a C-PSC device fabricated at low temperatures ($\leq 85^{\circ}\text{C}$) shows the best PCE (up to 18.65%). The prepared device also has excellent stability when exposed to humidity and heating. Moreover, it shows prominent structural flexibility with negligible degradation in efficiency even after repeated disassembly and reassembly (more than 500 times). **Table 11** shows the summary information of carbon-based perovskite solar cells with conventional device configuration and using graphene as a back electrode.

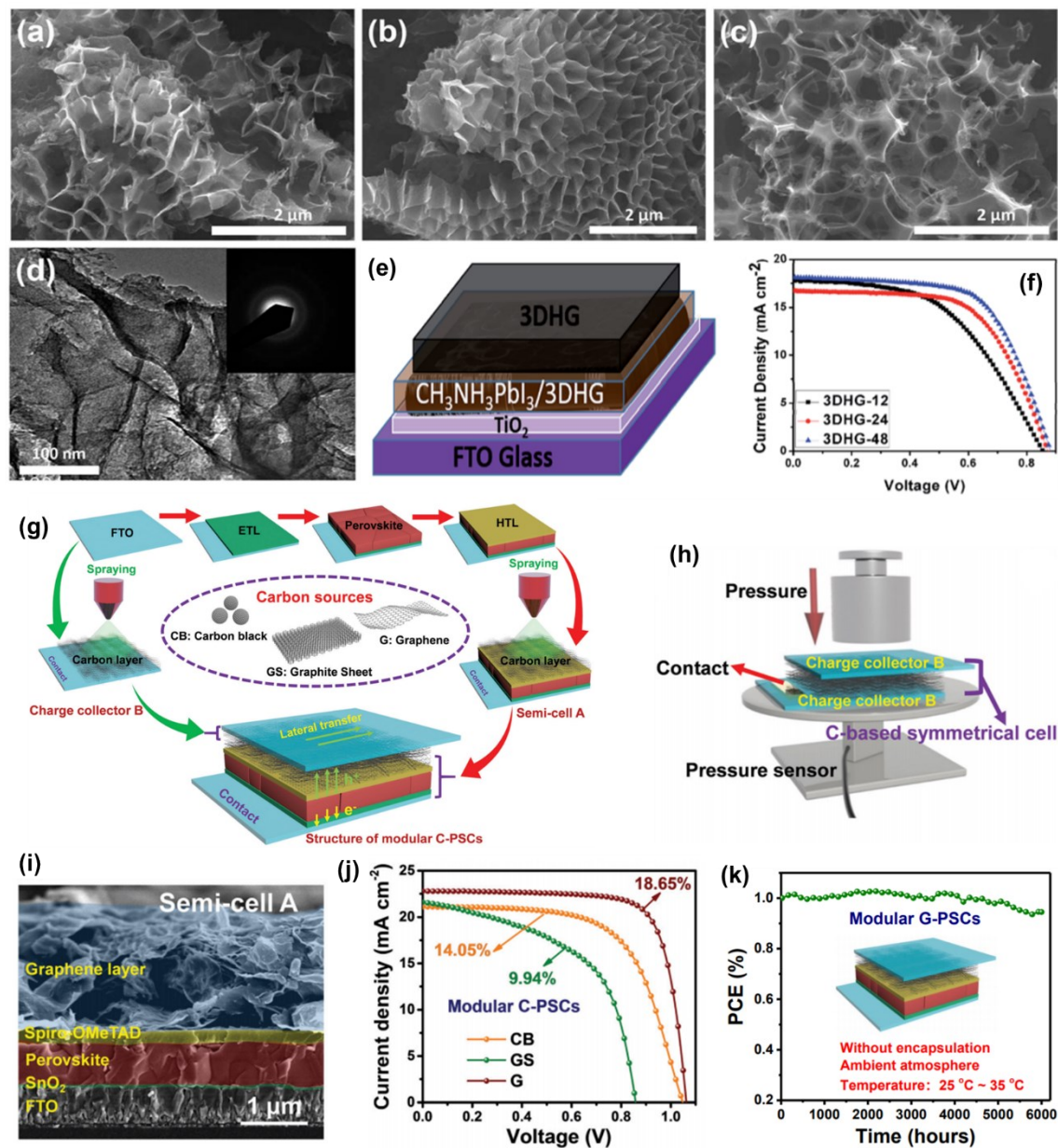


Fig. 32 Scanning electron microscopy (SEM) images of three-dimensional (3D) graphene sheets prepared using a) 12 h, b) 24 h, and c) 48 h reaction times. (d) A transmission electron microscopy (TEM) image of graphene sheets with the electron diffraction pattern. (e) A device with a 3D honeycomb-like structured graphene (3DHG) back electrode (BE). (f) J-V curves of carbon-based perovskite solar cells (C-PSCs) with different 3DHG BEs. Copyright 2017, The Royal Society of Chemistry; reprinted with permission.⁵⁰³ (g)

Schematic of the device fabrication process for the modular C-PSCs. The insets show the three carbon source materials. (h) A diagram for testing electromechanical contact properties for stacked symmetrical cell (by stacking two charge collectors B together). (i) Cross-sectional SEM image of graphene-based semi-cell A. (j) J-V curves measured under solar simulator AM 1.5 for modular C-PSCs based on different carbon sources. (k) Long-term stability of modular G-PSC without encapsulation stored in the ambient air (25–35°C and 40–80% humidity). Copyright 2019, The Royal Society of Chemistry; reprinted with permission.⁵⁰⁴

905 **Table 11** Summary of photovoltaic parameters on carbon-based perovskite solar cells with a conventional device configuration and using graphene
 906 as a back electrode.

Device configuration	Deposition method	Thermal treatment	V_{OC} (mV)	J_{SC} (mA cm ⁻²)	FF	η (%)	Ref.
FTO/c-TiO ₂ /mp-TiO ₂ /MAPbI ₃ /single-layer graphene	drop-casting	120°C/60 min	0.878	14.2	0.54	6.7%	502
FTO/c-TiO ₂ /mp-TiO ₂ /MAPbI ₃ /multi-layer graphene	drop-casting	120°C/60 min	0.943	16.7	0.73	11.5%	502
FTO/c-TiO ₂ /mp-TiO ₂ /MAPbI ₃ /three-dimensional mesoporous graphene	doctor-blading	80°C/240 min	0.78	18.00	0.58	8.18%	502
FTO/c-TiO ₂ /mp-TiO ₂ /MAPbI ₃ /N-GFs	drop-casting	100°C/5min	0.87	20.02	0.59	10.32	501
FTO/c-TiO ₂ /mp-TiO ₂ /MAPbI ₃ /GFs	drop-casting	100°C/5 min	0.86	18.69	0.56	8.98	501
FTO/SnO ₂ /Cs ₅ (MA _{0.17} FA _{0.83}) ₉₅ Pb(I _{0.83} Br _{0.17}) ₃ /doped spiro-OMeTAD/CB	Spraying & physical stacking	85°C/-	1.04	21.11	0.64	14.05	504
FTO/SnO ₂ /Cs ₅ (MA _{0.17} FA _{0.83}) ₉₅ Pb(I _{0.83} Br _{0.17}) ₃ /doped spiro-OMeTAD/graphene sheet	Spraying & physical stacking	85°C/-	0.84	21.52	0.55	9.94	504
FTO/SnO ₂ /Cs ₅ (MA _{0.17} FA _{0.83}) ₉₅ Pb(I _{0.83} Br _{0.17}) ₃ /doped spiro-OMeTAD/graphene	Spraying & physical stacking	85°C/-	1.05	22.78	0.78	18.65	504
FTO/c-TiO ₂ /MAPbI ₃ /3DHG-12	doctor-blade	120°C/60 min	0.87	17.79	0.50	7.71	503
FTO/c-TiO ₂ /MAPbI ₃ /3DHG-24	doctor-blade	120°C/60 min	0.87	16.75	0.62	9.01	503
FTO/c-TiO ₂ /MAPbI ₃ /3DHG-48	doctor-blade	120°C/60 min	0.89	18.11	0.63	10.06	503
FTO/c-TiO ₂ /MAPbI ₃ /spiro-OMeTAD/PEDOT:PSS/graphene (2 layer)	lamination process	65°C/-	0.96	19.17	0.672	12.37	499

FTO/c-TiO₂/MAPbI₃/spiro-OMeTAD/PEDOT:PSS/graphene (2
layer)

lamination process

65°C/°-

0.945

17.75

0.717

12.03*

⁴⁹⁹

907 Abbreviations: 3DHG, three-dimensional honeycomb-like structured graphene; FTO, fluorine-doped tin oxide; N-GF, nitrogen-doped graphene framework; PEDOT:SS,
908 poly(3,4-ethylenedioxythiophene) polystyrene sulfonate. *Indicates the efficiency from back side containing semi-transparent graphene electrode.

4. Conclusions and Outlooks: The CE/BE is a key component in DSSCs and PSCs and plays a critical role in the photovoltaic efficiency of the devices. The CE in DSSCs must possess high electrocatalytic ability, high conductivity, high electrochemical and mechanical stability, and good adhesivity with FTO. These properties may increase V_{OC} , J_{SC} , and FF and, consequently, the PCE of the DSSC. Pt satisfies most of the properties and has been widely employed as the standard CE in DSSCs; however, Pt is a costly and scarce noble metal, and it is thus difficult to use for large-scale applications. Carbon-based materials are promising substitutes for a Pt CE due to their low cost, scalability, and long-term stability. Numerous carbon-based materials, like CB, porous carbon, graphite, graphene, CNTs, and CNFs, have been successfully employed as CEs in DSSCs. The main disadvantages of carbon-based CEs are their low catalytic activity and conductivity compared to a Pt CE, as well as the large quantity required to obtain the desired catalytic activity. Therefore, researchers have attempted to increase the surface area and modify the surface of carbon-based materials through heteroatom doping (N, O, S, B, and P), as well as the incorporation of metals, metalloids, metal oxides, alloy, and polymer to achieve the anticipated performance of the devices.

Among the different types of amorphous carbons, N-doped mesoporous carbon is one of the best choices for a CE in DSSCs. A large surface area increases the catalytic active sites, while heteroatom doping redistributes the spin and charge density of the carbon network and creates highly efficient active sites, where reactant molecules interact more competently. Besides, different defect positions or heteroatoms in carbon substrate may be exploited as active sites for nucleation and growth of metal NPs, which can stabilize the deposited metal NPs that have a small size and narrow distribution.⁵⁴ Additionally, a doped carbon substrate enhances the surface roughness and oxygen vacancies of metal NPs and metal oxides, factors that also improve the catalytic activity of carbon composites.

Notably, functionalized graphene shows the best catalytic activity toward the iodine and cobalt reduction reaction in DSSCs. Topological defects and the dangling bonds located at the edge of sp^2 -hybridized carbon basal planes usually render high-energy sites and catalytic centers. Graphene nanoplatelet (GNP) composites, where edge sites are only catalytic sites, as CE in DSSCs, show the highest efficiency.^{214,218,505,506} Conversely, CNTs and CNFs show lower efficiency compared to functionalized graphene due to fewer active sites and limited capability for functionalization. Due to their higher flexibility and mechanical stability, CNTs and CNFs are the only choice for flexible, stretchable, or wire-shaped DSSCs.^{309,310,368} However, engineering specific catalytic sites in different carbon materials remains challenging. Thus, more investigations are required to develop a synthetic approach to create well-defined active sites in various carbon-based catalysts. Furthermore, researchers should consider the adjustability of designed CE materials for different electrolytes employed in DSSCs.

Unlike the CE in DSSCs, the catalytic activity of a carbon CE is not required for a BE in PSCs. Carbon materials are cost effective, highly stable, and have a Fermi energy level that is close to an Au electrode. Considering these aspects, carbon materials may be the ideal BE materials for PSCs. However, the efficiency of C- PSCs is relatively low, and there is a gap of over 25% comparing with metal BE-based PSCs, as summarized in **Tables 8–11** To minimize this large gap, the following aspects should be considered for developing efficient carbon BEs for C-PSCs. For mesoscopic triple layer type of C-PSCs: 1) a carbon BE must have good conductivity; 2) a carbon BE must have a suitable WF for a better energy level alignment of carbon-based materials with perovskite to ensure efficient hole selectively extraction; 3) the mesoporous carbon layer should have a suitable morphology to allow for efficient perovskite precursor filtration and interfacial contact in perovskite/carbon film; 4) there should be an efficient insulating layer with a wide bandgap, high porosity, and pore size >100 nm with ultra-film thickness.⁴²⁵ For conventional insulating layer-free C-PSCs: 1) a carbon BE must have

good conductivity; 2) the carbon BE must have a suitable WF for a better energy level alignment; 3) the processing solvent for carbon paste should not damage the perovskite film; and 4) a suitable organic and inorganic HTM should be inserted to enhance the HTM/carbon composite hole selectively extraction and collection. Furthermore, to improve heterogeneous contact at the carbon BE/perovskite or BE/HTM/perovskite interface, chemical binding, different solvent engineering, and fabrication processes should be investigated, all of which may decrease interfacial recombination. Finally, CNT and CVD graphene may be a potential transparent BE for a bifacial C-PSC^{490,499} or as a metal-free transparent electrode for a tandem solar cells that involve perovskite.⁵⁰⁰ In addition, a low-processing temperature for C-PSCs allows their application in flexible devices.

Conflicts of interest

The authors declare no conflicts of interest.

Acknowledgements

This work was supported by the Korean government (Ministry of Science, ICT, and Future Planning) through the Mid-career Researcher Program (NRF-2017R1A2A1A17069374). The Human Resources Program in Energy Technology of the Korea Institute of Energy Technology Evaluation and Planning (KETEP) granted financial resources from the Ministry of Trade, Industry & Energy, Republic of Korea (KETEP-20204030200070).

References

- 1 D. Spencer, *Ed. BP Stat. Rev. World Energy*, 2019, 1–69.
- 2 U.S. Energy Information Administration, *International Energy Outlook 2016*, 2016, vol. 0484(2016).
- 3 F. S. Fabiani Appavou, Adam Brown, Bärbel Epp, Duncan Gibb, Bozhil Kondev, Angus McCrone, Hannah E. Murdock, Evan Musolino, Lea Ranalder, Janet L. Sawin, Kristin Seyboth, Jonathan Skeen, *REN21 - 2019 Global Status Report*, 2019.
- 4 United Nations Development Programme, *World Energy Assessment. Energy and the challenge of Sustainability*, 2000.
- 5 V. Smil, *General Energetics: Energy in the Biosphere and Civilization*, John Wiley, New York, 1991.
- 6 D. M. Bagnall and M. Boreland, *Energy Policy*, 2008, **36**, 4390–4396.
- 7 A. Polman, M. Knight, E. C. Garnett, B. Ehrler and W. C. Sinke, *Science*, 2016, **352**, 4424–4424.
- 8 S. Sharma, Bulkesh Siwach, S. K. Ghoshal and D. Mohan, *Renew. Sustain. Energy Rev.*, 2017, **70**, 529–537.
- 9 M. A. Green, Y. Hishikawa, W. Warta, E. D. Dunlop, D. H. Levi, J. Hohl-Ebinger and A. W. H. Ho-Baillie, *Prog. Photovoltaics Res. Appl.*, 2017, **25**, 668–676.
- 10 M. A. Green, *Sol. Energy*, 2004, **76**, 3–8.
- 11 M. A. Green, *Prog. Photovoltaics Res. Appl.*, 2001, **9**, 123–135.
- 12 K. Yoshikawa, H. Kawasaki, W. Yoshida, T. Irie, K. Konishi, K. Nakano, T. Uto, D. Adachi, M. Kanematsu, H. Uzu and K. Yamamoto, *Nat. Energy*, 2017, **2**, 17032.

- 13 J. M. Ji, H. Zhou, Y. K. Eom, C. H. Kim and H. K. Kim, *Adv. Energy Mater.*, 2020, **10**, 1–12.
- 14 K. Kakiage, Y. Aoyama, T. Yano, K. Oya, J. Fujisawa and M. Hanaya, *Chem. Commun.*, 2015, **51**, 15894–15897.
- 15 M. A. Green, E. D. Dunlop, J. Hohl-Ebinger, M. Yoshita, N. Kopidakis and A. W. Y. Ho-Baillie, *Prog. Photovoltaics Res. Appl.*, 2020, **28**, 3–15.
- 16 Y. R. and K. H. Komiya R, Fukui A, Murofushi N, Koide N, *Tech. Dig.*, 2011, **21st Inter**, 2C-5O-08.
- 17 Q. Zhang, K. Park, J. Xi, D. Myers and G. Cao, *Adv. Energy Mater.*, 2011, **1**, 988–1001.
- 18 A. Hagfeldt, G. Boschloo, L. Sun, L. Kloo and H. Pettersson, *Chem. Rev.*, 2010, **110**, 6595–6663.
- 19 H. Michaels, M. Rinderle, R. Freitag, I. Benesperi, T. Edvinsson, R. Socher, A. Gagliardi and M. Freitag, *Chem. Sci.*, 2020, **11**, 2895–2906.
- 20 M. Freitag, J. Teuscher, Y. Saygili, X. Zhang, F. Giordano, P. Liska, J. Hua, S. M. Zakeeruddin, J. E. Moser, M. Grätzel and A. Hagfeldt, *Nat. Photonics*, 2017, **11**, 372–378.
- 21 S. Yoon, S. Tak, J. Kim, Y. Jun, K. Kang and J. Park, *Build. Environ.*, 2011, **46**, 1899–1904.
- 22 Y. Cao, Y. Liu, S. M. Zakeeruddin, A. Hagfeldt and M. Grätzel, *Joule*, 2018, **2**, 1108–1117.

- 23 File:Breakdown of the incoming solar energy.jpg - Wikipedia,
https://en.wikipedia.org/wiki/File:Breakdown_of_the_incoming_solar_energy.jpg,
(accessed 2 April 2020).
- 24 J. K. B. Bishop, *J. Geophys. Res.*, 1991, **96**, 839–858.
- 25 Best Research-Cell Efficiency Chart, <https://www.nrel.gov/pv/assets/pdfs/best-research-cell-efficiencies.20200406.pdf>, (accessed 13 July 2020).
- 26 M. Aftabuzzaman and H. K. Kim, *Emerg. Sol. Energy Mater.*, 2018,
DOI:10.5772/intechopen.75398.
- 27 M. Wu, M. Sun, H. Zhou, J. Y. Ma and T. Ma, *Adv. Funct. Mater.*, 2019, **1906451**, 1–
34.
- 28 L. Fagiolari and F. Bella, *Energy Environ. Sci.*, 2019, **12**, 3437–3472.
- 29 C. Zhou and S. Lin, *Sol. RRL*, 2020, **4**, 1900190.
- 30 J. Theerthagiri, A. R. Senthil, J. Madhavan and T. Maiyalagan, *ChemElectroChem*,
2015, **2**, 928–945.
- 31 G. Grancini, C. Roldán-Carmona, I. Zimmermann, E. Mosconi, X. Lee, D. Martineau,
S. Narbey, F. Oswald, F. De Angelis, M. Graetzel and M. K. Nazeeruddin, *Nat.*
Commun., 2017, **8**, 15684.
- 32 J. Wu, Y. Li, Q. Tang, G. Yue, J. Lin, M. Huang and L. Meng, *Sci. Rep.*, 2015, **4**,
4028.
- 33 T. N. Murakami and M. Grätzel, *Inorganica Chim. Acta*, 2008, **361**, 572–580.
- 34 J. B. Baxter, *J. Vac. Sci. Technol. A Vacuum, Surfaces, Film.*, 2012, **30**, 020801.
- 35 K. Li, Z. Yu, Y. Luo, D. Li and Q. Meng, *J. Mater. Sci. Technol.*, 2007, **23**, 577.

- 36 F. Fabregat-Santiago, J. Bisquert, E. Palomares, L. Otero, D. Kuang, S. M. Zakeeruddin and M. Grätzel, *J. Phys. Chem. C*, 2007, **111**, 6550–6560.
- 37 B. Zhang, D. Wang, Y. Hou, S. Yang, X. H. Yang, J. H. Zhong, J. Liu, H. F. Wang, P. Hu, H. J. Zhao and H. G. Yang, *Sci. Rep.*, 2013, **3**, 1836.
- 38 J. Wu, Y. Li, Q. Tang, G. Yue, J. Lin, M. Huang and L. Meng, , DOI:10.1038/srep04028.
- 39 K. Kalyanasundaram and M. Grätzel, *Coord. Chem. Rev.*, 1998, **77**, 347–414.
- 40 S. Thomas, T. G. Deepak, G. S. Anjusree, T. A. Arun, S. V Nair and A. S. Nair, *J. Mater. Chem. A*, 2014, **2**, 4474–4490.
- 41 L. Wang, M. Al-Mamun, P. Liu, Y. Wang, H. G. Yang, H. F. Wang and H. Zhao, *NPG Asia Mater.*, **7**, e226.
- 42 M. Seo, K. Fushimi, H. Takahashi, K. Aotsuka, K. Fujimoto, M. Nagayama, H. Konno, K. Kobayashi, K. Shimizu, D. Teranishi, J. Mater, K. Fujiwara, F. Takashima, M. Al-Odan, W. H. Smyrl, N. Papageorgiou, W. F. Maier and M. Grätzel, *J. Electrochem. Soc.*, 1997, **144**, 257–1349.
- 43 N. Papageorgiou, *Coord. Chem. Rev.*, 2004, **248**, 1421–1446.
- 44 G. Veerappan, K. Bojan and S. W. Rhee, *ACS Appl. Mater. Interfaces*, 2011, **3**, 857–862.
- 45 Y. S. Wei, Q. Q. Jin and T. Z. Ren, *Solid. State. Electron.*, 2011, **63**, 76–82.
- 46 L. Kavan, J. H. Yum and M. Grätzel, *Nano Lett.*, 2011, **11**, 5501–5506.
- 47 L. Kavan, J. H. Yum, M. K. Nazeeruddin and M. Grätzel, *ACS Nano*, 2011, **5**, 9171–9178.

- 48 K. Gao, B. Wang, L. Tao, B. V. Cuning, Z. Zhang, S. Wang, R. S. Ruoff and L. Qu, *Adv. Mater.*, 2019, **31**, 1–11.
- 49 Y. Xu, M. Kraft and R. Xu, *Chem. Soc. Rev.*, 2016, **45**, 3039–3052.
- 50 W. C. Oh and Y. Areerob, *ACS Appl. Mater. Interfaces*, 2019, **11**, 38859–38867.
- 51 M. S. Mahmoud, M. Motlak and A. M. Barakat, *Catalysts*, 2019, **9**, 139.
- 52 C. K. Kim, H. Zhou, T. Kowalewski, K. Matyjaszewski and H. K. Kim, *ACS Appl. Mater. Interfaces*, 2019, **11**, 2093–2102.
- 53 W. Yang, Z. Li, X. Xu, L. Hou, Y. Tang, B. Deng, F. Yang, Y. Wang and Y. Li, *Chem. Eng. J.*, 2018, **349**, 782–790.
- 54 Y. Cao, S. Mao, M. Li, Y. Chen and Y. Wang, *ACS Catal.*, 2017, **7**, 8090–8112.
- 55 File:Eight Allotropes of Carbon.png - Wikipedia,
https://en.wikipedia.org/wiki/File:Eight_Allotropes_of_Carbon.png, (accessed day month year).
- 56 J. Lim, S. Y. Ryu, J. Kim and Y. Jun, *Nanoscale Res. Lett.*, 2013, **8**, 227.
- 57 A. Kay and M. Grätzel, *Sol. Energy Mater. Sol. Cells*, 1996, **44**, 99–117.
- 58 T. N. Murakami, S. Ito, Q. Wang, M. K. Nazeeruddin, T. Bessho, I. Cesar, P. Liska, R. Humphry-Baker, P. Comte, P. Péchy and M. Grätzel, *J. Electrochem. Soc.*, 2006, **153**, A2255.
- 59 C.-S. Wu, T.-W. Chang, H. Teng and Y.-L. Lee, *Energy*, 2016, **115**, 513–518.
- 60 I. P. Liu, Y. C. Hou, C. W. Li and Y. L. Lee, *J. Mater. Chem. A*, 2017, **5**, 240–249.
- 61 M. Bagavathi, A. Ramar and R. Saraswathi, *Ceram. Int.*, 2016, **42**, 13190–13198.

- 62 C.-T. Li, C.-T. Lee, S.-R. Li, C.-P. Lee, I.-T. Chiu, R. Vittal, N.-L. Wu, S.-S. Sun and K.-C. Ho, *J. Power Sources*, 2016, **302**, 155–163.
- 63 C.-S. Wu, S. Venkatesan, T.-W. Chang and Y.-L. Lee, *J. Solid State Electrochem.*, 2018, **22**, 255–262.
- 64 B. C. Nath, K. J. Mohan, R. Barua, G. A. Ahmed and S. K. Dolui, *J. Photochem. Photobiol. A Chem.*, 2017, **348**, 33–40.
- 65 A. Bora, K. Mohan, P. Phukan and S. K. Dolui, *Electrochim. Acta*, 2018, **259**, 233–244.
- 66 J. Zhang, H. Long, S. G. Miralles, J. Bisquert, F. Fabregat-Santiago and M. Zhang, *Phys. Chem. Chem. Phys.*, 2012, **14**, 7131.
- 67 G. Kang, J. Choi and T. Park, *Sci. Rep.*, 2016, **6**, 22987.
- 68 C. S. Wu, S. Venkatesan, T. W. Chang and Y. L. Lee, *J. Solid State Electrochem.*, 2018, **22**, 255–262.
- 69 W. R. Lee, Y. S. Jun, J. Park and G. D. Stucky, *J. Mater. Chem. A*, 2015, **3**, 24232–24236.
- 70 M. Li, C. Yu, C. Hu, C. Zhao, M. Zhang, Y. Ding, X. Wang and J. Qiu, *Green Chem.*, 2018, **20**, 250–254.
- 71 S. Q. Guo, L. C. Wang, C. G. Zhang, G. C. Qi, B. C. Gu, L. Liu and Z. H. Yuan, *Nanoscale*, 2017, **9**, 6837–6845.
- 72 J. Li, X. Li, T. Wang, P. He, F. Li, W. Chen and E. Wang, *ACS Appl. Energy Mater.*, 2019, **2**, 5824–5834.

- 73 C. F. Lin, Y. C. Chou, J. F. Haung, P. H. Chen, H. C. Han, K. Y. Chiu and Y. O. Su, *Jpn. J. Appl. Phys.*, 2016, **55**, 1–6.
- 74 I.-P. Liu, Y.-C. Hou, C.-W. Li and Y.-L. Lee, *J. Mater. Chem. A*, 2017, **5**, 240–249.
- 75 W. Ahmad, L. Chu, M. R. Al-Bahrani, Z. Yang, S. Wang, L. Li and Y. Gao, *RSC Adv.*, 2015, **5**, 35635–35642.
- 76 G. Wang, J. Zhang and S. Hou, *Mater. Res. Bull.*, 2016, **76**, 454–458.
- 77 Y. Wang, N. Fu, P. Ma, Y. Fang, L. Peng, X. Zhou and Y. Lin, *Appl. Surf. Sci.*, 2017, **419**, 670–677.
- 78 A. Bora, K. Mohan, P. Phukan and S. K. Dolui, *Electrochim. Acta*, 2018, **259**, 233–244.
- 79 A. S. A. Ahmed, W. Xiang, A. Gu, X. Hu, I. A. Saana and X. Zhao, *New J. Chem.*, 2018, **42**, 11715–11723.
- 80 M. U. Rahman, F. Xie, X. Sun and M. Wei, *J. Electroanal. Chem.*, 2019, **848**, 113317.
- 81 H. Jing, D. Wu, S. Liang, X. Song, Y. An, C. Hao and Y. Shi, *J. Energy Chem.*, 2019, **31**, 89–94.
- 82 K. D. M. S. P. K. Kumarasinghe, G. R. A. Kumara, R. M. G. Rajapakse, D. N. Liyanage and K. Tennakone, *Org. Electron.*, 2019, **71**, 93–97.
- 83 K. Lee, S. Cho, M. Kim, J. Kim, J. Ryu, K. Y. Shin and J. Jang, *J. Mater. Chem. A*, 2015, **3**, 19018–19026.
- 84 C. T. Li, Y. F. Lin, I. T. Chiu and K. C. Ho, *J. Mater. Chem. A*, 2015, **3**, 24479–24486.
- 85 I. T. Chiu, C. T. Li, C. P. Lee, P. Y. Chen, Y. H. Tseng, R. Vittal and K. C. Ho, *Nano Energy*, 2016, **22**, 594–606.

- 86 X. Cui, Z. Xie and Y. Wang, *Nanoscale*, 2016, **8**, 11984–11992.
- 87 C. Zhu, F. Xu, J. Chen, H. Min, H. Dong, L. Tong, K. Qasim, S. Li and L. Sun, *J. Power Sources*, 2016, **303**, 159–167.
- 88 P. Sun, M. Zhang, C. Ai, Z. Wu, S. Lu, X. Zhang, N. Huang, Y. Sun and X. Sun, *J. Power Sources*, 2016, **319**, 219–226.
- 89 C. Xiang, T. Lv, C. A. Okonkwo, M. Zhang, L. Jia and W. Xia, *J. Electrochem. Soc.*, 2017, **164**, H203–H210.
- 90 Y. Duan, N. Fu, S. Li, X. Yang, J. Zheng, Y. Lin and F. Pan, *J. Mater. Chem. A*, 2017, **5**, 6884–6892.
- 91 W. Zhu, Y. Zhao, J. Duan, Y. Duan, Q. Tang and B. He, *Chem. Commun.*, 2017, **53**, 9894–9897.
- 92 C. Gao, H. Wang, Q. Han, Z. Hu and M. Wu, *Electrochim. Acta*, 2018, **264**, 312–318.
- 93 Y. Ding, N. Huang, S. Yan, R. Peng, P. Sun, X. Sun and C. Huang, *J. Alloys Compd.*, 2018, **767**, 848–855.
- 94 Y. Zhang, Y. Zhao, J. Duan and Q. Tang, *Electrochim. Acta*, 2018, **261**, 588–595.
- 95 Y. Di, S. Jia, N. Li, C. Hao, H. Zhang and S. Hu, *Org. Electron.*, 2020, **76**, 105395.
- 96 M. Chen, L.-L. Shao, X. Qian, L. Liu, T.-Z. Ren and Z.-Y. Yuan, *Chem. Eng. J.*, 2014, **256**, 23–31.
- 97 Q. W. Jiang, G. R. Li, F. Wang and X. P. Gao, *Electrochem. Commun.*, 2010, **12**, 924–927.
- 98 H. K. Kim, M. Aftabuzzaman, C. K. Kim, T. Kowalewski and K. Matyjaszewski, *J. Mater. Chem. A*, 2019, **7**, 20208–20222.

- 99 Z. Huang, X. Liu, K. Li, D. Li, Y. Luo, H. Li, W. Song, L. Q. Chen and Q. Meng, *Electrochem. commun.*, 2007, **9**, 596–598.
- 100 K. Imoto, K. Takahashi, T. Yamaguchi, T. Komura, J. I. Nakamura and K. Murata, *Sol. Energy Mater. Sol. Cells*, 2003, **79**, 459–469.
- 101 B. Fang, S. Q. Fan, J. H. Kim, M. S. Kim, M. Kim, N. K. Chaudhari, J. Ko and J. S. Yu, *Langmuir*, 2010, **26**, 11238–11243.
- 102 E. Ramasamy and J. Lee, *Chem. Commun.*, 2010, **46**, 2136.
- 103 B. Zhao, H. Huang, P. Jiang, H. Zhao, X. Huang, P. Shen, D. Wu, R. Fu and S. Tan, *J. Phys. Chem. C*, 2011, **115**, 22615–22621.
- 104 L. L. Shao, M. Chen and Z. Y. Yuan, *J. Power Sources*, 2014, **272**, 1091–1099.
- 105 D. Y. Chung, Y. J. Son, J. M. Yoo, J. S. Kang, C.-Y. Ahn, S. Park and Y.-E. Sung, *ACS Appl. Mater. Interfaces*, 2017, **9**, 41303–41313.
- 106 C. Wang, F. Meng, M. Wu, X. Lin, T. Wang, J. Qiu and T. Ma, *Phys. Chem. Chem. Phys.*, 2013, **15**, 14182.
- 107 R. Gokhale, S. Agarkar, J. Debgupta, D. Shinde, B. Lefez, A. Banerjee, J. Jog, M. More, B. Hannoyer and S. Ogale, *Nanoscale*, 2012, **4**, 6730.
- 108 A. S. Mestre, E. Tyszko, M. A. Andrade, M. Galhetas, C. Freire and A. P. Carvalho, *RSC Adv.*, 2015, **5**, 19696–19707.
- 109 H. Marsh and F. Rodríguez-Reinoso, *Activated Carbon*, Elsevier Science, Amsterdam, 2006.
- 110 E. Raymundo-Piñero, P. Azañes, T. Cacciaguerra, D. Cazorla-Amorós, A. Linares-Solano and F. Béguin, *Carbon N. Y.*, 2005, **43**, 786–795.

- 111 A. J. Romero-Anaya, M. Ouzzine, M. A. Lillo-Ródenas and A. Linares-Solano, *Carbon N. Y.*, 2014, **68**, 296–307.
- 112 X. Liu, *Nano Adv.*, 2016, **1**, 90–103.
- 113 S. Fajardo, García-Galvan, F. R., V. Barranco, J. C. Galvan and S. F. Batlle, *Intech*, 2016, **i**, 13.
- 114 K. Yajima, H. Matsuura and F. Tsukihashi, *ISIJ Int.*, 2009, **49**, 10–16.
- 115 M. Sevilla and A. B. Fuertes, *ChemSusChem*, 2016, **9**, 1880–1888.
- 116 J. Wang and S. Kaskel, *J. Mater. Chem.*, 2012, **22**, 23710.
- 117 X. Liu and M. Antonietti, *Adv. Mater.*, 2013, **25**, 6284–6290.
- 118 D. Y. Chung, Y. J. Son, J. M. Yoo, J. S. Kang, C. Y. Ahn, S. Park and Y. E. Sung, *ACS Appl. Mater. Interfaces*, 2017, **9**, 41303–41313.
- 119 C. K. Kim, I. T. Choi, S. H. Kang and H. K. Kim, *RSC Adv.*, 2017, **7**, 35565–35574.
- 120 G. Hasegawa, T. Deguchi, K. Kanamori, Y. Kobayashi, H. Kageyama, T. Abe and K. Nakanishi, *Chem. Mater.*, 2015, **27**, 4703–4712.
- 121 L. Wang, Z. Gao, J. Chang, X. Liu, D. Wu, F. Xu, Y. Guo and K. Jiang, *ACS Appl. Mater. Interfaces*, 2015, **7**, 20234–20244.
- 122 C. Wang, S. Yun, Q. Fan, Z. Wang, Y. Zhang, F. Han, Y. Si and A. Hagfeldt, *J. Mater. Chem. A*, 2019, **7**, 14864–14875.
- 123 M. Baro, Jaidev and S. Ramaprabhu, *RSC Adv.*, 2016, **6**, 96109–96120.
- 124 G. Nagaraju, J. H. Lim, S. M. Cha and J. S. Yu, *J. Alloys Compd.*, 2017, **693**, 1297–1304.

- 125 G. Wang, C. Yan, S. Hou and W. Zhang, *Mater. Sci. Semicond. Process.*, 2017, **63**, 190–195.
- 126 P. Ma, W. Lu, X. Yan, W. Li, L. Li, Y. Fang, X. Yin, Z. Liu and Y. Lin, *RSC Adv.*, 2018, **8**, 18427–18433.
- 127 S. M. Cha, G. Nagaraju, S. C. Sekhar, L. K. Bharat and J. S. Yu, *J. Colloid Interface Sci.*, 2018, **513**, 843–851.
- 128 M. Baro, J. Harjwani and S. Ramaprabhu, *IEEE J. Photovoltaics*, 2019, **9**, 700–709.
- 129 C. Wang, S. Yun, H. Xu, Z. Wang, F. Han, Y. Zhang, Y. Si and M. Sun, *Ceram. Int.*, 2019, **46**, 3292–3303.
- 130 M. Baro, Jaidev and S. Ramaprabhu, *Appl. Surf. Sci.*, 2020, **503**, 144069.
- 131 G. Wang, W. Dong, P. Ma, C. Yan, W. Zhang and J. Liu, *Electrochim. Acta*, 2018, **290**, 273–281.
- 132 L. Wang, Z. Gao, J. Chang, X. Liu, D. Wu, F. Xu, Y. Guo and K. Jiang, *ACS Appl. Mater. Interfaces*, 2015, **7**, 20234–20244.
- 133 A. A. Memon, A. A. Arbab, I. A. Sahito, N. Mengal, K. C. Sun, M. B. Qadir, Y. S. Choi and S. H. Jeong, *Electrochim. Acta*, 2017, **234**, 53–62.
- 134 A. A. Memon, A. A. Arbab, I. A. Sahito, K. C. Sun, N. Mengal and S. H. Jeong, *Sol. Energy*, 2017, **150**, 521–531.
- 135 Y. Zhang, S. Yun, C. Wang, Z. Wang, F. Han and Y. Si, *J. Power Sources*, 2019, **423**, 339–348.
- 136 K. Wu, Z. Liu, M. Wu, B. Ruan, R. Wu, H. Zhou and M. Wu, *J. Electroanal. Chem.*, 2019, **835**, 150–155.

- 137 S. Yun, X. Zhou, Y. Zhang, C. Wang and Y. Hou, *Electrochim. Acta*, 2019, **309**, 371–381.
- 138 L. Li, C. L. Wang, J. Y. Liao and A. Manthiram, *J. Power Sources*, 2015, **300**, 254–260.
- 139 M. Wu, Y. nan Lin, H. Guo, W. Li, Y. Wang and X. Lin, *Nano Energy*, 2015, **11**, 540–549.
- 140 X. Liu, C. Giordano and M. Antonietti, *Small*, 2014, **10**, 193–200.
- 141 Z. Sun, W. Wang, J. Zhang, G. Wang, K. Wang, X. Liu, G. Ni and Y. Jiang, *New J. Chem.*, 2019, **43**, 1864–1873.
- 142 T. Morishita, T. Tsumura, M. Toyoda, J. Przepiórski, A. W. Morawski, H. Konno and M. Inagaki, *Carbon N. Y.*, 2010, **48**, 2690–2707.
- 143 C. Zhu and T. Akiyama, *Green Chem.*, 2016, **18**, 2106–2114.
- 144 Z. Li, W. Yang, X. Xu, Y. Tang, Z. Zeng, F. Yang, L. Zhang, G. Ning, C. Xu and Y. Li, *J. Power Sources*, 2016, **327**, 289–296.
- 145 J. Li, Q. Jiang, L. Wei, L. Zhong and X. Wang, *J. Mater. Chem. A*, 2020, **8**, 1469–1479.
- 146 L. Kong, M. Liu, Z. Diao, D. Chen, X. Chang and Y. Xiong, *Sci. Rep.*, 2016, **6**, 1–9.
- 147 J. Wang, C. Zhang, Y. Shen, Z. Zhou, J. Yu, Y. Li, W. Wei, S. Liu and Y. Zhang, *J. Mater. Chem. A*, 2015, **3**, 5126–5131.
- 148 N. Xiao, J. Song, Y. Wang, C. Liu, Y. Zhou, Z. Liu, M. Li and J. Qiu, *Carbon N. Y.*, 2018, **128**, 201–204.

- 149 M. Chen, L.-L. Shao, X. Qian, T.-Z. Ren and Z.-Y. Yuan, *J. Mater. Chem. C*, 2014, **2**, 10312–10321.
- 150 M. J. Ju, I. T. Choi, M. Zhong, K. Lim, J. Ko, J. Mohin, M. Lamson, T. Kowalewski, K. Matyjaszewski and H. K. Kim, *J. Mater. Chem. A*, 2015, **3**, 4413–4419.
- 151 L. Li, H. Sui, W. Zhang, X. Li, K. Yang, A. Hagfeldt and M. Wu, *J. Mater. Chem. C*, 2016, **4**, 6778–6783.
- 152 M. H. Selamat and A. H. Ahmad, 2016, **10**, 2–4.
- 153 L.-L. Shao, M. Chen, T.-Z. Ren and Z.-Y. Yuan, *J. Power Sources*, 2015, **274**, 791–798.
- 154 S.-H. Park, H.-R. Jung, B.-K. Kim and W.-J. Lee, *J. Photochem. Photobiol. A Chem.*, 2012, **246**, 45–49.
- 155 W. Li, P. Ma, F. Chen, R. Xu, Z. Cheng, X. Yin, Y. Lin and L. Wang, *Inorg. Chem. Front.*, 2019, **6**, 2550–2557.
- 156 M. Aftabuzzaman, C. K. Kim, H. Zhou and H. K. Kim, *Nanoscale*, 2020, **12**, 1602–1616.
- 157 C. K. Kim, J. M. Ji, H. Zhou, C. Lu and H. K. Kim, *Nanomaterials*, , DOI:10.3390/nano10010029.
- 158 M. Chen, L. L. Shao, Y. Xia, Z. Y. Huang, D. L. Xu, Z. W. Zhang, Z. X. Chang and W. J. Pei, *ACS Appl. Mater. Interfaces*, 2016, **8**, 26030–26040.
- 159 W. Yang, X. Ma, X. Xu, Y. Li, S. I. Raj, G. Ning, A. Wang and S. Chen, *J. Power Sources*, 2015, **282**, 228–234.

- 160 M. J. Ju, I. T. Choi, M. Zhong, K. Lim, J. Ko, J. Mohin, M. Lamson, T. Kowalewski, K. Matyjaszewski and H. K. Kim, *J. Mater. Chem. A*, 2015, **3**, 4413–4419.
- 161 C. L. Wang, J. Y. Liao, S. H. Chung and A. Manthiram, *Adv. Energy Mater.*, 2015, **5**, 1–4.
- 162 G. Wang, J. Zhang, S. Kuang and S. Zhuo, *Mater. Sci. Semicond. Process.*, 2015, **38**, 234–239.
- 163 X. Li, R. Chen, L. Li, S. Wang, W. Zhang, K. Wu, W. Li and M. Wu, *Electrochim. Acta*, 2016, **200**, 168–173.
- 164 X. Sun, Y. Li, J. Dou, D. Shen and M. Wei, *J. Power Sources*, 2016, **322**, 93–98.
- 165 H. Jing, X. Song, S. Ren, Y. Shi, Y. An, Y. Yang, M. Feng, S. Ma and C. Hao, *Electrochim. Acta*, 2016, **213**, 252–259.
- 166 Y. Zhu, H. Guo, H. Zheng, Y. nan Lin, C. Gao, Q. Han and M. Wu, *Nano Energy*, 2016, **21**, 1–18.
- 167 S. Y. Bae, D. H. Kweon, J. Mahmood, M. J. Kim, S. Y. Yu, S. M. Jung, S. H. Shin, M. J. Ju and J. B. Baek, *Nano Energy*, 2017, **34**, 533–540.
- 168 Q. Han, H. Wang, Y. Liu, Y. Yan and M. Wu, *J. Colloid Interface Sci.*, 2017, **506**, 518–523.
- 169 N. Xiao, J. Song, Y. Wang, C. Liu, Y. Zhou, Z. Liu, M. Li and J. Qiu, *Carbon N. Y.*, 2018, **128**, 201–204.
- 170 H. Jing, Y. Shi, D. Wu, S. Liang, X. Song, Y. An and C. Hao, *Electrochim. Acta*, 2018, **281**, 646–653.

- 171 X. Meng, C. Yu, X. Zhang, L. Huang, M. Rager, J. Hong, J. Qiu and Z. Lin, *Nano Energy*, 2018, **54**, 138–147.
- 172 Y. J. Huang, Y. J. Lin, H. J. Chien, Y. F. Lin and K. C. Ho, *Nanoscale*, 2019, **11**, 12507–12516.
- 173 H. Guo, Q. Han, C. Gao, H. Zheng, Y. Zhu and M. Wu, *J. Power Sources*, 2016, **332**, 399–405.
- 174 P. Hasin, V. Amornkitbamrung and N. Chanlek, *J. Catal.*, 2017, **351**, 19–32.
- 175 H. Li, Q. Xie, J. Li, Z. Xie and H. Tang, *J. Alloys Compd.*, 2018, **742**, 641–647.
- 176 W. Wang, J. Yao, X. Zuo and G. Li, *Mater. Lett.*, 2018, **227**, 172–175.
- 177 S. Lu, S. Jin, Y. Meng, J. Chen, W. Wang, J. Yao and G. Li, *Mater. Lett.*, 2019, **250**, 84–87.
- 178 J. Yao, W. Wang, X. Zuo, Q. Yang, M. W. Khan, M. Wu, H. Tang, S. Jin and G. Li, *Appl. Catal. B Environ.*, 2019, **256**, 117857.
- 179 J. Chang, X. Song, C. Yu, H. Huang, J. Hong, Y. Ding, H. Huang, J. Yu, X. Tan, Z. Zhao and J. Qiu, *Nano Energy*, 2020, **69**, 104377.
- 180 K. S. Novoselov, S. V. Morozov, D. Jiang, Y. Zhang, S. V. Dubonos, I. V. Grigorieva, A. A. Firsov and A. K. Geim, *Science*, 2004, **306**, 666–669.
- 181 X. Du, I. Skachko, A. Barker and E. Y. Andrei, *Nat. Nanotechnol.*, 2008, **3**, 491–495.
- 182 Y. Zhu, S. Murali, W. Cai, X. Li, J. W. Suk, J. R. Potts and R. S. Ruoff, *Adv. Mater.*, 2010, **22**, 3906–3924.
- 183 A. Peigney, C. Laurent, E. Flahaut, R. R. Bacsa and A. Rousset, *Carbon N. Y.*, 2001, **39**, 507–514.

- 184 M. J. McAllister, J. L. Li, D. H. Adamson, H. C. Schniepp, A. A. Abdala, J. Liu, M. Herrera-Alonso, D. L. Milius, R. Car, R. K. Prud'homme and I. A. Aksay, *Chem. Mater.*, 2007, **19**, 4396–4404.
- 185 S. Stankovich, D. A. Dikin, G. H. B. Dommett, K. M. Kohlhaas, E. J. Zimney, E. A. Stach, R. D. Piner, S. T. Nguyen and R. S. Ruoff, *Nature*, 2006, **442**, 282–286.
- 186 C. Lee, X. Wei, J. W. Kysar and J. Hone, *Science*, 2008, **321**, 385–388.
- 187 R. R. Nair, P. Blake, A. N. Grigorenko, K. S. Novoselov, T. J. Booth, T. Stauber, N. M. R. Peres and A. K. Geim, *Science*, 2008, **320**, 1308–1308.
- 188 C. Te Hsieh, B. H. Yang and Y. F. Chen, *Diam. Relat. Mater.*, 2012, **27–28**, 68–75.
- 189 H. Kim, H. Choi, S. Hwang, Y. Kim and M. Jeon, *Nanoscale Res. Lett.*, 2012, **7**, 53.
- 190 A. Bianco, H. M. Cheng, T. Enoki, Y. Gogotsi, R. H. Hurt, N. Koratkar, T. Kyotani, M. Monthieux, C. R. Park, J. M. D. Tascon and J. Zhang, *Carbon N. Y.*, 2013, **65**, 1–6.
- 191 C. Berger, X. Wu, N. Brown, C. Naud, X. Li, Z. Song, D. Mayou, T. Li, J. Hass, A. Marchenkov, E. H. Conrad, P. N. First and W. a. De Heer, *Science*, 2006, **312**, 1191–1196.
- 192 C. Huang, C. Li and G. Shi, *Energy Environ. Sci.*, 2012, **5**, 8848–8868.
- 193 A. K. Geim and K. S. Novoselov, *Nat. Mater.*, 2007, **6**, 183–191.
- 194 Y.-Y. Li, C.-T. Li, M.-H. Yeh, K.-C. Huang, P.-W. Chen, R. Vittal and K.-C. Ho, *Electrochim. Acta*, 2015, **179**, 211–219.
- 195 S. S. Nemala, P. Kartikay, S. Prathapani, H. L. M. Bohm, P. Bhargava, S. Bohm and S. Mallick, *J. Colloid Interface Sci.*, 2017, **499**, 9–16.

- 196 W. Yang, X. Xu, Y. Gao, Z. Li, C. Li, W. Wang, Y. Chen, G. Ning, L. Zhang, F. Yang, S. Chen, A. Wang, J. Kong and Y. Li, *Nanoscale*, 2016, **8**, 13059–13066.
- 197 Y. Hernandez, V. Nicolosi, M. Lotya, F. M. Blighe, Z. Sun, S. De, I. T. McGovern, B. Holland, M. Byrne, Y. K. Gun'Ko, J. J. Boland, P. Niraj, G. Duesberg, S. Krishnamurthy, R. Goodhue, J. Hutchison, V. Scardaci, A. C. Ferrari and J. N. Coleman, *Nat. Nanotechnol.*, 2008, **3**, 563–568.
- 198 Y.-M. Lin, C. Dimitrakopoulos, K. A. Jenkins, D. B. Farmer, H.-Y. Chiu, A. Grill and P. Avouris, *Science*, 2010, **327**, 662–662.
- 199 Q. Yu, L. A. Jauregui, W. Wu, R. Colby, J. Tian, Z. Su, H. Cao, Z. Liu, D. Pandey, D. Wei, T. F. Chung, P. Peng, N. P. Guisinger, E. A. Stach, J. Bao, S.-S. Pei and Y. P. Chen, *Nat. Mater.*, 2011, **10**, 443–449.
- 200 D. C. Marcano, D. V. Kosynkin, J. M. Berlin, A. Sinitskii, Z. Sun, A. Slesarev, L. B. Alemany, W. Lu and J. M. Tour, *ACS Nano*, 2010, **4**, 4806–4814.
- 201 W. S. Hummers and R. E. Offeman, *J. Am. Chem. Soc.*, 1958, **80**, 1339.
- 202 Y. Xu, H. Bai, G. Lu, C. Li and G. Shi, *J. Am. Chem. Soc.*, 2008, **130**, 5856–5857.
- 203 C. Punckt, J. D. Roy-mayhew, D. J. Bozym, C. Punckt and I. A. Aksay, *ACS Nano*, 2010, **4**, 6203–6211.
- 204 D. Deng, X. Pan, L. Yu, Y. Cui, Y. Jiang, J. Qi, W. X. Li, Q. Fu, X. Ma, Q. Xue, G. Sun and X. Bao, *Chem. Mater.*, 2011, **23**, 1188–1193.
- 205 C. A. Tseng, C. P. Lee, Y. J. Huang, H. W. Pang, K. C. Ho and Y. T. Chen, *Mater. Today Energy*, 2018, **8**, 15–21.
- 206 C. Yu, Z. Liu, X. Meng, B. Lu, D. Cui and J. Qiu, *Nanoscale*, 2016, **8**, 17458–17464.

- 207 H. M. Kim, I.-Y. Jeon, I. T. Choi, S. H. Kang, S.-H. Shin, H. Y. Jeong, M. J. Ju, J.-B. Baek and H. K. Kim, *J. Mater. Chem. A*, 2016, **4**, 9029–9037.
- 208 W. Yang, X. Xu, L. Hou, X. Ma, F. Yang, Y. Wang and Y. Li, *J. Mater. Chem. A*, 2017, **5**, 5952–5960.
- 209 Y. C. Chang, C. A. Tseng, C. P. Lee, S. B. Ann, Y. J. Huang, K. C. Ho and Y. T. Chen, *J. Power Sources*, 2020, **449**, 227470.
- 210 D. Wu, C. Zhu, Y. Shi, H. Jing, J. Hu, X. Song, D. Si, S. Liang and C. Hao, *ACS Sustain. Chem. Eng.*, 2019, **7**, 1137–1145.
- 211 A. Rani, K. Chung, J. Kwon, S. J. Kim, Y. H. Jang, Y. J. Jang, L. N. Quan, M. Yoon, J. H. Park and D. H. Kim, *ACS Appl. Mater. Interfaces*, 2016, **8**, 11488–11498.
- 212 Z. Yu, Y. Bai, Y. Wang, Y. Liu, Y. Zhao, Y. Liu and K. Sun, *Chem. Eng. J.*, 2017, **311**, 302–309.
- 213 K. Y. Lin, M. T. Nguyen, K. Waki and J. C. Jiang, *J. Phys. Chem. C*, 2018, **122**, 26385–26392.
- 214 C. K. Kim, H. M. Kim, M. Aftabuzzaman, I. Y. Jeon, S. H. Kang, Y. K. Eom, J. B. Baek and H. K. Kim, *Mater. Today Energy*, 2018, **9**, 67–73.
- 215 M. J. Ju, J. C. Kim, H. J. Choi, I. T. Choi, S. G. Kim, K. Lim, J. Ko, J. J. Lee, I. Y. Jeon, J. B. Baek and H. K. Kim, *ACS Nano*, 2013, **7**, 5243–5250.
- 216 I.-Y. Jeon, H.-J. Choi, M. J. Ju, I. T. Choi, K. Lim, J. Ko, H. K. Kim, J. C. Kim, J.-J. Lee, D. Shin, S.-M. Jung, J.-M. Seo, M.-J. Kim, N. Park, L. Dai and J.-B. Baek, *Sci. Rep.*, 2013, **3**, 2260.

- 217 I. Y. Jeon, H. M. Kim, D. H. Kweon, S. M. Jung, J. M. Seo, S. H. Shin, I. T. Choi, Y. K. Eom, S. H. Kang, H. K. Kim, M. J. Ju and J. B. Baek, *Nano Energy*, 2016, **30**, 867–876.
- 218 M. J. Ju, I.-Y. Jeon, H. M. Kim, J. I. Choi, S.-M. Jung, J.-M. Seo, I. T. Choi, S. H. Kang, H. S. Kim, M. J. Noh, J.-J. Lee, H. Y. Jeong, H. K. Kim, Y.-H. Kim and J.-B. Baek, *Sci. Adv.*, 2016, **2**, e1501459–e1501459.
- 219 I. Y. Jeon, H. M. Kim, I. T. Choi, K. Lim, J. Ko, J. C. Kim, H. J. Choi, M. J. Ju, J. J. Lee, H. K. Kim and J. B. Baek, *Nano Energy*, 2015, **13**, 336–345.
- 220 I. Y. Jeon, M. J. Ju, J. Xu, H. J. Choi, J. M. Seo, M. J. Kim, I. T. Choi, H. M. Kim, J. C. Kim, J. J. Lee, H. K. Liu, H. K. Kim, S. Dou, L. Dai and J. B. Baek, *Adv. Funct. Mater.*, 2015, **25**, 1170–1179.
- 221 J. Xu, I. Y. Jeon, J. M. Seo, S. Dou, L. Dai and J. B. Baek, *Adv. Mater.*, 2014, **26**, 7317–7323.
- 222 M. J. Ju, I. Y. Jeon, J. C. Kim, K. Lim, H. J. Choi, S. M. Jung, I. T. Choi, Y. K. Eom, Y. J. Kwon, J. Ko, J. J. Lee, H. K. Kim and J. B. Baek, *Adv. Mater.*, 2014, **26**, 3055–3062.
- 223 M. J. Ju, I.-Y. Jeon, K. Lim, J. C. Kim, H.-J. Choi, I. T. Choi, Y. K. Eom, Y. J. Kwon, J. Ko, J.-J. Lee, J.-B. Baek and H. K. Kim, *Energy Environ. Sci.*, 2014, **7**, 1044–1052.
- 224 S. M. Jung, I. T. Choi, K. Lim, J. Ko, J. C. Kim, J. J. Lee, M. J. Ju, H. K. Kim and J. B. Baek, *Chem. Mater.*, 2014, **26**, 3586–3591.
- 225 Z. Zhao, C. Y. Lin, J. Tang and Z. Xia, *Nano Energy*, 2018, **49**, 193–199.
- 226 X. Meng, C. Yu, X. Song, Y. Liu, S. Liang, Z. Liu, C. Hao and J. Qiu, *Adv. Energy Mater.*, 2015, **5**, 1500180.

- 227 D. Pan, C. Feng, L. Wang, Y. Liu, Z. Chen, W. Shi and Z. Li, *Electrochim. Acta*, 2016, **191**, 946–953.
- 228 J. Gong, Z. Zhou, K. Sumathy, H. Yang and Q. Qiao, *J. Appl. Phys.*, 2016, **119**, 135501.
- 229 G. Wang, J. Zhang, S. Hou, W. Zhang and Z. Zhao, *Nanoscale*, 2016, **8**, 9676–9681.
- 230 W. Wei, K. Sun and Y. H. Hu, *J. Mater. Chem. A*, 2016, **4**, 12054–12057.
- 231 X. Xu, W. Yang, B. Chen, C. Zhou, X. Ma, L. Hou, Y. Tang, F. Yang, G. Ning, L. Zhang and Y. Li, *Appl. Surf. Sci.*, 2017, **405**, 308–315.
- 232 W. Wei, D. J. Stacchiola and Y. H. Hu, *Int. J. Energy Res.*, 2017, 40–42.
- 233 X. Meng, C. Yu, X. Song, Z. Liu, B. Lu, C. Hao and J. Qiu, *J. Mater. Chem. A*, 2017, **5**, 2280–2287.
- 234 S. S. Nemala, K. S. Aneja, P. Bhargava, H. L. M. Bohm, S. Mallick and S. Bohm, *Electrochim. Acta*, 2018, **285**, 86–93.
- 235 Y. C. Chang, C. A. Tseng, C. P. Lee, S. B. Ann, Y. J. Huang, K. C. Ho and Y. T. Chen, *J. Power Sources*, 2019, 227470.
- 236 B. Yang, X. Zuo, P. Chen, L. Zhou, X. Yang, H. Zhang, G. Li, M. Wu, Y. Ma, S. Jin and X. Chen, *ACS Appl. Mater. Interfaces*, 2015, **7**, 137–143.
- 237 S. Q. Guo, X. Chen, F. Z. Hu, Q. C. Zhang and L. Liu, *ACS Appl. Mater. Interfaces*, 2015, **7**, 20164–20169.
- 238 C. Zhu, H. Min, F. Xu, J. Chen, H. Dong, L. Tong, Y. Zhu and L. Sun, *RSC Adv.*, 2015, **5**, 85822–85830.

- 239 C. P. Lee, C. A. Lin, T. C. Wei, M. L. Tsai, Y. Meng, C. T. Li, K. C. Ho, C. I. Wu, S. P. Lau and J. H. He, *Nano Energy*, 2015, **18**, 109–117.
- 240 P. Y. Chen, C. T. Li, C. P. Lee, R. Vittal and K. C. Ho, *Nano Energy*, 2015, **12**, 374–385.
- 241 J. Huo, J. Wu, M. Zheng, Y. Tu and Z. Lan, *J. Power Sources*, 2015, **293**, 570–576.
- 242 H. Elbohy, A. Aboagye, S. Sigdel, Q. Wang, M. H. Sayyad, L. Zhang and Q. Qiao, *J. Mater. Chem. A*, 2015, **3**, 17721–17727.
- 243 J. Ma, W. Shen, C. Li and F. Yu, *J. Mater. Chem. A*, 2015, **3**, 12307–12313.
- 244 J. Jia, J. Wu, J. Dong and J. Lin, *Electrochim. Acta*, 2015, **185**, 184–189.
- 245 H. Ren, H. Shao, L. Zhang, D. Guo, Q. Jin, R. Yu, L. Wang, Y. Li, Y. Wang, H. Zhao and D. Wang, *Adv. Energy Mater.*, 2015, **5**, 1–6.
- 246 Z. Lan, S. Gao, J. Wu and J. Lin, *J. Appl. Polym. Sci.*, 2015, **132**, 1–5.
- 247 I.-Y. Jeon, M. J. Ju, J. Xu, H.-J. Choi, J.-M. Seo, M.-J. Kim, I. T. Choi, H. M. Kim, J. C. Kim, J.-J. Lee, H. K. Liu, H. K. Kim, S. Dou, L. Dai and J.-B. Baek, *Adv. Funct. Mater.*, 2015, **25**, 1170–1179.
- 248 M. R. Al-bahrani, W. Ahmad, H. F. Mehnane, Y. Chen, Z. Cheng and Y. Gao, *Nano-Micro Lett.*, 2015, **7**, 298–306.
- 249 X. Meng, C. Yu, B. Lu, J. Yang and J. Qiu, *Nano Energy*, 2016, **22**, 59–69.
- 250 C. Yu, H. Fang, Z. Liu, H. Hu, X. Meng and J. Qiu, *Nano Energy*, 2016, **25**, 184–192.
- 251 Z. Zhou, S. Sigdel, J. Gong, B. Vaagensmith, H. Elbohy, H. Yang, S. Krishnan, X. F. Wu and Q. Qiao, *Nano Energy*, 2016, **22**, 558–563.

- 252 X. Cui, J. Xiao, Y. Wu, P. Du, R. Si, H. Yang, H. Tian, J. Li, W. H. Zhang, D. Deng and X. Bao, *Angew. Chemie - Int. Ed.*, 2016, **55**, 6708–6712.
- 253 I. A. Sahito, K. C. Sun, A. A. Arbab, M. B. Qadir, Y. S. Choi and S. H. Jeong, *J. Power Sources*, 2016, **319**, 90–98.
- 254 C. Yu, X. Meng, X. Song, S. Liang, Q. Dong, G. Wang, C. Hao, X. Yang, T. Ma, P. M. Ajayan and J. Qiu, *Carbon N. Y.*, 2016, **100**, 474–483.
- 255 S. Li, H. Min, F. Xu, L. Tong, J. Chen, C. Zhu and L. Sun, *RSC Adv.*, 2016, **6**, 34546–34552.
- 256 W. Yang, X. Xu, Z. Li, F. Yang, L. Zhang, Y. Li, A. Wang and S. Chen, *Carbon N. Y.*, 2016, **96**, 947–954.
- 257 F. Du, X. Zuo, Q. Yang, G. Li, Z. Ding, M. Wu, Y. Ma and K. Zhu, *J. Mater. Chem. C*, 2016, **4**, 10323–10328.
- 258 B. Kilic, S. Turkdogan, O. C. Ozer, M. Asgin, O. Bayrakli, G. Surucu, A. Astam and D. Ekinci, *Mater. Lett.*, 2016, **185**, 584–587.
- 259 G. Wang, J. Zhang, S. Kuang and W. Zhang, *Chem. - A Eur. J.*, 2016, **22**, 11763–11769.
- 260 K. S. Anuratha, M. Ramaprakash, S. K. Panda and S. Mohan, *Ceram. Int.*, 2017, **43**, 10174–10182.
- 261 H. Yuan, Q. Jiao, J. Liu, X. Liu, Y. Li, D. Shi, Q. Wu, Y. Zhao and H. Li, *Carbon N. Y.*, 2017, **122**, 381–388.
- 262 T. Liu, K. Yu, L. Gao, H. Chen, N. Wang, L. Hao, T. Li, H. He and Z. Guo, *J. Mater. Chem. A*, 2017, **5**, 17848–17855.

- 263 Z. Wang, B. Lu, X. Meng, C. Zhao, L. Huang, Z. Liu, C. Yu and J. Qiu, *Electrochim. Acta*, 2017, **252**, 84–90.
- 264 V. Murugadoss, N. Wang, S. Tadakamalla, B. Wang, Z. Guo and S. Angaiah, *J. Mater. Chem. A*, 2017, **5**, 14583–14594.
- 265 C. P. Lee, K. Y. Lai, C. A. Lin, C. T. Li, K. C. Ho, C. I. Wu, S. P. Lau and J. H. He, *Nano Energy*, 2017, **36**, 260–267.
- 266 M. Batmunkh, A. Shrestha, G. Gao, L. Yu, J. Zhao, M. J. Biggs, C. J. Shearer and J. G. Shapter, *Sol. RRL*, 2017, **1**, 1700011.
- 267 G. S. Shanker, G. B. Markad, M. Jagadeeswararao, U. Bansode and A. Nag, *ACS Energy Lett.*, 2017, **2**, 2251–2256.
- 268 M. Zhang, J. Zai, J. Liu, M. Chen, Z. Wang, G. Li, X. Qian, L. Qian and X. Yu, *Dalt. Trans.*, 2017, **46**, 9511–9516.
- 269 S. Sui, Y. Liao, Y. Xie, X. Wang, L. Li, Z. Luo, W. Zhou, G. Wang, K. Pan and A. Cabot, *ChemistrySelect*, 2017, **2**, 8927–8935.
- 270 V. D. Dao, L. L. Larina, Q. C. Tran, V. T. Bui, V. T. Nguyen, T. D. Pham, I. M. A. Mohamed, N. A. M. Barakat, B. T. Huy and H. S. Choi, *Carbon N. Y.*, 2017, **116**, 294–302.
- 271 J. Yao, K. Zhang, W. Wang, X. Zuo, Q. Yang, H. Tang, M. Wu and G. Li, *ACS Appl. Mater. Interfaces*, 2018, **10**, 19564–19572.
- 272 F. Yu, Y. Shi, X. Shen, W. Yao, S. Han and J. Ma, *ACS Sustain. Chem. Eng.*, 2018, **6**, 17427–17434.

- 273 C.-H. Tsai, C.-J. Shih, Y.-R. Chou, W.-F. Chi, W.-C. Huang and Y.-H. Yu, *Org. Electron.*, 2018, **52**, 51–60.
- 274 J. Ma, S. Yuan, S. Yang, H. Lu and Y. Li, *Appl. Surf. Sci.*, 2018, **440**, 8–15.
- 275 C. H. Tsai, C. J. Shih, W. S. Wang, W. F. Chi, W. C. Huang, Y. C. Hu and Y. H. Yu, *Appl. Surf. Sci.*, 2018, **434**, 412–422.
- 276 T. Jiang, S. Yang, P. Dai, X. Yu, Z. Bai, M. Wu, G. Li and C. Tu, *Electrochim. Acta*, 2018, **261**, 143–150.
- 277 B. Zhou, X. Zhang, P. Jin, X. Li, X. Yuan, J. Wang and L. Liu, *Electrochim. Acta*, 2018, **281**, 746–752.
- 278 H. Yuan, J. Liu, H. Li, Y. Li, X. Liu, D. Shi, Q. Wu and Q. Jiao, *J. Mater. Chem. A*, 2018, **6**, 5603–5607.
- 279 R. Karthick, A. Arulraj, M. Ramesh and M. Selvaraj, *J. Colloid Interface Sci.*, 2018, **530**, 179–188.
- 280 J. Chen, D. Wu, H. Wang, F. Wang, Y. Wang, Z. Gao, F. Xu and K. Jiang, *J. Colloid Interface Sci.*, 2018, **524**, 475–482.
- 281 K. Zhang, J. Yao, X. Zuo, Q. Yang, H. Tang and G. Li, *J. Electrochem. Soc.*, 2018, **165**, H916–H926.
- 282 M. Zhou, J. He, L. Wang, S. Zhao, Q. Wang, S. Cui, X. Qin and R. Wang, *Sol. Energy*, 2018, **166**, 71–79.
- 283 X. Meng, C. Yu, X. Song, J. Iocozzia, J. Hong, M. Rager, H. Jin, S. Wang, L. Huang, J. Qiu and Z. Lin, *Angew. Chemie*, 2018, **130**, 4772–4776.

- 284 V. D. Dao, N. D. Hoa, N. H. Vu, D. V. Quang, N. Van Hieu, T. T. N. Dung, N. X. Viet, C. M. Hung and H. S. Choi, *Sol. Energy*, 2019, **191**, 420–426.
- 285 B. Tang, H. Yu, W. Huang, Y. Sun, X. Li, S. Li and T. Ma, *RSC Adv.*, 2019, **9**, 15678–15685.
- 286 F. Yu, Y. Shi, W. Yao, S. Han and J. Ma, *J. Power Sources*, 2019, **412**, 366–373.
- 287 R. Senthilkumar, M. Balu, S. Ramakrishnan, P. C. Ramamurthy, S. K. Batabyal, D. Kumaresan and N. K. Kothurkar, *J. Electroanal. Chem.*, 2019, **847**, 113236.
- 288 S. Wang, X. Wang, Y. Xie, W. Jiang, X. Wang, Y. Jiang, W. Zhou and K. Pan, *J. Alloys Compd.*, 2019, **803**, 216–223.
- 289 Y. Zhao, J. Wang, L. Zheng, P. Sun, N. Huang, X. Huang and X. Sun, *J. Nanoparticle Res.*, 2019, **21**, 123.
- 290 S. Iijima, *Lett. to Nat.*, 1991, **353**, 737–740.
- 291 J. C. Byers, A. G. Güell and P. R. Unwin, *J. Am. Chem. Soc.*, 2014, **136**, 11252–11255.
- 292 Y. Cheng, J. Zhang and S. P. Jiang, *Chem. Commun.*, 2015, **51**, 13764–13767.
- 293 K. Suzuki, M. Yamaguchi, M. Kumagai and S. Yanagida, *Chem. Lett.*, 2003, **32**, 28–29.
- 294 Y. Cheng, C. Xu, L. Jia, J. D. Gale, L. Zhang, C. Liu, P. K. Shen and S. P. Jiang, *Appl. Catal. B Environ.*, 2015, **163**, 96–104.
- 295 K. Fujisawa, K. Komiyama, H. Muramatsu, D. Shimamoto, T. Tojo, Y. A. Kim, T. Hayashi, M. Endo, K. Oshida, M. Terrones and M. S. Dresselhaus, *ACS Nano*, 2011, **5**, 7547–7554.

- 296 C. Li, E. T. Thostenson and T. W. Chou, *Appl. Phys. Lett.*, 2007, **91**, 223114.
- 297 J. Hong, C. Yu, X. Song, X. Meng, H. Huang, C. Zhao, X. Han, Z. Wang and J. Qiu, *ACS Sustain. Chem. Eng.*, 2019, **7**, 7527–7534.
- 298 M. Wasim Khan, X. Zuo, Q. Yang, H. Tang, K. M. U. Rehman, M. Wu and G. Li, *Nanoscale*, 2020, **12**, 1046–1060.
- 299 M. S. Wu and Z. Z. Ceng, *Electrochim. Acta*, 2016, **191**, 895–901.
- 300 S. Huang, S. Li, Q. He, H. An, L. Xiao and L. Hou, *Appl. Surf. Sci.*, 2019, **476**, 769–777.
- 301 M. W. Khan, J. Yao, K. Zhang, X. Zuo, Q. Yang, H. Tang, K. M. U. Rehman, H. Zhang, G. Li, S. Jin and M. Wu, *J. Electroanal. Chem.*, 2019, **844**, 142–154.
- 302 Y. Li, X. Liu, H. Li, D. Shi, Q. Jiao, Y. Zhao, C. Feng, X. Bai, H. Wang and Q. Wu, *J. Power Sources*, 2019, **422**, 122–130.
- 303 M. Chen, G. C. Wang, L. L. Shao, Z. Y. Yuan, X. Qian, Q. S. Jing, Z. Y. Huang, D. L. Xu and S. X. Yang, *ACS Appl. Mater. Interfaces*, 2018, **10**, 31208–31224.
- 304 X. Wang, Y. Xie, Y. Jiao, K. Pan, B. Bateer, J. Wu and H. Fu, *J. Mater. Chem. A*, 2019, **7**, 10405–10411.
- 305 T. Liu, X. Mai, H. Chen, J. Ren, Z. Liu, Y. Li, L. Gao, N. Wang, J. Zhang, H. He and Z. Guo, *Nanoscale*, 2018, **10**, 4194–4201.
- 306 G. Yue, W. Wu, X. Liu and H. Zheng, *Sol. Energy*, 2018, **167**, 137–146.
- 307 M. Chen, G. C. Wang, W. Q. Yang, Z. Y. Yuan, X. Qian, J. Q. Xu, Z. Y. Huang and A. X. Ding, *ACS Appl. Mater. Interfaces*, 2019, **11**, 42156–42171.

- 308 B. Peng, M. Locascio, P. Zapol, S. Li, S. L. Mielke, G. C. Schatz and H. D. Espinosa, *Nat. Nanotechnol.*, 2008, **3**, 626–631.
- 309 A. Ali, K. Shehzad, F. Ur-Rahman, S. M. Shah, M. Khurram, M. Mumtaz and R. U. R. Sagar, *ACS Appl. Mater. Interfaces*, 2016, **8**, 25353–25360.
- 310 Y. Xue, Y. Ding, J. Niu, Z. Xia, A. Roy, H. Chen, J. Qu, Z. L. Wang and L. Dai, *Sci. Adv.*, 2015, **1**, 1–10.
- 311 Z. Yang, J. Deng, X. Sun, H. Li and H. Peng, *Adv. Mater.*, 2014, **26**, 2643–2647.
- 312 F. Lodermeier, M. Prato, R. D. Costa and D. M. Guldi, *Nanoscale*, 2016, **8**, 7556–7561.
- 313 A. A. Arbab, M. H. Peerzada, I. A. Sahito and S. H. Jeong, *J. Power Sources*, 2017, **343**, 412–423.
- 314 S. G. Hashmi, G. G. Sonai, H. Iftikhar, P. D. Lund and A. F. Nogueira, *Semicond. Sci. Technol.*, 2019, **34**, 105001.
- 315 A. Monreal-Bernal, J. J. Vilatela and R. D. Costa, *Carbon N. Y.*, 2019, **141**, 488–496.
- 316 J. Ma, C. Li, F. Yu and J. Chen, *J. Power Sources*, 2015, **273**, 1048–1055.
- 317 J. Y. Lin, W. Y. Wang and S. W. Chou, *J. Power Sources*, 2015, **282**, 348–357.
- 318 M. R. Al-Bahrani, W. Ahmad, S. Sen Ruan, Z. Yang, Z. Cheng and Y. Gao, *RSC Adv.*, 2015, **5**, 95551–95557.
- 319 L. Qiu, Q. Wu, Z. Yang, X. Sun, Y. Zhang and H. Peng, *Small*, 2015, **11**, 1150–1155.
- 320 M. Raissan Al-Bahrani, L. Liu, W. Ahmad, J. Tao, F. Tu, Z. Cheng and Y. Gao, *Appl. Surf. Sci.*, 2015, **331**, 333–338.

- 321 A. A. Arbab, K. C. Sun, I. A. Sahito, M. B. Qadir and S. H. Jeong, *Appl. Surf. Sci.*, 2015, **349**, 174–183.
- 322 J. Y. Lin, A. L. Su, C. Y. Chang, K. C. Hung and T. W. Lin, *ChemElectroChem*, 2015, **2**, 720–725.
- 323 J. Zhang, M. Yu, S. Li, Y. Meng, X. Wu and J. Liu, *J. Power Sources*, 2016, **334**, 44–51.
- 324 A. A. Arbab, K. C. Sun, I. A. Sahito, M. B. Qadir, Y. S. Choi and S. H. Jeong, *ACS Appl. Mater. Interfaces*, 2016, **8**, 7471–7482.
- 325 W. Hou, Y. Xiao, G. Han and H. Zhou, *Electrochim. Acta*, 2016, **190**, 720–728.
- 326 G. Wang, S. Kuang, J. Zhang, S. Hou and S. Nian, *Electrochim. Acta*, 2016, **187**, 243–248.
- 327 H. Chen, T. Liu, J. Ren, H. He, Y. Cao, N. Wang and Z. Guo, *J. Mater. Chem. A*, 2016, **4**, 3238–3244.
- 328 Z. Yang, W. Ahmad, L. Chu, M. R. Al-Bahrani, F. Tu, Y. Wang, H. Zhang, X. Wang, J. Su, N. Liu, L. Li, C. Yang and Y. Gao, *RSC Adv.*, 2016, **6**, 55071–55078.
- 329 G. Yue, X. Liu, Y. Mao, H. Zheng and W. Zhang, *Mater. Today Energy*, 2017, **4**, 58–65.
- 330 H. Li, Y. Xiao, G. Han and M. Li, *J. Mater. Sci.*, 2017, **52**, 8421–8431.
- 331 C. H. Lin, C. H. Tsai, F. G. Tseng, C. C. M. Ma, H. C. Wu and C. K. Hsieh, *J. Alloys Compd.*, 2017, **692**, 941–949.
- 332 A. Imbrogno, R. Pandiyan, M. Barberio, A. Macario, A. Bonanno and M. A. El khakani, *Mater. Renew. Sustain. Energy*, 2017, **6**, 11.

- 333 Y. A. Leu, M. H. Yeh, L. Y. Lin, T. J. Li, L. Y. Chang, S. Y. Shen, Y. S. Li, G. L. Chen, W. H. Chiang, J. J. Lin and K. C. Ho, *ACS Sustain. Chem. Eng.*, 2017, **5**, 537–546.
- 334 A. Shrestha, M. Batmunkh, C. J. Shearer, Y. Yin, G. G. Andersson, J. G. Shapter, S. Qiao and S. Dai, *Adv. Energy Mater.*, 2017, **7**, 1602276.
- 335 M. Chen, G. Zhao, L. L. Shao, Z. Y. Yuan, Q. S. Jing, K. J. Huang, Z. Y. Huang, X. H. Zhao and G. D. Zou, *Chem. Mater.*, 2017, **29**, 9680–9694.
- 336 Z. Xie, X. Cui, W. Xu and Y. Wang, *Electrochim. Acta*, 2017, **229**, 361–370.
- 337 Y. Liu, Y. Guo, M. Li, L. Wang, B. Geng, Z. Chen, Z. Li and D. Pan, *Electrochim. Acta*, 2017, **245**, 318–326.
- 338 Y. C. Shih, H. L. Lin and K. F. Lin, *J. Electroanal. Chem.*, 2017, **794**, 112–119.
- 339 E. Demir, B. Sen and F. Sen, *Nano-Structures and Nano-Objects*, 2017, **11**, 39–45.
- 340 X. Liu, L. Gao, G. Yue, H. Zheng and W. Zhang, *Sol. Energy*, 2017, **158**, 952–959.
- 341 L. Zheng, C. Bao, S. Lei, J. Wang, F. Li, P. Sun, N. Huang, L. Fang and X. Sun, *Carbon N. Y.*, 2018, **133**, 423–434.
- 342 M. H. Yeh, Y. A. Leu, W. H. Chiang, Y. S. Li, G. L. Chen, T. J. Li, L. Y. Chang, L. Y. Lin, J. J. Lin and K. C. Ho, *J. Power Sources*, 2018, **375**, 29–36.
- 343 J. W. Chew, M. H. Khanmirzaei, A. Numan, F. S. Omar, K. Ramesh and S. Ramesh, *Mater. Sci. Semicond. Process.*, 2018, **83**, 144–149.
- 344 J. Ou, C. Gong, J. Xiang and J. Liu, *Sol. Energy*, 2018, **174**, 225–230.
- 345 T. K. Chuang, K. S. Anuratha, J. Y. Lin, K. C. Huang, C. H. Su and C. K. Hsieh, *Surf. Coatings Technol.*, 2018, **344**, 534–540.

- 346 D. J. Yun, H. Ra, J. M. Kim, J. H. Lee, S. H. Park, J. Hwang, J. G. Chung, S. H. Kim, Y. S. Kim, Y. J. Jeong and S. H. Lee, *Appl. Surf. Sci.*, 2019, **487**, 480–487.
- 347 W. Maiaugree, T. Tansoonton, V. Amornkitbamrung and E. Swatsitang, *Curr. Appl. Phys.*, 2019, **19**, 1355–1361.
- 348 U. Mehmood, W. Ahmad and S. Ahmed, *Sustain. Energy Fuels*, 2019, **3**, 3473–3480.
- 349 M. Younas, M. A. Gondal, M. A. Dastageer and K. Harrabi, *Sol. Energy*, 2019, **188**, 1178–1188.
- 350 D. J. Yun, H. Ra, J. M. Kim, E. Oh, J. Lee, M. H. Jeong, Y. J. Jeong, H. Yang and J. Jang, *Org. Electron.*, 2019, **65**, 349–356.
- 351 Y. Di, Z. Xiao, Z. Zhao, G. Ru, B. Chen and J. Feng, *J. Alloys Compd.*, 2019, **788**, 198–205.
- 352 Q. Ngo, T. Yamada, M. Suzuki, Y. Ominami, A. M. Cassell, M. Meyyappan and C. Y. Yang, *IEEE Trans. Nanotechnol.*, 2007, **6**, 688–695.
- 353 E. Zussman, X. Chen, W. Ding, L. Calabri, D. A. Dikin, J. P. Quintana and R. S. Ruoff, *Carbon N. Y.*, 2005, **43**, 2175–2185.
- 354 C. Wei and D. Srivastava, *Appl. Phys. Lett.*, 2004, **85**, 2208–2210.
- 355 P. Joshi, L. Zhang, Q. Chen, D. Galipeau, H. Fong and Q. Qiao, *ACS Appl. Mater. Interfaces*, 2010, **2**, 3572–3577.
- 356 D. Sebastián, V. Baglio, M. Girolamo, R. Moliner, M. J. Lázaro and A. S. Aricò, *J. Power Sources*, 2014, **250**, 242–249.
- 357 G. Bin Zheng, K. Kouda, H. Sano, Y. Uchiyama, Y. F. Shi and H. J. Quan, *Carbon N. Y.*, 2004, **42**, 635–640.

- 358 V. I. Merkulov, D. K. Hensley, M. V. Melechko, M. A. Guillorn, D. H. Lowndes and M. L. Simpson, *J. Phys. Chem. B*, 2002, **106**, 10570–10577.
- 359 Y. Zhao, Y. Liu, C. Tong, J. Ru, B. Geng, Z. Ma, H. Liu and L. Wang, *J. Mater. Sci.*, 2018, **53**, 7637–7647.
- 360 Y. H. Wang, H. Q. Fang, Q. Dong, D. H. Si, X. D. Song, C. Yu and J. S. Qiu, *RSC Adv.*, 2018, **8**, 7040–7043.
- 361 A. Yousef, R. M. Brooks, M. H. El-Newehy, S. S. Al-Deyab and H. Y. Kim, *Int. J. Hydrogen Energy*, 2017, **42**, 10407–10415.
- 362 L. Song, X. Yin, X. Xie, P. Du, J. Xiong and F. Ko, *Electrochim. Acta*, 2017, **255**, 256–265.
- 363 K. Xiong, Z. Liu, J. Yuan, K. Li, G. Li, S. Jin, C. Luo, L. Zhu, H. Shi and X. Xiao, *J. Mater. Sci. Mater. Electron.*, 2017, **28**, 1679–1683.
- 364 G. H. Kim, S. H. Park, M. S. Birajdar, J. Lee and S. C. Hong, *J. Ind. Eng. Chem.*, 2017, **52**, 211–217.
- 365 H. Guo, Y. Zhu, W. Li, H. Zheng, K. Wu, K. Ding, B. Ruan, A. Hagfeldt, T. Ma and M. Wu, *Electrochim. Acta*, 2015, **176**, 997–1000.
- 366 L. Li, X. Zhang, Z. Li, S. Liu, X. Li, Y. Zhang and W. Zhang, *Mater. Today Commun.*, 2019, **18**, 1–6.
- 367 A. Aboagye, H. Elbohy, A. D. Kelkar, Q. Qiao, J. Zai, X. Qian and L. Zhang, *Nano Energy*, 2015, **11**, 550–556.
- 368 L. Chen, Y. Zhou, H. Dai, T. Yu, J. Liu and Z. Zou, *Nano Energy*, 2015, **11**, 697–703.

- 369 L. Li, X. Zhang, D. Wang, W. Zhang, X. Li, X. Zhao, Q. Zhang, L. Gu, Z. Yu and M. Wu, *Electrochim. Acta*, 2018, **280**, 94–100.
- 370 L. Song, X. Yin, X. Xie, P. Du, J. Xiong and F. Ko, *Electrochim. Acta*, 2017, **255**, 256–265.
- 371 L. Song, T. Wang, W. Jing, X. Xie, P. Du and J. Xiong, *Mater. Res. Bull.*, 2019, **118**, 110522.
- 372 L. Chen, H. Dai, Y. Zhou, Y. Hu, T. Yu, J. Liu and Z. Zou, *Chem. Commun.*, 2014, **50**, 14321–14324.
- 373 G. Wang, S. Kuang and W. Zhang, *Mater. Lett.*, 2016, **174**, 14–16.
- 374 L. Li, J. Xiao, H. Sui, X. Yang, W. Zhang, X. Li, A. Hagfeldt and M. Wu, *J. Power Sources*, 2016, **326**, 6–13.
- 375 X. Ma, H. Elbohy, S. Sigdel, C. Lai, Q. Qiao and H. Fong, *RSC Adv.*, 2016, **6**, 11481–11487.
- 376 L. Li, M. Wang, J. Xiao, H. Sui, W. Zhang, X. Li, K. Yang, Y. Zhang and M. Wu, *Electrochim. Acta*, 2016, **219**, 350–355.
- 377 J. Xiao, M. Cui, M. Wang, H. Sui, K. Yang, L. Li, W. Zhang, X. Li, G. Fu, A. Hagfeldt and Y. Zhang, *J. Power Sources*, 2016, **328**, 543–550.
- 378 L. Li, Q. Lu, J. Xiao, J. Li, H. Mi, R. Duan, J. Li, W. Zhang, X. Li, S. Liu, K. Yang, M. Wu and Y. Zhang, *J. Power Sources*, 2017, **363**, 9–15.
- 379 J. Qiu, D. He, R. Zhao, B. Sun, H. Ji, N. Zhang, Y. Li, X. Lu and C. Wang, *J. Colloid Interface Sci.*, 2018, **522**, 95–103.

- 380 L. Li, H. Sui, K. Zhao, W. Zhang, X. Li, S. Liu, K. Yang, M. Wu and Y. Zhang, *Electrochim. Acta*, 2018, **259**, 188–195.
- 381 L. Li, Q. Lu, J. Li, X. Liu, G. Shi, F. Liu, S. Liu, W. Ding, X. Zhao and Y. Zhang, *Appl. Surf. Sci.*, 2018, **448**, 522–528.
- 382 L. Li, X. Wang, Z. Ma, L. Liu, H. Wang, W. Zhang and X. Li, *Appl. Surf. Sci.*, 2019, **475**, 109–116.
- 383 L. Li, X. Zhang, L. Fu, Q. Wang, S. Ji, M. Wu, H. Wang and W. Zhang, *Compos. Part B Eng.*, 2019, **173**, 107026.
- 384 K. Zhao, X. Zhang, M. Wang, W. Zhang, X. Li, H. Wang and L. Li, *J. Alloys Compd.*, 2019, **786**, 50–55.
- 385 M. A. Green, E. D. Dunlop, D. H. Levi, J. Hohl-Ebinger, M. Yoshita and A. W. Y. Ho-Baillie, *Prog. Photovoltaics Res. Appl.*, 2019, **27**, 565–575.
- 386 M. M. Lee, J. Teuscher, T. Miyasaka, T. N. Murakami and H. J. Snaith, *Science*, 2012, **338**, 643–647.
- 387 J. S. Manser, M. I. Saidaminov, J. A. Christians, O. M. Bakr and P. V Kamat, *Acc. Chem. Res.*, 2016, **49**, 330–338.
- 388 J.-H. Im, I.-H. Jang, N. Pellet, M. Grätzel and N.-G. Park, *Nat Nano*, 2014, **9**, 927–932.
- 389 S. Y. Sun, T. Salim, N. Mathews, M. Duchamp, C. Boothroyd, G. C. Xing, T. C. Sum and Y. M. Lam, *Energy Environ. Sci.*, 2014, **7**, 399–407.
- 390 C. Wehrenfennig, G. E. Eperon, M. B. Johnston, H. J. Snaith and L. M. Herz, *Adv. Mater.*, 2014, **26**, 1584–1589.

- 391 G. Xing, N. Mathews, S. Sun, S. S. Lim, Y. M. Lam, M. Grätzel, S. Mhaisalkar and T. C. Sum, *Science*, 2013, **342**, 344–347.
- 392 S. D. Stranks, G. E. Eperon, G. Grancini, C. Menelaou, M. J. P. Alcocer, T. Leijtens, L. M. Herz, A. Petrozza and H. J. Snaith, *Science*, 2013, **342**, 341–344.
- 393 V. D’Innocenzo, G. Grancini, M. J. P. Alcocer, A. R. S. Kandada, S. D. Stranks, M. M. Lee, G. Lanzani, H. J. Snaith and A. Petrozza, *Nat. Commun.*, 2014, **5**, 3586.
- 394 A. Guerrero, J. You, C. Aranda, Y. S. Kang, G. Garcia-Belmonte, H. Zhou, J. Bisquert and Y. Yang, *ACS Nano*, 2016, **10**, 218–224.
- 395 T. Leijtens, G. E. Eperon, S. Pathak, A. Abate, M. M. Lee and H. J. Snaith, *Nat. Commun.*, 2013, **4**, 2885.
- 396 C. Besleaga, L. E. Abramiuc, V. Stancu, A. G. Tomulescu, M. Sima, L. Trinca, N. Plugaru, L. Pintilie, G. A. Nemnes, M. Iliescu, H. G. Svavarsson, A. Manolescu and I. Pintilie, *J. Phys. Chem. Lett.*, 2016, **7**, 5168–5175.
- 397 K. Domanski, J.-P. Correa-Baena, N. Mine, M. K. Nazeeruddin, A. Abate, M. Saliba, W. Tress, A. Hagfeldt and M. Grätzel, *ACS Nano*, 2016, **10**, 6306–6314.
- 398 N. N. Shlenskaya, N. A. Belich, M. Grätzel, E. A. Goodilin and A. B. Tarasov, *J. Mater. Chem. A*, 2018, **6**, 1780–1786.
- 399 S. Cacovich, L. Ciná, F. Matteocci, G. Divitini, P. A. Midgley, A. Di Carlo and C. Ducati, *Nanoscale*, 2017, **9**, 4700–4706.
- 400 L. Zhao, R. A. Kerner, Z. Xiao, Y. L. Lin, K. M. Lee, J. Schwartz and B. P. Rand, *ACS Energy Lett.*, 2016, **1**, 595–602.
- 401 Y. Rong, L. Liu, A. Mei, X. Li and H. Han, *Adv. Energy Mater.*, 2015, **5**, 1501066.

- 402 R. L. McCreery, *Chem. Rev.*, 2008, **108**, 2646–2687.
- 403 Y. Cai, L. Liang and P. Gao, *Chinese Phys. B*, 2018, **27**, 18805.
- 404 Y. Rong, Z. Ku, A. Mei, T. Liu, M. Xu, S. Ko, X. Li and H. Han, *J. Phys. Chem. Lett.*, 2014, **5**, 2160–2164.
- 405 T. Liu, L. Liu, M. Hu, Y. Yang, L. Zhang, A. Mei and H. Han, *J. Power Sources*, 2015, **293**, 533–538.
- 406 Z.-L. Yang, Z.-Y. Zhang, W.-L. Fan, C. Hu, L. Zhang and J.-J. Qi, *Sol. Energy*, 2019, **193**, 859–865.
- 407 H. Liu, B. Yang, H. Chen, K. Li, G. Liu, Y. Yuan, Y. Gao and C. Zhou, *Org. Electron.*, 2018, **58**, 69–74.
- 408 M. Hu, L. Liu, A. Mei, Y. Yang, T. Liu and H. Han, *J. Mater. Chem. A*, 2014, **2**, 17115–17121.
- 409 Z. Ku, Y. Rong, M. Xu, T. Liu and H. Han, *Sci. Rep.*, 2013, **3**, 3132.
- 410 K. Cao, Z. Zuo, J. Cui, Y. Shen, T. Moehl, S. M. Zakeeruddin, M. Grätzel and M. Wang, *Nano Energy*, 2015, **17**, 171–179.
- 411 A. Mei, X. Li, L. Liu, Z. Ku, T. Liu, Y. Rong, M. Xu, M. Hu, J. Chen, Y. Yang, M. Grätzel and H. Han, *Science*, 2014, **345**, 295–298.
- 412 L. Xu, F. Wan, Y. Rong, H. Chen, S. He, X. Xu, G. Liu, H. Han, Y. Yuan, J. Yang, Y. Gao, B. Yang and C. Zhou, *Org. Electron.*, 2017, **45**, 131–138.
- 413 Y. Hu, Z. Zhang, A. Mei, Y. Jiang, X. Hou, Q. Wang, K. Du, Y. Rong, Y. Zhou, G. Xu and H. Han, *Adv. Mater.*, 2018, **30**, 1705786.

- 414 L. Zhang, T. Liu, L. Liu, M. Hu, Y. Yang, A. Mei and H. Han, *J. Mater. Chem. A*, 2015, **3**, 9165–9170.
- 415 P. Jiang, T. W. Jones, N. W. Duffy, K. F. Anderson, R. Bennett, M. Grigore, P. Marvig, Y. Xiong, T. Liu, Y. Sheng, L. Hong, X. Hou, M. Duan, Y. Hu, Y. Rong, G. J. Wilson and H. Han, *Carbon N. Y.*, 2018, **129**, 830–836.
- 416 D. L. Carroll, P. Redlich, X. Blase, J. C. Charlier, S. Curran, P. M. Ajayan, S. Roth and M. Rühle, *Phys. Rev. Lett.*, 1998, **81**, 2332–2335.
- 417 Y. A. Kim, K. Fujisawa, H. Muramatsu, T. Hayashi, M. Endo, T. Fujimori, K. Kaneko, M. Terrones, J. Behrends, A. Eckmann, C. Casiraghi, K. S. Novoselov, R. Saito and M. S. Dresselhaus, *ACS Nano*, 2012, **6**, 6293–6300.
- 418 L. S. Panchakarla, K. S. Subrahmanyam, S. K. Saha, A. Govindaraj, H. R. Krishnamurthy, U. V Waghmare and C. N. R. Rao, *Adv. Mater.*, 2009, **21**, 4726–4730.
- 419 P. Jiang, Y. Xiong, M. Xu, A. Mei, Y. Sheng, L. Hong, T. W. Jones, G. J. Wilson, S. Xiong, D. Li, Y. Hu, Y. Rong and H. Han, *J. Phys. Chem. C*, 2018, **122**, 16481–16487.
- 420 M. Duan, C. Tian, Y. Hu, A. Mei, Y. Rong, Y. Xiong, M. Xu, Y. Sheng, P. Jiang, X. Hou, X. Zhu, F. Qin and H. Han, *ACS Appl. Mater. Interfaces*, 2017, **9**, 31721–31727.
- 421 M. Chen, R.-H. Zha, Z.-Y. Yuan, Q.-S. Jing, Z.-Y. Huang, X.-K. Yang, S.-M. Yang, X.-H. Zhao, D.-L. Xu and G.-D. Zou, *Chem. Eng. J.*, 2017, **313**, 791–800.
- 422 C. Tian, A. Mei, S. Zhang, H. Tian, S. Liu, F. Qin, Y. Xiong, Y. Rong, Y. Hu, Y. Zhou, S. Xie and H. Han, *Nano Energy*, 2018, **53**, 160–167.
- 423 T. Liu, Y. Rong, Y. Xiong, A. Mei, Y. Hu, Y. Sheng, P. Jiang, X. Hou, M. Duan, Y. Guan, L. Hong and H. Han, *RSC Adv.*, 2017, **7**, 10118–10123.

- 424 Z. Meng, D. Guo and K. Fan, *Appl. Surf. Sci.*, 2018, **430**, 632–638.
- 425 T. Liu, Y. Xiong, A. Mei, Y. Hu, Y. Rong, M. Xu, Z. Wang, L. Lou, D. Du, S. Zheng, X. Long, S. Xiao, S. Yang and H. Han, *RSC Adv.*, 2019, **9**, 29840–29846.
- 426 S. Bhandari, A. Roy, A. Ghosh, T. K. Mallick and S. Sundaram, *ACS Omega*, 2020, **5**, 422–429.
- 427 L. Zhou, Y. Zuo, T. K. Mallick and S. Sundaram, *Sci. Rep.*, 2019, **9**, 8778.
- 428 S. Guarnera, A. Abate, W. Zhang, J. M. Foster, G. Richardson, A. Petrozza and H. J. Snaith, *J. Phys. Chem. Lett.*, 2015, **6**, 432–437.
- 429 Y. Yang, H. Chen, X. Zheng, X. Meng, T. Zhang, C. Hu, Y. Bai, S. Xiao and S. Yang, *Nano Energy*, 2017, **42**, 322–333.
- 430 G. S. Han, H. S. Chung, B. J. Kim, D. H. Kim, J. W. Lee, B. S. Swain, K. Mahmood, J. S. Yoo, N.-G. Park, J. H. Lee and H. S. Jung, *J. Mater. Chem. A*, 2015, **3**, 9160–9164.
- 431 Y. H. Lee, J. Luo, M.-K. Son, P. Gao, K. T. Cho, J. Seo, S. M. Zakeeruddin, M. Grätzel and M. K. Nazeeruddin, *Adv. Mater.*, 2016, **28**, 3966–3972.
- 432 J. M. Marin-Beloqui, L. Lanzetta and E. Palomares, *Chem. Mater.*, 2016, **28**, 207–213.
- 433 S. F. Shaikh, H.-C. Kwon, W. Yang, H. Hwang, H. Lee, E. Lee, S. Ma and J. Moon, *J. Mater. Chem. A*, 2016, **4**, 15478–15485.
- 434 Y. Xiong, X. Zhu, A. Mei, F. Qin, S. Liu, S. Zhang, Y. Jiang, Y. Zhou and H. Han, *Sol. RRL*, 2018, **2**, 1800002.
- 435 Q. Wang, S. Liu, Y. Ming, Y. Guan, D. Li, C. Zhang, Z. Wang, Y. Rong, Y. Hu and H. Han, *Sustain. Energy Fuels*, 2018, **2**, 2412–2418.

- 436 J. Chen, Y. Rong, A. Mei, Y. Xiong, T. Liu, Y. Sheng, P. Jiang, L. Hong, Y. Guan, X. Zhu, X. Hou, M. Duan, J. Zhao, X. Li and H. Han, *Adv. Energy Mater.*, 2016, **6**, 1502009.
- 437 S. Liu, W. Huang, P. Liao, N. Pootrakulchote, H. Li, J. Lu, J. Li, F. Huang, X. Shai, X. Zhao, Y. Shen, Y.-B. Cheng and M. Wang, *J. Mater. Chem. A*, 2017, **5**, 22952–22958.
- 438 P. Zhang, G. Kapil, K. Hamada, S. S. Pandey, T. Ma and S. Hayase, *ACS Sustain. Chem. Eng.*, 2018, **6**, 10221–10228.
- 439 J. Chen, Y. Xiong, Y. Rong, A. Mei, Y. Sheng, P. Jiang, Y. Hu, X. Li and H. Han, *Nano Energy*, 2016, **27**, 130–137.
- 440 X. Hou, Y. Hu, H. Liu, A. Mei, X. Li, M. Duan, G. Zhang, Y. Rong and H. Han, *J. Mater. Chem. A*, 2017, **5**, 73–78.
- 441 A. M. A. Leguy, Y. Hu, M. Campoy-Quiles, M. I. Alonso, O. J. Weber, P. Azarhoosh, M. van Schilfgaarde, M. T. Weller, T. Bein, J. Nelson, P. Docampo and P. R. F. Barnes, *Chem. Mater.*, 2015, **27**, 3397–3407.
- 442 R. J. Sutton, G. E. Eperon, L. Miranda, E. S. Parrott, B. A. Kamino, J. B. Patel, M. T. Hörantner, M. B. Johnston, A. A. Haghighirad, D. T. Moore and H. J. Snaith, *Adv. Energy Mater.*, 2016, **6**, 1502458.
- 443 B. Conings, J. Drijkoningen, N. Gauquelin, A. Babayigit, J. D’Haen, L. D’Olieslaeger, A. Ethirajan, J. Verbeeck, J. Manca, E. Mosconi, F. De Angelis and H.-G. Boyen, *Adv. Energy Mater.*, 2015, **5**, 1500477.
- 444 N. H. Tiep, Z. Ku and H. J. Fan, *Adv. Energy Mater.*, 2016, **6**, 1501420.
- 445 C. Lu, M. Paramasivam, K. Park, C. H. Kim and H. K. Kim, *ACS Appl. Mater. Interfaces*, 2019, **11**, 14011–14022.

- 446 Y. Rong, X. Hou, Y. Hu, A. Mei, L. Liu, P. Wang and H. Han, *Nat. Commun.*, 2017, **8**, 14555.
- 447 S. Liu, S. Li, J. Wu, Q. Wang, Y. Ming, D. Zhang, Y. Sheng, Y. Hu, Y. Rong, A. Mei and H. Han, *J. Phys. Chem. Lett.*, 2019, **10**, 6865–6872.
- 448 A. Mei, X. Li, L. Liu, Z. Ku, T. Liu, Y. Rong, M. Xu, M. Hu, J. Chen, Y. Yang, M. Grätzel and H. Han, *Science*, 2014, **345**, 295–8.
- 449 X. Jiang, Y. Xiong, Z. Zhang, Y. Rong, A. Mei, C. Tian, J. Zhang, Y. Zhang, Y. Jin, H. Han and Q. Liu, *Electrochim. Acta*, 2018, **263**, 134–139.
- 450 H. Zhou, Y. Shi, Q. Dong, H. Zhang, Y. Xing, K. Wang, Y. Du and T. Ma, *J. Phys. Chem. Lett.*, 2014, **5**, 3241–3246.
- 451 Y. Yang, J. Xiao, H. Wei, L. Zhu, D. Li, Y. Luo, H. Wu and Q. Meng, *RSC Adv.*, 2014, **4**, 52825–52830.
- 452 S. Gholipour, J.-P. Correa-Baena, K. Domanski, T. Matsui, L. Steier, F. Giordano, F. Tajabadi, W. Tress, M. Saliba, A. Abate, A. Morteza Ali, N. Taghavinia, M. Grätzel and A. Hagfeldt, *Adv. Energy Mater.*, 2016, **6**, 1601116.
- 453 L. Gao, Y. Zhou, F. Meng, Y. Li, A. Liu, Y. Li, C. Zhang, M. Fan, G. Wei and T. Ma, *Carbon N. Y.*, 2020, **162**, 267–272.
- 454 Q.-Q. Chu, B. Ding, Q. Qiu, Y. Liu, C.-X. Li, C.-J. Li, G.-J. Yang and B. Fang, *J. Mater. Chem. A*, 2018, **6**, 8271–8279.
- 455 Q.-Q. Chu, B. Ding, Y. Li, L. Gao, Q. Qiu, C.-X. Li, C.-J. Li, G.-J. Yang and B. Fang, *ACS Sustain. Chem. Eng.*, 2017, **5**, 9758–9765.

- 456 H. Wei, J. Xiao, Y. Yang, S. Lv, J. Shi, X. Xu, J. Dong, Y. Luo, D. Li and Q. Meng, *Carbon N. Y.*, 2015, **93**, 861–868.
- 457 S. He, L. Qiu, D.-Y. Son, Z. Liu, E. J. Juarez-Perez, L. K. Ono, C. Stecker and Y. Qi, *ACS Energy Lett.*, 2019, **4**, 2032–2039.
- 458 H. Ye, Z. Liu, X. Liu, B. Sun, X. Tan, Y. Tu, T. Shi, Z. Tang and G. Liao, *Appl. Surf. Sci.*, 2019, **478**, 417–425.
- 459 Y. Lv, Y. Jin, W. Cai, Z. Zhang, X. Zhou and H. Chen, *J. Alloys Compd.*, 2020, **821**, 153272.
- 460 N. Arora, M. I. Dar, S. Akin, R. Uchida, T. Baumeler, Y. Liu, S. M. Zakeeruddin and M. Grätzel, *Small*, 2019, **15**, 1904746.
- 461 A. K. Baranwal, H. Kanda, N. Shibayama and S. Ito, *Sustain. Energy Fuels*, 2018, **2**, 2778–2787.
- 462 F. Zhang, X. Yang, M. Cheng, W. Wang and L. Sun, *Nano Energy*, 2016, **20**, 108–116.
- 463 X. Jiang, Z. Yu, H.-B. Li, Y. Zhao, J. Qu, J. Lai, W. Ma, D. Wang, X. Yang and L. Sun, *J. Mater. Chem. A*, 2017, **5**, 17862–17866.
- 464 F. Zhang, X. Yang, M. Cheng, J. Li, W. Wang, H. Wang and L. Sun, *J. Mater. Chem. A*, 2015, **3**, 24272–24280.
- 465 L. Chu, W. Liu, Z. Qin, R. Zhang, R. Hu, J. Yang, J. Yang and X. Li, *Sol. Energy Mater. Sol. Cells*, 2018, **178**, 164–169.
- 466 H. Chen, Z. Wei, H. He, X. Zheng, K. S. Wong and S. Yang, *Adv. Energy Mater.*, 2016, **6**, 1502087.

- 467 X. Chang, W. Li, H. Chen, L. Zhu, H. Liu, H. Geng, S. Xiang, J. Liu, X. Zheng, Y. Yang and S. Yang, *ACS Appl. Mater. Interfaces*, 2016, **8**, 30184–30192.
- 468 F. Zhang, X. Yang, H. Wang, M. Cheng, J. Zhao and L. Sun, *ACS Appl. Mater. Interfaces*, 2014, **6**, 16140–16146.
- 469 Y. Xiao, N. Cheng, K. K. Kondamareddy, C. Wang, P. Liu, S. Guo and X.-Z. Zhao, *J. Power Sources*, 2017, **342**, 489–494.
- 470 X. Liu, Z. Liu, B. Sun, X. Tan, H. Ye, Y. Tu, T. Shi, Z. Tang and G. Liao, *Nano Energy*, 2018, **50**, 201–211.
- 471 J. Liu, L. Zhu, S. Xiang, H. Wang, H. Liu, W. Li and H. Chen, *ACS Sustain. Chem. Eng.*, 2019, **7**, 16927–16932.
- 472 H. Hu, B. Dong, H. Hu, F. Chen, M. Kong, Q. Zhang, T. Luo, L. Zhao, Z. Guo, J. Li, Z. Xu, S. Wang, D. Eder and L. Wan, *ACS Appl. Mater. Interfaces*, 2016, **8**, 17999–18007.
- 473 Y. Xiao, C. Wang, K. K. Kondamareddy, N. Cheng, P. Liu, Y. Qiu, F. Qi, S. Kong, W. Liu and X.-Z. Zhao, *ACS Appl. Energy Mater.*, 2018, **1**, 5453–5462.
- 474 W. Liu, L. Chu, R. Hu, R. Zhang, Y. Ma, Y. Pu, J. Zhang, J. Yang, X. Li and W. Huang, *Sol. Energy*, 2018, **166**, 42–49.
- 475 Z. Liu, S. Bi, G. Hou, C. Ying and X. Su, *J. Power Sources*, 2019, **430**, 12–19.
- 476 B. Zhang, B. Zhang, S. Wang, S. Yao, H. Bala, G. Sun, J. Cao and Z. Zhang, *Electrochim. Acta*, 2020, **338**, 135884.
- 477 W. Fan, Z. Wei, Z. Zhang, F. Qiu, C. Hu, Z. Li, M. Xu and J. Qi, *Inorg. Chem. Front.*, 2019, **6**, 2767–2775.

- 478 C. Zhang, Q. Luo, X. Deng, J. Zheng, W. Ou-Yang, X. Chen and S. Huang, *Electrochim. Acta*, 2017, **258**, 1262–1272.
- 479 Z. Liu, B. Sun, X. Liu, J. Han, H. Ye, Y. Tu, C. Chen, T. Shi, Z. Tang and G. Liao, *J. Mater. Chem. A*, 2018, **6**, 7409–7419.
- 480 X. Guo, H. Dong, W. Li, N. Li and L. Wang, *ChemPhysChem*, 2015, **16**, 1727–1732.
- 481 S. Lin, B. Yang, X. Qiu, J. Yan, J. Shi, Y. Yuan, W. Tan, X. Liu, H. Huang, Y. Gao and C. Zhou, *Org. Electron.*, 2018, **53**, 235–241.
- 482 X. Wu, L. Xie, K. Lin, J. Lu, K. Wang, W. Feng, B. Fan, P. Yin and Z. Wei, *J. Mater. Chem. A*, 2019, **7**, 12236–12243.
- 483 G. D. M. R. Dabera, K. D. G. I. Jayawardena, M. R. R. Prabhath, I. Yahya, Y. Y. Tan, N. A. Nismy, H. Shiozawa, M. Sauer, G. Ruiz-Soria, P. Ayala, V. Stolojan, A. A. D. T. Adikaari, P. D. Jarowski, T. Pichler and S. R. P. Silva, *ACS Nano*, 2013, **7**, 556–565.
- 484 Y. Jung, X. Li, N. K. Rajan, A. D. Taylor and M. A. Reed, *Nano Lett.*, 2013, **13**, 95–99.
- 485 P. G. Collins, K. Bradley, M. Ishigami and A. Zettl, *Science*, 2000, **287**, 1801–1804.
- 486 P. Liu, Q. Sun, F. Zhu, K. Liu, K. Jiang, L. Liu, Q. Li and S. Fan, *Nano Lett.*, 2008, **8**, 647–651.
- 487 J. Ryu, K. Lee, J. Yun, H. Yu, J. Lee and J. Jang, *Small*, 2017, **13**, 1701225.
- 488 Y. Wang, H. Zhao, Y. Mei, H. Liu, S. Wang and X. Li, *ACS Appl. Mater. Interfaces*, 2019, **11**, 916–923.

- 489 H. Li, K. Cao, J. Cui, S. Liu, X. Qiao, Y. Shen and M. Wang, *Nanoscale*, 2016, **8**, 6379–6385.
- 490 Z. Li, S. A. Kulkarni, P. P. Boix, E. Shi, A. Cao, K. Fu, S. K. Batabyal, J. Zhang, Q. Xiong, L. H. Wong, N. Mathews and S. G. Mhaisalkar, *ACS Nano*, 2014, **8**, 6797–6804.
- 491 Z. Wei, H. Chen, K. Yan, X. Zheng and S. Yang, *J. Mater. Chem. A*, 2015, **3**, 24226–24231.
- 492 X. Zheng, H. Chen, Q. Li, Y. Yang, Z. Wei, Y. Bai, Y. Qiu, D. Zhou, K. S. Wong and S. Yang, *Nano Lett.*, 2017, **17**, 2496–2505.
- 493 K. Aitola, K. Sveinbjörnsson, J.-P. Correa-Baena, A. Kaskela, A. Abate, Y. Tian, E. M. J. Johansson, M. Grätzel, E. I. Kauppinen, A. Hagfeldt and G. Boschloo, *Energy Environ. Sci.*, 2016, **9**, 461–466.
- 494 N. Ahn, I. Jeon, J. Yoon, E. I. Kauppinen, Y. Matsuo, S. Maruyama and M. Choi, *J. Mater. Chem. A*, 2018, **6**, 1382–1389.
- 495 Q. Luo, H. Ma, Q. Hou, Y. Li, J. Ren, X. Dai, Z. Yao, Y. Zhou, L. Xiang, H. Du, H. He, N. Wang, K. Jiang, H. Lin, H. Zhang and Z. Guo, *Adv. Funct. Mater.*, 2018, **28**, 1706777.
- 496 Y. Yang, Z. Liu, W. K. Ng, L. Zhang, H. Zhang, X. Meng, Y. Bai, S. Xiao, T. Zhang, C. Hu, K. S. Wong and S. Yang, *Adv. Funct. Mater.*, 2019, **29**, 1806506.
- 497 X. Zheng, H. Chen, Z. Wei, Y. Yang, H. Lin and S. Yang, *Front. Optoelectron.*, 2016, **9**, 71–80.
- 498 Q. Luo, H. Ma, Y. Zhang, X. Yin, Z. Yao, N. Wang, J. Li, S. Fan, K. Jiang and H. Lin, *J. Mater. Chem. A*, 2016, **4**, 5569–5577.

- 499 P. You, Z. Liu, Q. Tai, S. Liu and F. Yan, *Adv. Mater.*, 2015, **27**, 3632–3638.
- 500 F. Lang, M. A. Gluba, S. Albrecht, J. Rappich, L. Korte, B. Rech and N. H. Nickel, *J. Phys. Chem. Lett.*, 2015, **6**, 2745–2750.
- 501 Y. Zhu, S. Jia, J. Zheng, Y. Lin, Y. Wu and J. Wang, *J. Mater. Chem. C*, 2018, **6**, 3097–3103.
- 502 K. Yan, Z. Wei, J. Li, H. Chen, Y. Yi, X. Zheng, X. Long, Z. Wang, J. Wang, J. Xu and S. Yang, *Small*, 2015, **11**, 2269–2274.
- 503 W. Wei, B. Hu, F. Jin, Z. Jing, Y. Li, A. A. García Blanco, D. J. Stacchiola and Y. H. Hu, *J. Mater. Chem. A*, 2017, **5**, 7749–7752.
- 504 C. Zhang, S. Wang, H. Zhang, Y. Feng, W. Tian, Y. Yan, J. Bian, Y. Wang, S. Jin, S. M. Zakeeruddin, M. Grätzel and Y. Shi, *Energy Environ. Sci.*, 2019, **12**, 3585–3594.
- 505 S. Mathew, A. Yella, P. Gao, R. Humphry-Baker, B. F. E. Curchod, N. Ashari-Astani, I. Tavernelli, U. Rothlisberger, M. K. Nazeeruddin and M. Grätzel, *Nat. Chem.*, 2014, **6**, 242–247.
- 506 K. Kakiage, Y. Aoyama, T. Yano, K. Oya, J. I. Fujisawa and M. Hanaya, *Chem. Commun.*, 2015, **51**, 15894–15897.